Author:
Stell, Angharad C

Title:
Using Gaussian process emulation to quantify the global methane budget

Using Gaussian process emulation to quantify the global methane budget

Angharad Caroline Stell

A dissertation submitted to the University of Bristol in accordance with the requirements for award of the degree of Doctor of Philosophy in the Faculty of Science

School of Chemistry

July 2020

Word count: 29 000

Abstract

The atmospheric concentration of methane (the second most important greenhouse gas) is increasing, despite plateauing between 2000 and 2007. These changes remain unexplained despite a multitude of studies, each suggesting different primary drivers.

This thesis works towards constraining the methane budget and thoroughly quantifying its uncertainty. Gaussian process emulators are developed, which estimate the relationship between uncertain inputs (methane sources and sinks) and observable outputs (monthly average hemispheric mole fraction and δ^{13}C-CH_4 time series) for a three-dimensional chemical transport model (MOZART), without assuming linearity. The emulators run as fast as two-dimensional box models, but have inter-annually varying transport and MOZART's spatial resolution. Some minor source and sink parameters were held constant, and their uncertainty was, for the first time, included by considering the range of observable outputs when these parameters are varied within their uncertainties. This invariant parameter uncertainty was found to be comparable to previously estimated model uncertainties and thus should be considered in future studies.

Using the emulators, two analyses that would have been unfeasible for the computational expense of MOZART were carried out. The first is a sensitivity analysis to find the methane sources and sinks whose uncertainties cause the largest amount of variance in the modelled observable outputs. This analysis showed several parameters (such as the freshwater source, the Cl loss, and the initial conditions) that have often had their uncertainty ignored previously, have large effects on the modelled observable outputs. In the second analysis, the emulator output was compared to atmospheric observations to reduce the uncertainty ranges of the sources and sinks. However, only 10 out of 28 parameters were constrained, and the uncertainty ranges remained large. These large parameter ranges could explain the disagreement between many previous studies, which came to different conclusions about recent methane changes, despite using the same atmospheric datasets.

Acknowledgements

This thesis would have been impossible without the help of Matt Rigby and Luke Western, and they deserve more thanks than this one sentence can give. All the Atmospheric Chemistry Research Group deserve a special mention for their support, in both moral and baked form.

I have read many emotional acknowledgements preceding theses, but that is not me. However, I wrote the majority of this thesis during the coronavirus pandemic, so I would also like to thank every person who supported me when all plans went awry, in particular Matt Boyd. This list of people does not only include those whose messages made me smile, but also the NHS staff, the supermarket workers, the bin collectors, the public transport workers... without them, nothing would ever be achieved.

Declaration

I declare that the work in this dissertation was carried out in accordance with the requirements of the University's Regulations and Code of Practice for Research Degree Programmes and that it has not been submitted for any other academic award. Except where indicated by specific reference in the text, the work is the candidate's own work. Work done in collaboration with, or with the assistance of, others, is indicated as such. Any views expressed in the dissertation are those of the author.

SIGNED:

DATE:

Contents

List of Tables

List of Figures

Chapter 1

Introduction

1.1 The importance of atmospheric methane

The concentration of methane (CH_4) in the atmosphere is rising (Dlugokencky 2020). This rise has implications for the climate because methane is the second most important anthropogenic greenhouse gas, in terms of radiative forcing (Myhre et al. 2013, Etminan et al. 2016), only surpassed by carbon dioxide (CO_2).

The amount of methane in the atmosphere is generally measured as a mole fraction: the number of methane molecules in a given number of air molecules, after the removal of water vapour. The unit of this measure is often communicated as nanomoles per mole, which is abbreviated in this thesis to parts per billion (ppb). There has been variation in the methane mole fraction for millennia, between inter-glacial (700 ppb) and glacial ages (400 ppb), as recorded by air trapped in Antarctic ice (Petit et al. 1999), though the cause of this variation remains unclear (e.g. Hopcroft et al. (2017)). However, since the industrial revolution, the mole fraction of methane, and many other greenhouse gases, has risen unusually quickly to an extraordinarily high value. The mole fraction of methane over the last 1 000 years can be seen in Figure 1.1.1, showing a sudden large increase after 1750. Today, the methane mole fraction has surpassed 1800 ppb (Dlugokencky 2020), compared to 700 ppb before the industrial revolution. The primary cause of the increased mole fraction of methane (and other greenhouse gases) is the industrialisation of human civilisation.

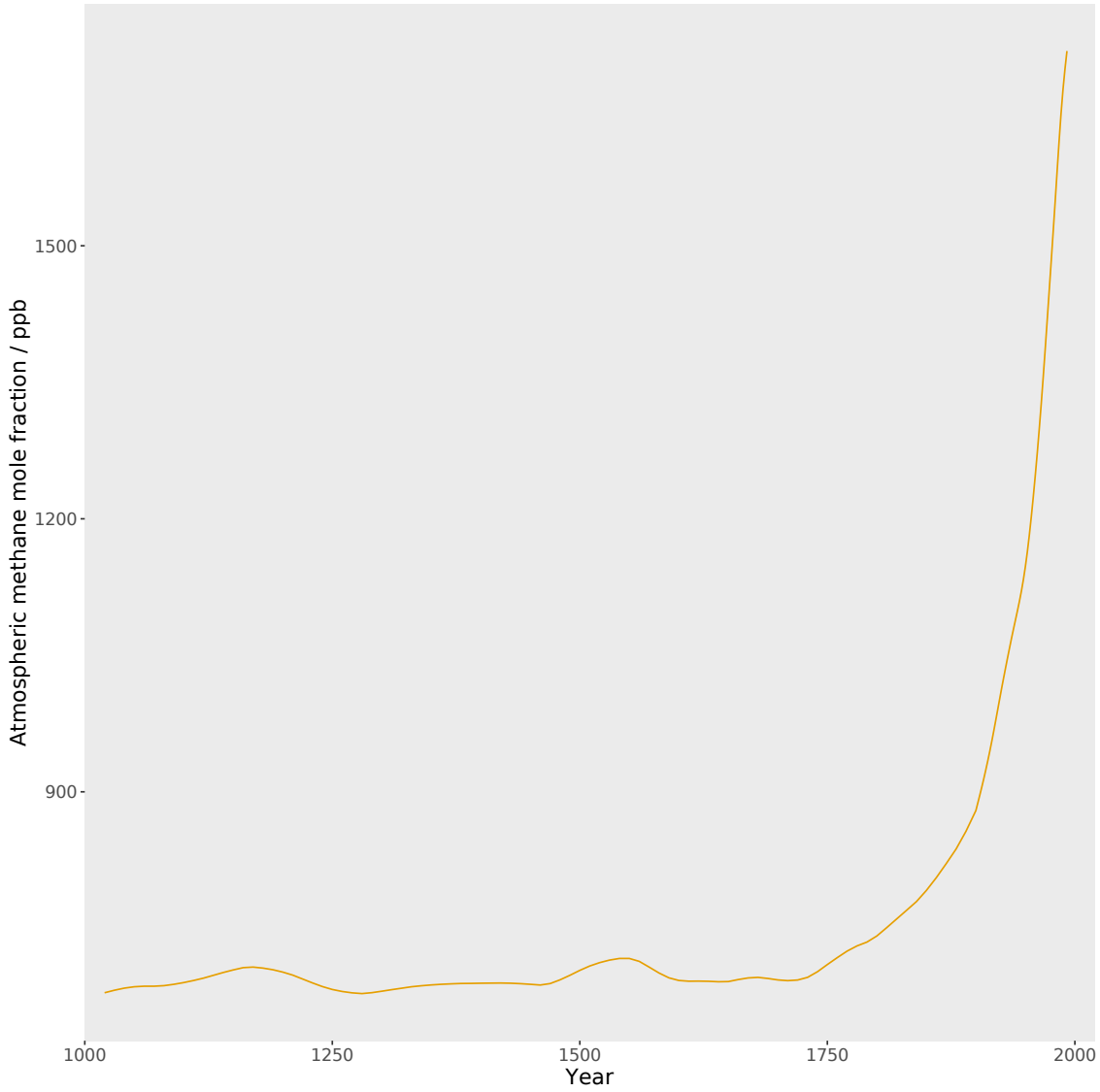

Figure 1.1.1: The global mean atmospheric methane mole fraction between the year 1020 and 1992 from the ice core data of Etheridge et al. (1998).

The effects of the increased greenhouse effect caused by rising concentrations of greenhouse gases are already being seen: the global mean temperature has increased by 1 °C above the average in 1961-1990 (Menne et al. 2018). However, this warming has not been evenly distributed, with polar areas warming by several degrees (Serreze & Barry 2011), which causes ice to melt, lowering the planet's albedo, and causing the temperature to rise further. The melting land ice also contributes to sea level rise, though this is mainly caused by the thermal expansion of the oceans (Mengel et al. 2016). The increased energy in the Earth system causes the climate to change, leading to more extreme weather events (Herring et al. 2020). For example,

the European heatwave of 2018 was significantly more likely due to anthropogenic warming (Leach et al. 2020), with a wide range of impacts from wildfires in Sweden to widespread drought.

All these changes have far-reaching implications not just for the planet, but for human society (IPCC 2014). Crop yields in many regions are predicted to decline severely (Lobell et al. 2008). Hundreds of millions of people live on low lying coastal land that is expected to go under the high tide line or be at risk of coastal flooding due to sea level rise by 2100 (Kulp & Strauss 2019). Extreme weather events come with a death toll and an economic cost that has been increasing due to rising population and climate change (Kron et al. 2019). These changes do not just affect humanity, but every species on Earth, many of which are predicted to become extinct due to climate change and other human effects (e.g. Román-Palacios & Wiens (2020)).

Only recently has political action been taken to curb anthropogenic greenhouse gas emissions. The 2015 Paris Agreement states that the global mean temperature rise this century should be kept well below 2 °C, and we should attempt to keep it below 1.5 °C. However, the 1.5 °C rise is expected to be reached as soon as 2030 (IPCC 2018). In order to meet this target, the methane mole fraction needs to come down quickly because of methane's short lifetime and potency as a greenhouse gas. Methane has an atmospheric lifetime of around 10 years (Voulgarakis et al. 2013), far shorter than CO_2's hundreds (or thousands) of years (Archer & Brovkin 2008), so emissions reductions will more quickly translate to a decrease in atmospheric mole fraction. Methane is also about 30 times more potent a greenhouse gas than CO_2 over 100 years using the Global Warming Potential metric (Myhre et al. 2013, Etminan et al. 2016). About 20 % of the warming since the industrial revolution is due to methane (Myhre et al. 2013), despite its much lower mole fraction than CO_2: around 1800 ppb CH_4 compared to 400 parts per million (ppm) CO_2 (Dlugokencky 2020, Dlugokencky & Tans 2020). Part of this warming is because methane's impact on climate does not end when it is removed from the atmosphere. The removal process can lead to the production of ozone, stratospheric water vapour, and CO_2.

All of these species are substantial contributors to the radiative forcing of the planet (Myhre et al. 2013).

Without intervention, methane may participate in positive feedbacks on climate change: methane emissions from sources such as melting hydrates and permafrost (Schuur et al. 2015), as well as wetlands and fresh water (Yvon-Durocher et al. 2014), are expected to increase as temperature rises. Additionally, the warming effect of methane is non-linear with respect to its emissions. The main loss of methane is reaction with the hydroxyl radical (OH) (Ehhalt & Heidt 1973), and one of the main losses of OH is reaction with methane (Gligorovski et al. 2015). Therefore, as more methane is emitted and reacts with OH, there is less OH to remove the remaining methane, and hence the methane lifetime increases (Myhre et al. 2013).

Therefore, suggested future scenarios that keep the global mean temperature below 2 °C by the end of the century have involved substantial reductions in the methane mole fraction. The Representative Concentration Pathways (RCPs) (van Vuuren et al. 2011) are greenhouse gas mole fraction trajectories suggested by the Intergovernmental Panel on Climate Change (IPCC) that produce different anthropogenic radiative forcings. Of these four pathways, RCP2.6 is the most drastic reduction in greenhouse gas mole fractions, and the only one that will make 2 °C warming unlikely (Collins et al. 2013). This pathway involves an approximately 30 % decrease in the methane mole fraction from 2005 levels by the end of this century (Meinshausen et al. 2011). However, since 2005, methane concentrations have continued to rise with potentially grave consequences for the Paris Agreement (Nisbet et al. 2019). As a result, new suggested scenarios involve an even stronger 45 % decrease in the methane mole fraction from 2015 levels by the end of the century (Meinshausen et al. 2020). But once again, the methane mole fraction has continued to rise since 2015, which is particularly concerning as scientists cannot agree why (Section 1.7). Without improvements to methane source attribution, it will become more difficult to formulate effective mitigation measures (Ganesan et al. 2019, Nisbet et al. 2019).

The reduction of the methane mole fraction must become a priority. Therefore,

understanding its sources and sinks, which are outlined in the following section, is of the upmost importance.

1.2 The sources and sinks of atmospheric methane

The atmospheric methane budget is composed of various sources and sinks, the mean magnitudes of which are shown in Figure 1.2.1, along with their ranges in the literature as error bars (Saunois et al. 2016). The lack of understanding of the sources and sinks of methane is demonstrated by the large error bars in this figure, and also by the mismatch between bottom-up (inventory and process model-based) and top-down (atmospheric data-based) emissions estimates (Section 1.3), seen in Table 1.1. Whilst the two ways of estimating emissions agree quite well for anthropogenic sources (331 $\mathrm{Tg\,yr^{-1}}$ for bottom-up and 335 $\mathrm{Tg\,yr^{-1}}$ for top-down), there is a large difference between the emissions derived using the two methods for the natural sources: 347 $\mathrm{Tg\,yr^{-1}}$ for bottom-up and 218 $\mathrm{Tg\,yr^{-1}}$ for top-down. This is a discrepancy in the total global source of methane of 125 $\mathrm{Tg\,yr^{-1}}$, which is 18 % of bottom-up emissions and 23 % of top-down emissions. It is important to know what fraction of the total global emissions are anthropogenic, so that the required reduction in anthropogenic emissions can be calculated. In this section, an overview of the methane budget is presented, highlighting the main sources of uncertainty.

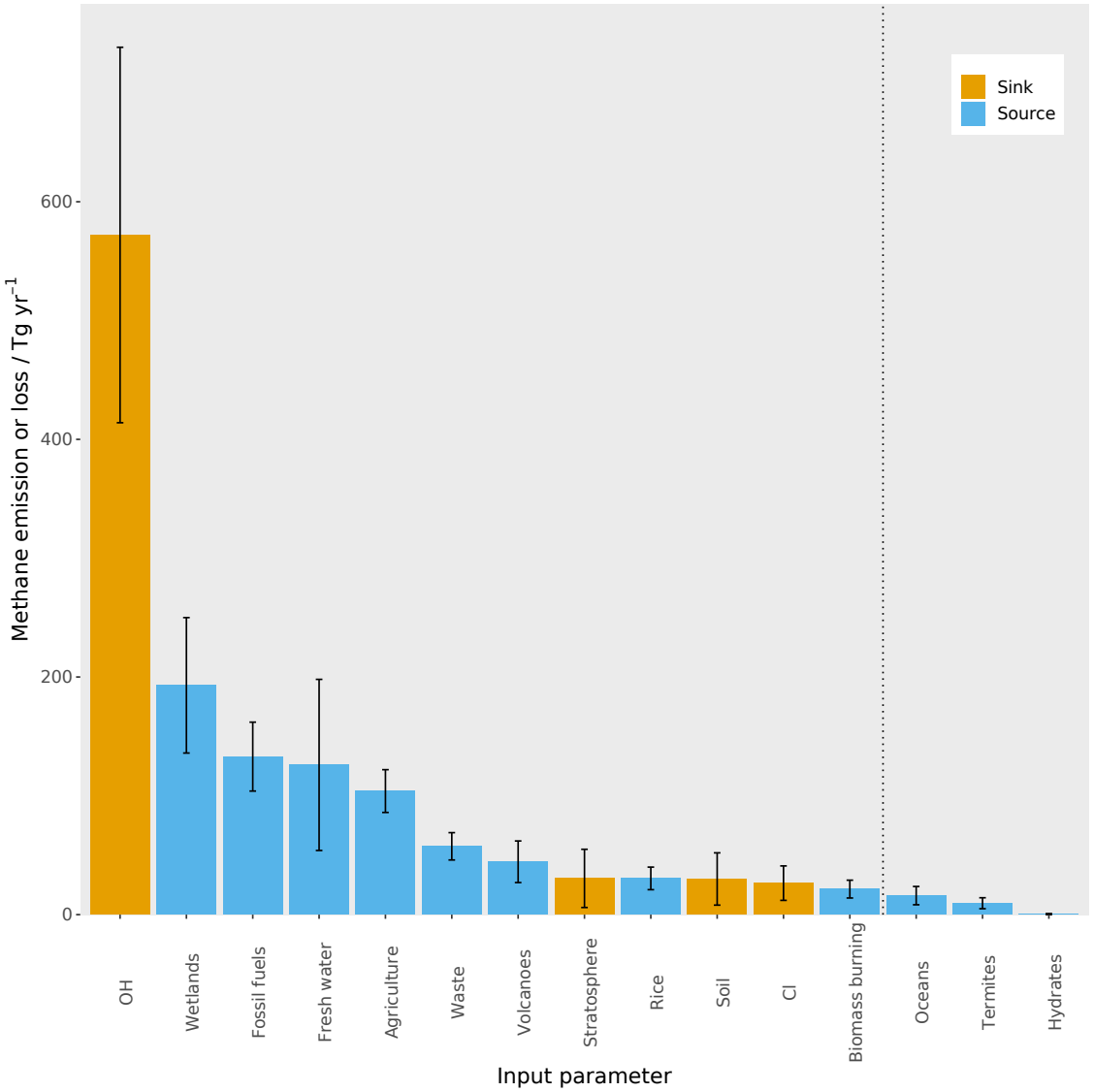

Figure 1.2.1: The magnitude of the different sources and sinks in the methane budget, according to the combined ranges of the bottom-up (inventory or process model-based) and top-down (atmospheric data-based) estimates (Saunois et al. 2016). The blue bars are sources of methane and the orange bars are sinks of methane. The error bars represent the range of possible values used in this work, which are the minimum and maximum possible values given in Saunois et al. (2016). The dashed black line shows the cut off between the parameters that are examined in this work, and those that are not (see Section 2.3.1 for more detail).

	Methane emission or loss / $\mathrm{Tg\,yr^{-1}}$	
	Bottom-up	Top-down
Natural sources	347 (238-484)	218 (179-273)
Anthropogenic sources	331 (304-368)	335 (273-409)
Chemical losses	604 (483-738)	518 (510-538)
Soil loss	28 (9-47)	36 (26-42)

Table 1.1: The magnitude of bottom-up and top-down methane source and sink estimates, as reported in Kirschke et al. (2013) for the period 2000 to 2009. The numbers in parenthesis are the minimum and maximum values.

1.2.1 Sources

About half of methane emissions originate from natural sources (Table 1.1), which include wetlands, fresh water, volcanoes, wildfires, oceans, and termites. The other half is from anthropogenic sources, which are dominated by fossil fuels, agriculture (primarily ruminants and rice), and waste. These disparate sources can be divided into three emission pathways: biogenic, thermogenic, and pyrogenic. Biogenic methane is produced by bacteria in anaerobic environments, such as waterlogged soils or animal intestines. Thermogenic methane is produced by the breakdown of organic matter by heat and pressure deep underground. Thermogenic methane escapes to the atmosphere either naturally or by the extraction, distribution, or utilisation of fossil fuels. Pyrogenic methane is produced by the incomplete combustion of biomass, such as the burning of forests or biofuels. Three minor methane sources (oceans, termites, and hydrates) are not explored in detail in this work, but each of the major sources examined in this thesis are described in this section.

Wetlands

Wetlands are generally thought to be the largest single source of methane to the atmosphere, as seen in Figure 1.2.1. These are ecosystems with inundated or saturated soils, which includes bogs, fens, swamps, marshes, and floodplains. The waterlogged soils create anaerobic conditions, so that when bacteria (methanogens) break down

organic matter, they release methane rather than CO_2. Factors such as the height of the water table (which affects oxygen availability), temperature, soil pH, and the amount of organic matter are all important for the amount of methane produced (Valentine et al. 1994, Wania et al. 2010). The methane released makes its way to the atmosphere by three pathways: molecular diffusion, plant-mediated transport, and ebullition. Before reaching the atmosphere, the methane can be oxidised by a different type of bacteria, known as methanotrophs (Chowdhury & Dick 2013). Wetlands have one of the largest uncertainties among the methane sources (Saunois et al. 2016). This is because it is challenging to define the wetland area that produces methane, the timing of wetland emissions, and parameterise the behaviour of both the bacteria types that generate and oxidise the methane (Melton et al. 2013, Wania et al. 2013, Bloom et al. 2017).

Climate change is expected to increase wetland methane emissions due to the temperature dependence of the bacterial metabolism (Yvon-Durocher et al. 2014). Additionally, climate change will change precipitation patterns, which may also increase wetland emissions (Shindell et al. 2004). However, there will be regional dependencies and some boreal wetlands could become cooler and drier, which would decrease emissions (Watts et al. 2014). There are suggestions that wetlands have previously contributed to warming events. For example, 15 000 years ago a rapid warming took place (Thompson et al. 1998, Chappellaz et al. 1993) alongside an increase in atmospheric methane (Brook et al. 1996, Chappellaz et al. 1993). This methane is proposed to have come from tropical wetlands as ice sheets covered the other main extratropical methane source areas (Chappellaz et al. 1990).

Fossil fuels

Fossil fuel methane is predominantly produced from the extraction, distribution, and utilisation of coal, oil, and natural gas. Natural gas is composed mainly of methane, so any leak in extraction or transportation, or incomplete combustion when used, will release methane to the atmosphere (Shorter et al. 1996, Lamb et al. 2015). For oil and coal, methane is created by the same processes that form the oil and coal,

and this methane is released to the atmosphere as the fuel is extracted (Karacan et al. 2011, Lyon et al. 2016). These emissions per unit of fossil fuel have been reduced in developed countries by capturing the methane for use as fuel, but this does not occur universally or as efficiently as possible (Karacan et al. 2011, Lyon et al. 2016).

The uncertainty in fossil fuel emissions is partly due a lack of site-specific data, as the amount of methane emitted depends on many factors, such as the geological features of the extraction site and extraction technique used (Karacan et al. 2011). There are further regional variations in distribution emissions (e.g. leaking pipes) as this is highly dependent on the age and how well maintained the transport infrastructure is (Plant et al. 2019).

Fresh water

Freshwater bodies emit methane by bacteria breaking down organic matter in an anaerobic environment. These emissions have been more widely recognised as important as the number of studies has increased, with Saunois et al. (2016) estimating methane emissions of 122 $\mathrm{Tg\,yr^{-1}}$. Whilst there are now a relatively large number of observational studies in a wide range of locations (from South America (Bastviken et al. 2010), Africa (Borges et al. 2015), up to the Arctic circle (Wik, Varner, Anthony, MacIntyre & Bastviken 2016)) there is still a large amount of uncertainty in the emissions from freshwater bodies. This uncertainty is due to the wide range of observed values for different freshwater systems. Freshwater emissions estimates vary not only between lakes, reservoirs, and rivers; but also between different climates (for example tundra or boreal (Wik, Varner, Anthony, MacIntyre & Bastviken 2016)).

There is even large variation within individual water bodies (Bastviken et al. 2004), due to the many different emission pathways. The four main pathways are diffusive flux across the water surface, ebullition from the sediment, plant-mediated transport, and degassing and elevated methane concentrations downstream from reservoir turbines (Bastviken et al. 2004, Guérin et al. 2006, Yang 2019). Ebullition is often

the main source, and its episodic nature means that it is difficult to capture these emissions in limited observations (Bastviken et al. 2004). Each of these pathways has many dependent variables that control it, making a global estimate of emissions challenging. This long list of factors includes water body area, body depth, sediment type, temperature, pressure, wind, amount of sediment running into the water, amount of plants present, and if the body is ice-covered (Wik, Varner, Anthony, MacIntyre & Bastviken 2016, Natchimuthu et al. 2016, Davidson et al. 2018).

Climate change is expected to increase freshwater methane emissions. The temperature dependence of the bacterial emissions means that as the climate warms, methane emissions are expected to grow (Yvon-Durocher et al. 2014, 2017). Rising temperatures will also increase the number of ice-free days on Arctic lakes: Wik, Varner, Anthony, MacIntyre & Bastviken (2016) predict that 20 more ice-free days each year (which is expected before 2079 for most of the Arctic) could raise lake and pond emissions by 30 %. Perhaps this will be offset by these bodies reducing in total area due to large-scale drainage from thawing permafrost (Avis et al. 2011, van Huissteden et al. 2011, Bouchard et al. 2014). However, it is not only temperature that is expected to change: increases in precipitation will likely increase organic loading to fresh water, which would increase methane emissions wherever precipitation increases (Davidson et al. 2018). Increased cloud cover might also reduce shortwave energy input, reducing methane emissions (Wik et al. 2014, Wik, Varner, Anthony, MacIntyre & Bastviken 2016). Overall, there is evidence to suggest that freshwater emissions will increase, but it is uncertain.

Agriculture

Agricultural emissions of methane are mostly from ruminants and rice paddies. The digestive systems of ruminants provide a good environment for the bacteria that produce methane, which is subsequently released through the mouth or rectum of the ruminant. There are 1.5 billion cattle, 1.2 billion sheep, and around one billion goats on the planet, and their numbers are increasing (FAO 2020). Most of the

livestock emissions come from cattle, not only because of their number, but also their large size, and particular digestive system (Crutzen et al. 1986). Additional emissions are possible if the manure produced by livestock is stored under anaerobic conditions (Arndt et al. 2018, Kupper et al. 2020).

In this thesis, rice has been separated out from the rest of the agricultural source as it has a distinct spatial distribution. Rice grows in waterlogged soils which result in anaerobic conditions and hence when organic matter decomposes, methane is released. Some of this methane is oxidised in the soil, some is leached away in the floodwater, but the rest escapes to the atmosphere either through the rice plant, or diffusion and bubbling in the water; the same processes as the wetlands and freshwater sources (Bridgham et al. 2013).

The uncertainty in the agricultural emissions comes from incomplete reporting and local variation in the emissions per animal or per amount of rice. Livestock emissions depend on the weight of the animal and the animal's diet, and manure emissions depend on the manure composition, management system, length of storage, and meteorological variables like temperature and wind (Hristov et al. 2018). Rice emissions are affected by different fertilization practices, soil temperatures, soil types, rice variety, and cultivation practices (Conrad et al. 2000, Yan et al. 2009).

Rice emissions are expected to increase as the planet warms, with high atmospheric CO_2 and warmer temperatures potentially causing methane emissions per kilogram of rice to double by the end of the century (van Groenigen et al. 2013). To reduce these emissions, cultivation practices can be adapted, for example brief aeration of the soil (Yuan et al. 2011) and continuous cycles of dry and wet soil (Ma et al. 2012) have been shown to reduce methane emissions. Livestock emissions could potentially be reduced by selective breeding, changes in diet, and changes in manure management systems to avoid anaerobic conditions (Wallace et al. 2019, Kinley et al. 2020, Kupper et al. 2020).

Waste

Landfills and waste water handling emit methane through decomposition by bacteria in an anaerobic environment. The amount of methane emitted depends on biological controls, such as temperature, moisture, and pH (de Mes et al. 2003, Emkes et al. 2015). In landfills, the separation of biodegradable material and recycling from general waste reduces emissions, alongside gas capture (Boerboom et al. 2010). Many landfills are covered by soil which oxidises some of the methane emitted, and can turn the landfill into a methane sink (Bogner et al. 1995). In waste water treatment, aeration and gas capture are promising mitigation strategies (Daelman et al. 2012). However, these mitigation strategies are costly, and so difficult for less developed countries.

Volcanoes

Methane is released naturally from the Earth's crust (Etiope & Klusman 2002). Methane can be formed by either biogenic or thermogenic breakdown of organic matter in hydrocarbon basins, or without organic matter, for example magma degassing, in geothermal areas (Etiope & Klusman 2002).

Biomass burning

Incomplete combustion of biomass emits methane, this can be from biomass burning (wildfires or agricultural clearing) or biofuel. In this thesis, biofuel was counted with fossil fuels as it is anthropogenic, for example domestic cooking and heating (Ozgen & Caserini 2018). Pre-industrial fire activity was potentially even greater than the present day, though why is uncertain (van der Werf et al. 2013). However, humans have increased fire activity in places of deforestation (e.g. Fearnside (2005)) and remote regions (Mollicone et al. 2006). Climate change may also lead to more frequent and intense fires caused by droughts in key regions (Kasischke et al. 1995, Westerling et al. 2006). Emissions depend on the amount burned, burning conditions, and material burning (van der Werf et al. 2010), so types of stove and fire burning practices could reduce biofuel emissions (Ozgen & Caserini 2018).

1.2.2 Sinks

There are four main ways that methane is removed from the atmosphere: reaction with the hydroxyl radical (OH) (e.g. Ehhalt (1974)), reaction with the chlorine radical (Cl) in the marine boundary layer (e.g. Allan et al. (2007), Thornton et al. (2010)) and the stratosphere (e.g. McCarthy et al. (2003), Röckmann et al. (2004), Thanwerdas et al. (2019)), reaction with oxygen atoms in an excited singlet state ($O(^1D)$) in the stratosphere (e.g. McCarthy et al. (2003), Röckmann et al. (2004)), and methanotrophic loss in soils (Curry 2007, Dutaur & Verchot 2007). As seen in Figure 1.2.1, by far the largest of these (with the largest uncertainty too) is the reaction with OH, hence this sink is further explored in this section.

The hydroxyl radical

The hydroxyl radical is formed in the atmosphere by several different processes. The dominant process is a two step reaction (McGrath & Norrish 1960), which starts with the photolysis of ozone (O_3):

$$O_3 + h\nu \longrightarrow O_2(^1\Delta_g, {}^3\Sigma_g) + O(^1D). \tag{1.1}$$

The $O(^1D)$ then reacts with water vapour to produce two OH radicals:

$$O(^1D) + H_2O \longrightarrow 2\,OH. \tag{1.2}$$

This process has been shown to be a minor contributor to OH formation in some of the lowermost parts of the atmosphere, particularly under polluted conditions. In these areas, the photolysis of HONO, the ozonolysis of alkenes, and the photolysis of HCHO have all been shown to be significant sources of OH (e.g. Vogel et al. (2003), Ren et al. (2006), Elshorbany et al. (2009)).

The hydroxyl radical is very reactive so typically exists for less than a second before reacting (Levy 1971), predominantly with carbon monoxide:

$$OH + CO \longrightarrow H + CO_2, \tag{1.3}$$

immediately followed by

$$H + O_2 + M \longrightarrow HO_2 + M. \tag{1.4}$$

The hydroxyl radical is also lost in significant amounts by reaction with methane:

$$OH + CH_4 \longrightarrow CH_3 + H_2O, \tag{1.5}$$

immediately followed by

$$CH_3 + O_2 + M \longrightarrow CH_3O_2 + M. \tag{1.6}$$

As outlined in Section 1.1, methane is mainly removed by reaction with OH and OH is removed by reaction with methane, which is the source of a positive feedback in the methane budget. As the methane mole fraction increases, less methane can be removed and the methane lifetime increases. This feedback is also an important consideration in methane modelling studies because it causes a non-linear response in the methane mole fraction from a change in methane emissions, which will be further discussed in Section 2.2.2.

Due to the hydroxyl radical's short lifetime, it is found where it is produced: predominantly in the tropics, where sunlight and water vapour are abundant. Mid-latitudes have a large seasonal cycle as more hydroxyl radical is formed in the summer hemisphere due to the seasonal variation in sunlight and water vapour concentrations (Spivakovsky et al. 2000). Despite this large seasonal fluctuation in the distribution, on an annual scale, the inter-hemispheric difference in the hydroxyl radical concentration is thought to be small, for example Patra et al. (2014) suggest a hemispheric ratio of 0.97 ± 0.12.

As the Earth's temperature increases, the concentration of water vapour is expected to rise, causing the concentration of the hydroxyl radical to increase. For example, Wu et al. (2008) suggest an increase of 12 % in the global tropospheric hydroxyl radical concentration from 2000 to 2050. However, this change will be dependent on

anthropogenic emissions of gases such as methane and other hydrocarbons, as well as and nitrogen oxides (NO_x). Different RCPs produce a large range of changes in the hydroxyl radical concentration, e.g. +9 % for RCP4.5 or -15 % for RCP8.5 over the 21st century (John et al. 2012).

Substantial historic changes to the hydroxyl radical concentration have been suggested by ice core proxy data using the ratio of HCHO to CH_4: more than +50 % from the last glacial maximum to the preindustrial Holocene (Staffelbach et al. 1991) and -20 % from the preindustrial Holocene to the present day (Gillett et al. 2000, Alexander & Mickley 2015). However, atmospheric models predict smaller changes for these periods, raising concerns that these models underestimate the hydroxyl radical's sensitivity to future climate change (Alexander & Mickley 2015).

There is a large amount of uncertainty in the recent temporal trend of the global OH concentration. Inverse modelling studies using methane, methyl chloroform (Section 1.3.2), and OH infer negative trends in OH since the renewed methane growth in 2007 (Rigby et al. 2017, Turner et al. 2017) but with a large uncertainty. However, modelling studies that focus on inferring OH concentration, and so include important factors such as O_3, H_2O, NO_x, and temperature, have inferred both a positive trend (Stevenson et al. 2020) and very little trend (Nicely et al. 2018).

1.3 Methods of source and sink estimation

1.3.1 Methods of source estimation

Bottom-up estimation

Emissions can be estimated in a bottom-up method by measuring methane fluxes (usually at small scales) coming from a particular activity and then scaling by the total amount of that activity. This flux measurement can be done directly for a point source from the composition and flow rate of the gas being released (such as at valves in fossil fuel extraction (Allen et al. 2013)), or using a chamber for a small but more disperse source (such as a small area of wetland (Gutenberg et al. 2019)).

These local flux measurements can then be combined and generalised in process models and emission inventories to give estimates of global emissions.

There are many types of process models, for example, some reproduce the biochemical processes leading to emissions, such as those that occur in wetlands (e.g. Bloom et al. (2017)), which depend on things such as temperature and water availability. This method does require a mechanistic understanding of the processes involved, which can be very complex.

Emission inventories are a bottom-up estimate for a particular source type over a region or country using a synthesis of various estimation methods. Emissions for a sector can be calculated over a region or country by the product of an activity level, an emission factor for the activity, and potentially an abatement coefficient that accounts for regulations to reduce anthropogenic emissions (IPCC 2006, AMAP 2015). For example, an emission inventory of fossil fuel extraction might have a map of the amount of fuel extracted as the activity data and the mass of methane emitted per unit of fuel extracted as an emission factor. These emission factors will be derived from the flux measurements and process models.

Top-down estimation

The magnitudes of sources can be determined through top-down methods which use atmospheric observations. For example, eddy covariance measurements can be used to calculate the emissions from a specific source, in this method concentration measurements combined with local meteorological data can be used to infer the surface flux (e.g. Tang et al. (2018)). Alternatively, the need for meteorological data can be bypassed by releasing a tracer not emitted by the source, at a known rate, and measuring the ratio of the tracer and methane downwind. By assuming both the tracer and methane undergo the same atmospheric dispersion, with the rate of dilution depends on the relative size of the emission and the background concentration, the methane emission flux can be calculated (e.g. Yacovitch et al. (2017)). To quantify regional or global emissions, a variety of atmospheric observations can be used,

which are discussed in detail in Section 1.4, with the atmospheric models and inversion techniques in Sections 1.5 and 1.6, respectively. This inverse technique involves working backwards from the atmospheric observations, using the model transport and loss processes, to infer where methane was emitted. This method will be the focus of this thesis, so many previous studies that use this method are discussed in detail in Section 1.7.

1.3.2 Methods of sink estimation

Like the sources, the soil loss can be estimated by measurements (e.g. Czepiel et al. (1995)) and process modelling (e.g. Murguia-Flores et al. (2018)). However, a different approach is taken for the other sinks of methane. The global concentration of a reactive chemical species, such as OH, is hard to determine due to its very short lifetime, meaning that any measurement is only representative of a very small region for a very short time. As a result, there are only measurements of OH at very small scales (e.g. Poppe et al. (1994), Mount & Williams (1997), Heard & Pilling (2003), Heard (2006), Martinez et al. (2010)), and global concentrations must be determined indirectly. This can be done through photochemical models of its formation and destruction in the atmosphere (e.g. Spivakovsky et al. (2000), Nicely et al. (2018), Stevenson et al. (2020)). This method has also often been used for the other reactive loss species, the Cl radical and $O(^1D)$ (e.g. Sherwen et al. (2016), Röckmann et al. (2004)). Additionally, inversion techniques (as in Section 1.3.1) can be used, with examples in Section 1.7.

Alternatively, the OH concentration can be indirectly determined using measurements of one of the gases that OH oxidises. Any gas predominantly removed from the atmosphere by OH, that has relatively well known emissions can be used. For example, ^{14}CO is created at a relatively well known rate by cosmic rays interacting with nitrogen atoms to produce ^{14}C:

$$n + {}^{14}_{7}N \longrightarrow {}^{14}_{6}C + p, \tag{1.7}$$

which is oxidised to ^{14}CO (Pandow et al. 1960):

$$^{14}C + O_2 \longrightarrow {}^{14}CO + O. \tag{1.8}$$

^{14}CO is mainly removed by OH oxidation, so can be used to estimate global OH concentrations (Weinstock 1969). For example, Quay et al. (2000) combined ^{14}CO surface measurements and a two-dimensional atmospheric model to estimate a tropospheric OH concentration of 10×10^5 molecules cm^{-3}. However, the concentration of ^{14}CO, and hence inferred OH, is sensitive to the model transport parameter values.

One of the most popular gases for inferring the OH concentration is methyl chloroform (1,1,1 trichloroethane or CH_3CCl_3) (Lovelock 1977). This gas is less sensitive than ^{14}CO to the model transport parameter values because of its longer lifetime (about 5 years compared to 2 months), so should provide more certain OH estimates (Quay et al. 2000). Methyl chloroform was emitted primarily by industrial sources (where it was used as a cleaning agent and solvent), which should be known relatively accurately (e.g. Midgley & McCulloch (1995)), and its primary loss is by reaction with OH (although there is a small amount of transfer between the ocean and atmosphere (Wennberg 2004) and stratospheric photochemical loss (Prinn et al. 2001)). This means that measurements of this gas should allow the determination of OH concentration through use of an atmospheric model. For example, Prinn et al. (2001) used this method to calculate the global OH concentration as 9.4×10^5 molecules cm^{-3} for 1978-2000, although this varied significantly from year to year. This study also concluded that the OH concentration is lower in the northern hemisphere than the southern hemisphere, but this is highly uncertain. These conclusions have been questioned, as this process assumes that the methyl chloroform emissions, the rate of the other loss processes, the reaction rate with OH, and the atmospheric transport in the model are all reliable, which is debated (e.g. Krol & Lelieveld (2003)). The Montreal Protocol banned production of ozone-depleting substances such as methyl chloroform, and so emissions of this gas should have been near zero since 2010, though how near is uncertain (McCulloch & Midgley 2001, Rigby et al. 2019). As

the measured concentrations decrease, this method will become increasingly difficult as the concentrations approach the measurement detection limit.

1.4 Atmospheric observations of methane

Since there are so many highly uncertain sources and sinks of methane, monitoring the atmospheric methane mole fraction is important. When combined with atmospheric models, this monitoring data can tell us about changes in the methane sources and sinks using top-down estimation methods.

To measure the atmospheric methane mole fraction from the past $\sim 10^6$ years, air trapped in ice can be analysed (Yan et al. 2019). However, there are many effects that need to be accounted for in these measurements (Bender et al. 1997). Most importantly, these samples are limited in their locations, and the air samples are not a snapshot of a given time, but a mixture of multiple years, as the air in the ice mixes with the atmosphere until it is buried deep under the ice. This results in a very low spatial and temporal resolution for ice core data.

To examine the methane mole fraction in the most recent $\sim 10^2$ years, ground-based atmospheric measurement stations have been used, where continuous monitoring or discrete air samples can be taken. It is these flask samples that are used in this thesis, and are discussed in Section 1.4.1. More recently, satellites have become a common way to measure the methane mole fraction, which is further discussed in Section 1.4.2.

1.4.1 Methane mole fractions from ground-based stations

Since 1983, the Global Monitoring Laboratory (GML) Carbon Cycle group (part of National Oceanic and Atmospheric Administration (NOAA) (Dlugokencky et al. 1994)), alongside other organisations (e.g. the Advanced Global Atmospheric Gases Experiment (AGAGE) (Prinn et al. 2018)), has been monitoring global atmospheric methane mole fractions by taking air samples at more than 50 locations around the

globe. The GML sampling locations, shown in Figure 1.4.1, are sparse, with important areas for methane production, such as the tropics and Asia, underrepresented in the measurements.

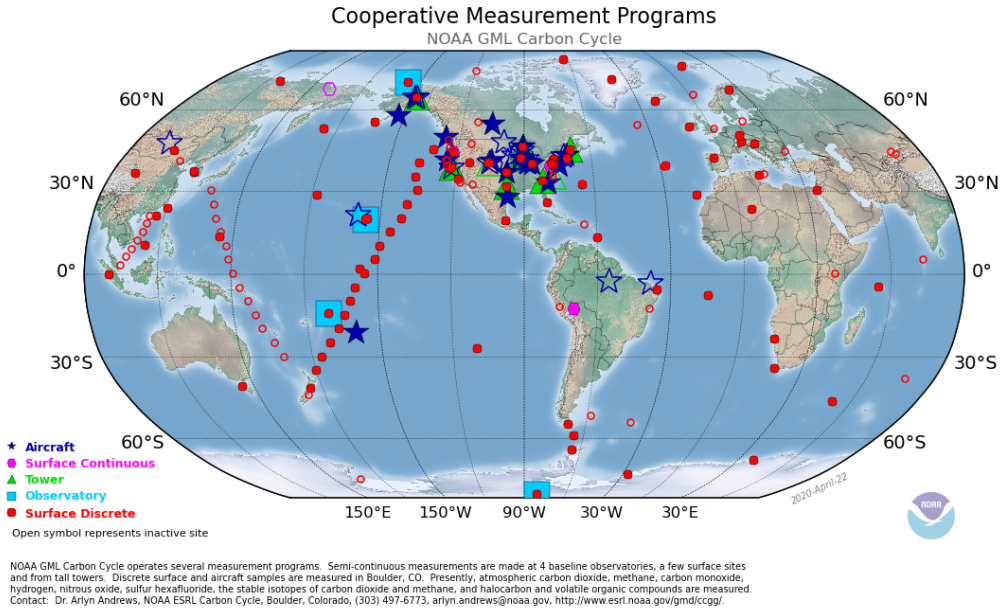

Figure 1.4.1: The locations where the NOAA GML Carbon Cycle group has taken GHG measurements, plotted by NOAA (2020).

It is the "surface discrete" stations in Figure 1.4.1 that will be used in this thesis. The stations aim to sample background air, where methane is well-mixed and local sources do not significantly contribute to the measured methane mole fraction, as these samples are thought to be representative of the hemisphere as a whole. Therefore, the stations are located far from local methane sources and any samples with evidence of above-baseline enhancements are removed from the dataset. At these stations, air samples are collected in flasks and shipped to the NOAA laboratory in Boulder to be analysed, where the mole fraction of several key trace gases is determined. The methane is isolated using a gas chromatograph, which separates gases based on their flow rates through a column with a coating that the gases have different affinities to. The methane fraction is then passed to a flame ionisation detector that ionises the methane, and the removed electrons create a current that can be monitored to measure the amount of methane. This measurement must be

compared to a standard with a known methane mole fraction measured in the same instrument to give an absolute methane mole fraction measurement (Dlugokencky et al. 1994).

The uncertainty in these measurements is calculated by the combination of an analytical repeatability error and NOAA's ability to propagate the methane mole fraction standard scale. The analytical repeatability is calculated as the average absolute value of the agreement of pairs of samples taken almost simultaneously, which varies between 0.8 and 2.3 ppb depending on the analytical instrument. The scale propagation error is calculated as 0.7 ppb by comparing flask and continuous measurements at two stations: Mauna Loa in the US and Barrow in the US. These two errors are added in quadrature to give a total measurement error (Dlugokencky et al. 2017).

The sine-latitude weighted global mean methane mole fraction calculated from combining all the surface station data is shown in Figure 1.4.2. These measurements show that the methane mole fraction has risen since 1983, but the rate of growth has changed. It slowed in the 1990s, before coming close to zero during 1999-2006. In 2007, the strong growth rate returned, and continues to this day (Dlugokencky 2003, Rigby et al. 2008, Dlugokencky et al. 2009). The causes of these changes are highly debated, as outlined in Section 1.7.

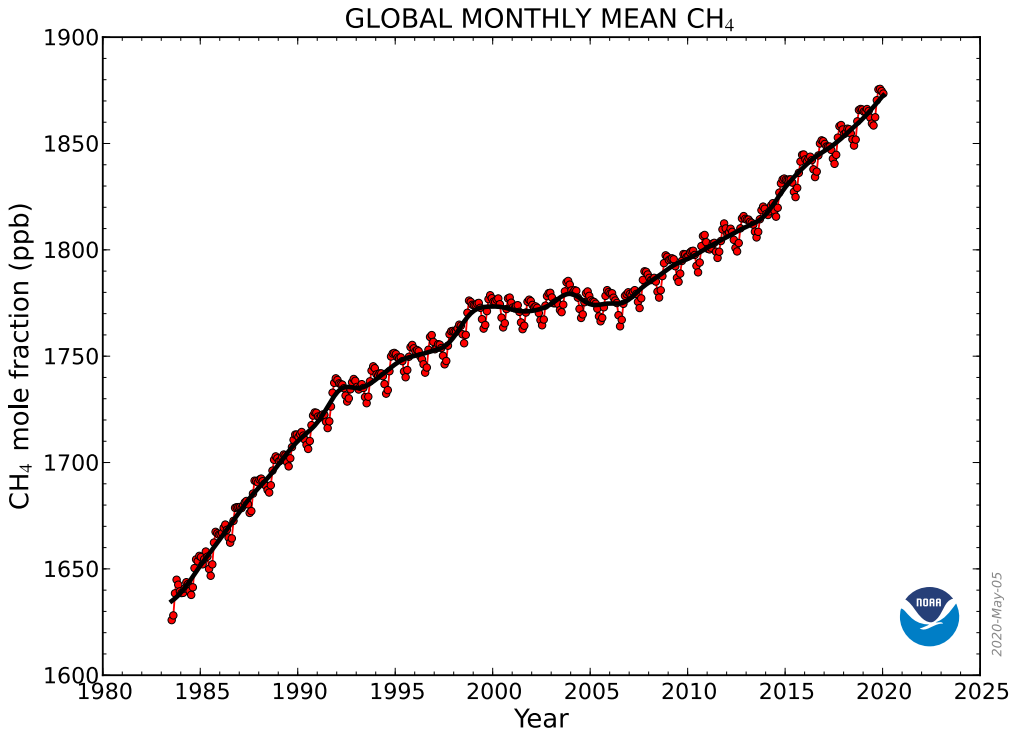

Figure 1.4.2: The measured sine-latitude weighted global mean atmospheric methane mole fraction from NOAA's surface measuring stations, plotted by Dlugokencky (2020). The red line and circles are monthly means, and the black line shows the 12 month running mean with the average seasonal cycle removed.

1.4.2 Methane mole fractions from satellites

The advent of satellite data in the last few decades has made near global coverage of methane measurements possible (e.g. Hu et al. (2018)). However, this does mean that a huge amount of data is produced which can be difficult to utilise fully, although data collection is limited in certain locations for certain times as cloud or the amount of reflected solar radiation (e.g. at low solar zenith angles) prevents measurement. Satellites provide less precise measurements than in situ instruments, as measurements are generally for columns of methane (from the surface to the top of the atmosphere), and models of the atmosphere are required to retrieve the data (e.g. Jacob et al. (2016)). Satellite data is expected to be complementary to, but not replace, the high precision but sparse ground-based stations.

1.4.3 Methane isotopologues

Measurements of methane's two most abundant isotopologues, $^{12}CH_4$ and $^{13}CH_4$, have been used along with methane mole fraction measurements to provide additional constraints on the methane budget (e.g. Bergamaschi et al. (1998), Quay et al. (1999), Schaefer et al. (2016), Nisbet et al. (2016), Rigby et al. (2017), Turner et al. (2017), McNorton et al. (2018), Nisbet et al. (2019)). The different sources of methane release different ratios of the two isotopologues, so if the ratio of the isotopologues is measured in the atmosphere, then it should provide some information on the magnitudes of the different sources. The ratio of the two isotopologues is measured as δ^{13}C-CH_4, which is defined as

$$\delta^{13}\text{C-CH}_4 = \left(\frac{\left(\frac{^{13}CH_4}{^{12}CH_4}\right)_{sample}}{\left(\frac{^{13}CH_4}{^{12}CH_4}\right)_{standard}} - 1 \right) \times 1000, \tag{1.9}$$

where the standard is the ratio of ^{13}C to ^{12}C in Pee Dee Belemnite (Coplen 2011) (which has the highest known value of δ^{13}C-CH_4), and the units of the measurement are parts per thousand or permil (‰). This means that the highest known fraction of $^{13}CH_4$ corresponds to a value of 0 ‰, and the more negative the δ^{13}C-CH_4, the less $^{13}CH_4$ is present.

The two isotopologues are emitted in different ratios from different sources (e.g. Whiticar & Schaefer (2007), Schwietzke et al. (2016)), depending on the process that generates the methane: microbial sources release methane with a typical δ^{13}C-CH_4 of around -62 ‰, thermogenic approximately -44 ‰, and pyrogenic about -22 ‰ (Schwietzke et al. 2016). However, these values are highly dependent on the same factors that affect methane production (such as the plant types in a wetland) meaning that there is a large amount of uncertainty and local variation in these values (e.g. Ganesan et al. (2018)). This means that the uncertainty ranges of many methane source δ^{13}C-CH_4 values overlap, as seen in Figure 1.4.3, which shows the uncertainty ranges used for the sources in this work.

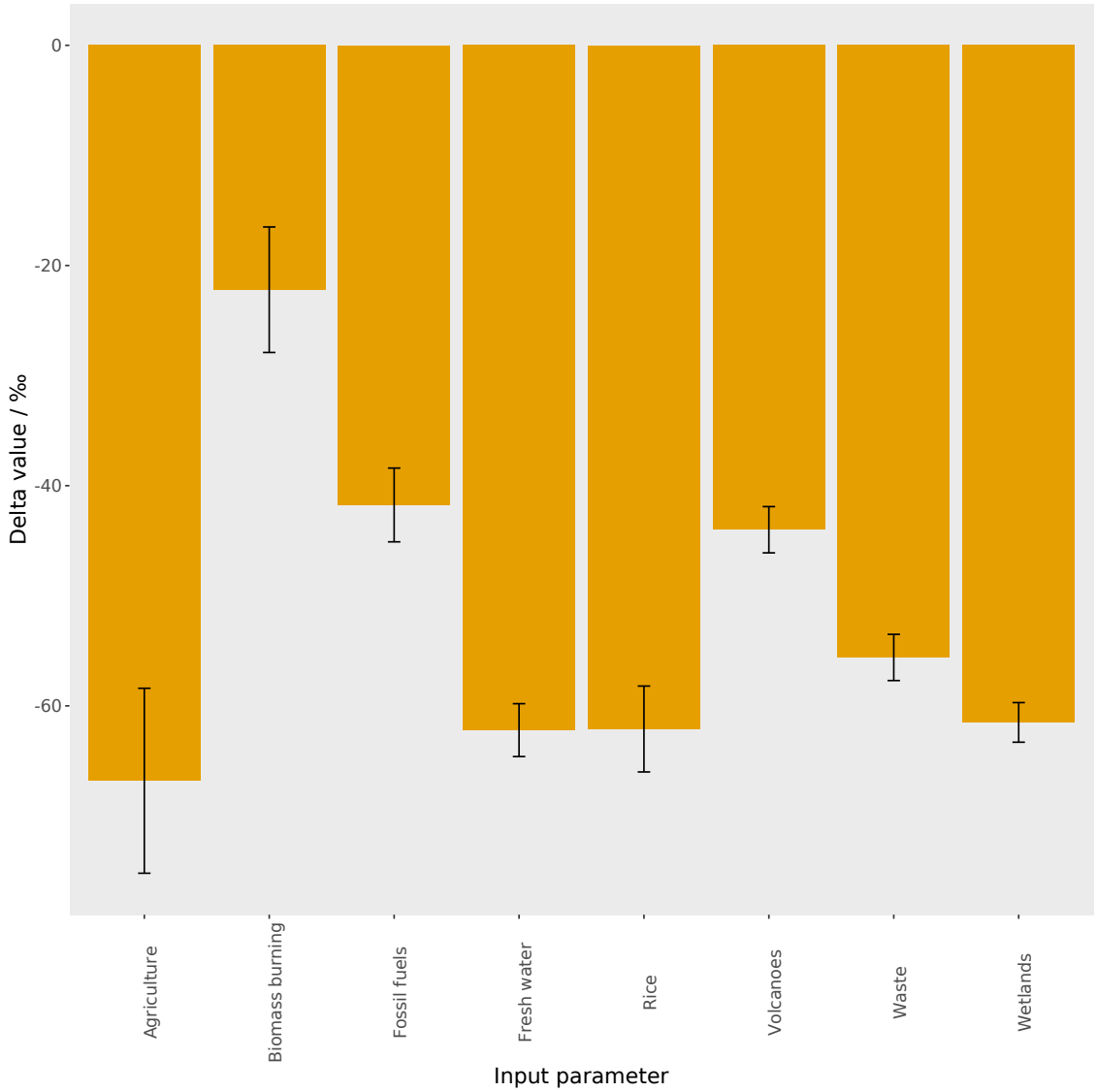

Figure 1.4.3: The mean source δ^{13}C-CH_4 values for the sources used in this work and the ranges explored in this work as error bars, based on Schwietzke et al. (2016) (see Section 2.3.1 for further details).

The methane released into the atmosphere is further fractionated by the isotopologues' different reaction rates with the sinks (e.g. Saueressig et al. (2001)). This isotopic fractionation is described by the kinetic isotope effect (KIE), which is defined as

$$KIE = \frac{k_{12}}{k_{13}}, \tag{1.10}$$

where k_{12} is the reaction rate constant of $^{12}CH_4$ and k_{13} is the reaction rate constant

of $^{13}CH_4$. The KIEs for the losses of methane used in this work are: 1.0039 for OH, 1.021 for soil, 1.0402 for the stratosphere, and 1.065 for Cl (more details on the origin of these values are given in Section 2.2.4). Whilst OH is the dominant sink that affects the methane mole fraction, Cl is by far the most fractionating, and so can have a very important impact on the atmospheric δ^{13}C-CH_4 (e.g. Allan et al. (2007), Thanwerdas et al. (2019)).

The δ^{13}C-CH_4 in the atmosphere is measured by the Institute of Arctic and Alpine Research (INSTAAR) at some of the NOAA stations, shown in Figure 1.4.4 (White et al. 2018). Other groups have also measured δ^{13}C-CH_4, such as Royal Holloway, University of London, and the University of Heidelberg (Nisbet et al. 2016, 2019), but it is the INSTAAR data that will be used in this thesis. The methane must first be separated from the rest of the sample, then the isotopologues can be separated using a mass spectrometer. In the mass spectrometer, methane molecules are first ionised and then accelerated. They are then passed through a magnetic field that deflects them according to their mass, with the lightest being deflected the most. The strength of the magnetic field can be adjusted so that different masses reach the detector, separating the isotopologues. The uncertainty in these values is calculated as the standard deviation in ten runs of a tank of air with a well characterised methane isotopic value (Miller et al. 2002, White et al. 2018).

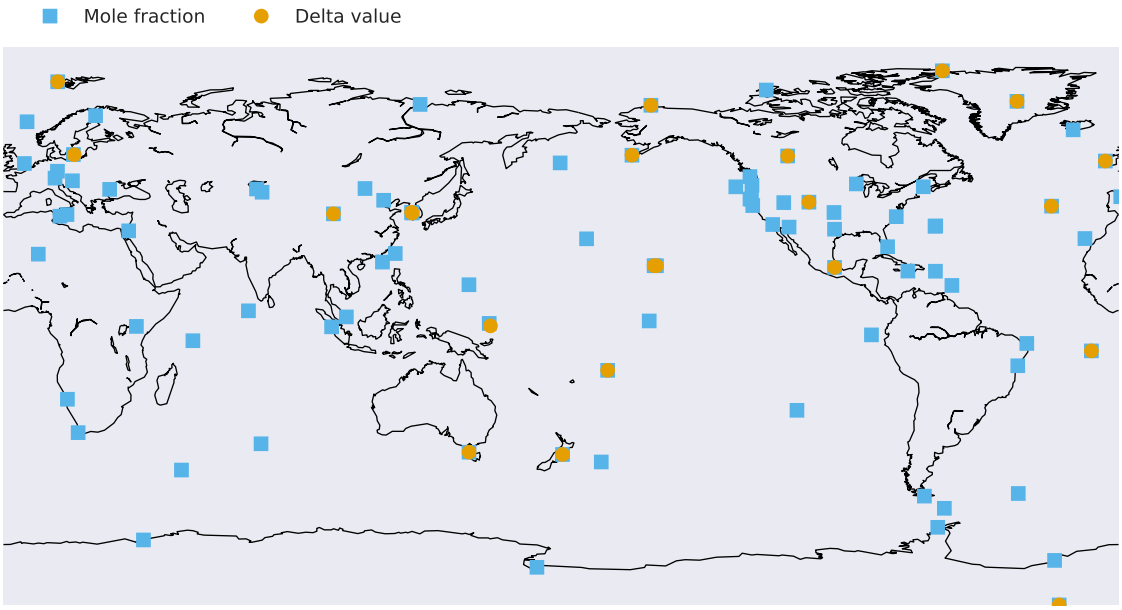

Figure 1.4.4: The locations where INSTAAR has taken δ^{13}C-CH_4 measurements (orange circles) (White et al. 2018), alongside the NOAA "surface discrete" stations (Dlugokencky et al. 1994) that measure the methane mole fraction (blue squares), plotted at average longitude and latitude.

These measurements from the different stations can be combined to a sine-latitude weighted global mean δ^{13}C-CH_4 shown in Figure 1.4.5. This value has become more negative since the renewed methane growth in 2007 (e.g. Nisbet et al. (2016, 2019)), the potential causes of which are discussed in Section 1.7.

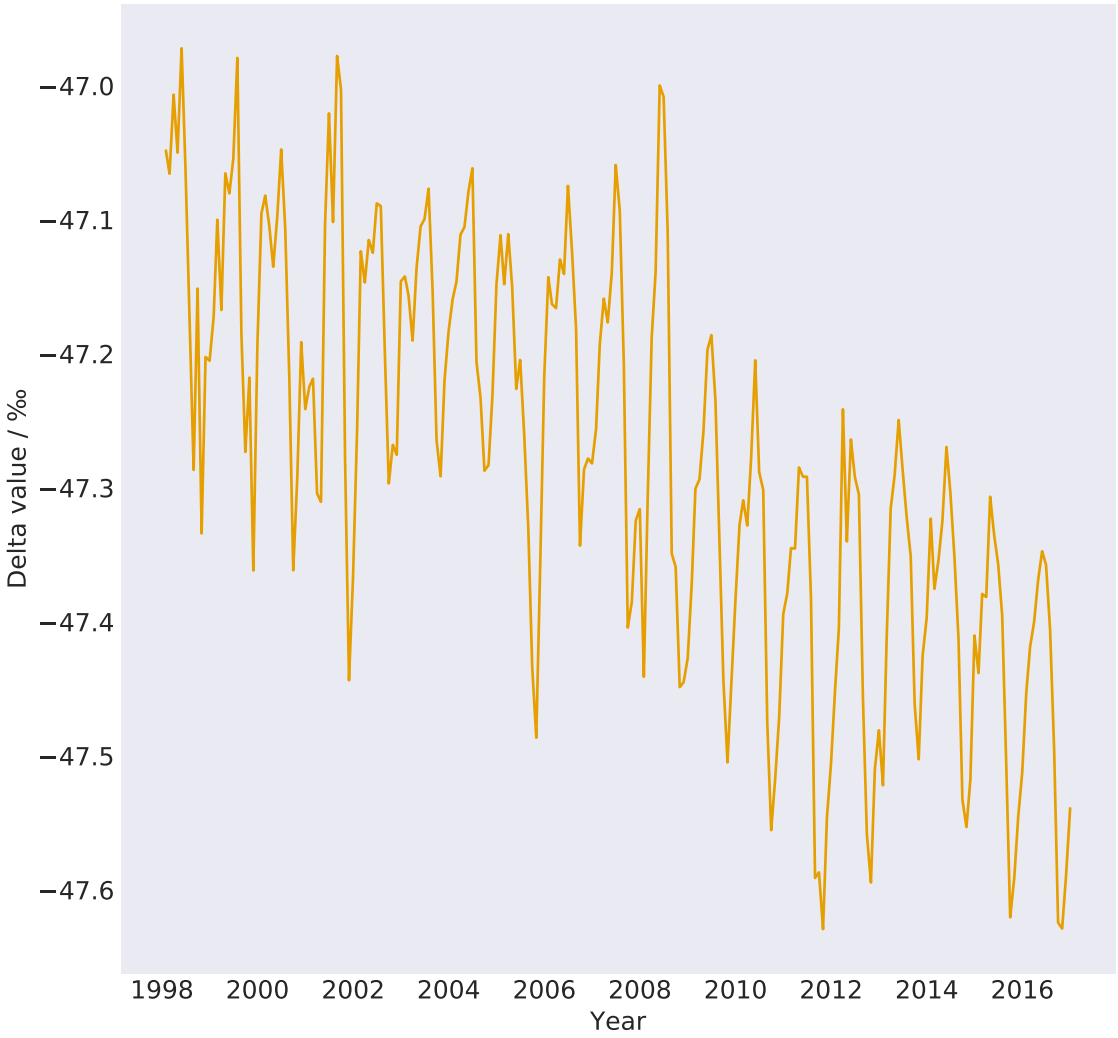

Figure 1.4.5: The measured sine-latitude weighted global mean atmospheric δ^{13}C-CH_4 from INSTAAR's surface measuring stations (White et al. 2018). A monthly mean was calculated for each station, and these were combined using a sine-latitude weighting to give a global mean.

There are other isotopologues of methane that could prove useful for constraining the methane budget: CH_3D and $^{14}CH_4$ (e.g. Bergamaschi et al. (1998), Quay et al. (1999), Hmiel et al. (2020)). $^{14}CH_4$ can be used to trace geological methane emissions (either from volcanoes or fossil fuel extraction), and CH_3D can be used to distinguish methane from the different emission pathways. However, there are very few measurements of these isotopologues and so, for now, they reveal little on a global scale.

1.4.4 Tracer gases for methane emissions from a particular source

Measurements of the mole fraction of other gases can also inform us about the magnitude of methane emissions from a particular source. If another gas is emitted with methane from a particular source, and that gas's sources and losses are well-characterised, then the mole fraction of the other gas can provide some additional information on the amount of methane coming from that source.

For example, ethane is co-emitted with methane in fossil fuel, biofuel combustion, and biomass burning sources (Rudolph 1995), and can be used (in combination with other gases) to infer changes in these methane sources (e.g. Simpson et al. (2006), Xiao et al. (2008), Hausmann et al. (2016)). Ethane has a lifetime of months (Rudolph 1995) compared to methane's years, which means it is less well-mixed than methane in the atmosphere and can offer information on emissions on a different timescale. However, there are large regional variations in the ratio of ethane to methane emissions from fossil fuels (Rudolph 1995), which limits the usage on a global scale.

1.5 Atmospheric modelling

As briefly described above, atmospheric observations in combination with atmospheric models, can provide estimates of the magnitudes of and changes in methane sources and sinks in top-down approaches. Initial estimates of the distribution of sources and sinks are input to the model (which simulates the emission, transport, and removal of methane from the atmosphere) and a distribution of methane in the atmosphere is output. This output can be compared to observations, and the sources and sinks adjusted to better match the data in a process often referred to as inverse modelling.

There are two types of transport models: Eulerian and Lagrangian. Eulerian models have a fixed grid and the gases are transported and chemically react based on the

conditions in each grid cell, whereas Lagrangian models calculate the transport and chemistry from the perspective of the released gases rather than the perspective of a fixed grid. In this thesis, a Eulerian model is used.

1.5.1 Three-dimensional chemical transport models

A three-dimensional chemical transport model (CTM) takes meteorological data, such as wind, temperature, and pressure fields, from general circulation models or meteorological analyses, which are used to transport chemical species of interest through the atmosphere. These models typically have a high spatial resolution, with the three-dimensional CTM used in this thesis able to split the atmosphere into hundreds of thousands of grid cells. This means that these models are computationally expensive compared to simpler two-dimensional box models.

1.5.2 Two-dimensional box models

The computational expense of a three-dimensional CTM is an issue if the model needs to run multiple times. For repeated model runs with limited computational resources, the two-dimensional box model excels. A two-dimensional box model splits the atmosphere into a small number of grid cells within which zonal mean concentrations are calculated (e.g. Rigby et al. (2008, 2017), Turner et al. (2017)). They are simple to set up, easy to understand, and computationally cheap. However, these models are generally limited by a lack of interannual variation in transport (provided by the meteorological data in three-dimensional CTMs) and much lower spatial resolution than three-dimensional CTMs. Naus et al. (2019) found that while box model parameters could be tuned to match a three-dimensional CTM-derived methane mole fraction trend, some bias remained.

1.5.3 Set up of atmospheric models

There are many inputs required to model methane in the atmosphere using a three-dimensional CTM, such as emission fields for the different sources, loss fields for

the chemical species that methane reacts with, and an initial methane mole fraction (and δ^{13}C-CH_4 if used) throughout the atmosphere. This section outlines the general features of these inputs.

Methane emission maps

Each source will emit methane from different locations at different times in different amounts. This can be input to the model as a two-dimensional map (assuming all emissions are from the lowest model level), calculated from the methods in Section 1.3.1. Some examples of frequently used emissions maps are GFED for biomass burning (van der Werf et al. 2010), WetCHARTs for wetlands (Bloom et al. 2017), and EDGAR for anthropogenic sources (Crippa et al. 2018). There are uncertainties in the spatial distribution, timing, and amount of methane emitted by different sources, and some studies have tried to quantify this (e.g. Bloom et al. (2017)), but generally uncertainties in these emissions maps remain poorly quantified.

Chemical loss species fields

A three-dimensional field is used to describe the concentration of the gas species that methane reacts with. This can be calculated using the methods described in Section 1.3.2. One of the most frequently used OH fields is from Spivakovsky et al. (2000), which is a climatology (a representation of the distribution in a typical year, ignoring interannual variations) calculated by a photochemical model informed by observations of OH precursors and tuned to match the methyl chloroform trends (Section 1.3.2). Similar approaches have been carried out for the stratospheric and Cl loss fields (e.g. Velders (1995), Patra et al. (2011), and Sherwen et al. (2016) have been used in this work). However, as soil loss only occurs at the surface, it is put in as negative emissions in this work.

Initial conditions

An initial three-dimensional field of methane mole fraction is required to begin the simulation. This is generally created by spinning the model up. Spin-up is

the process of running the model in order to reach a methane mole fraction (and any other measurements used) that is similar to that observed before the start of the simulation that will be analysed. This is often done with annually repeating emissions, losses, and meteorological fields because there are not estimates that go far enough back in time to create realistic methane mole fraction and δ^{13}C-CH_4 distributions.

1.6 Inverse methods

Inverse methods are used to infer the sources and sinks of methane from the atmospheric methane measurements using a model of atmospheric transport. The method often used is a Bayesian approach to statistical inference, which is outlined in this section. The model output and observations can be compared using Equation 1.11:

$$\boldsymbol{y} = F(\boldsymbol{x}) + \epsilon. \tag{1.11}$$

The model (F) is used to map a set of inputs ($\boldsymbol{x}$), that describe the sources and sinks of methane, onto an output methane mole fraction. However, there will be a mismatch between the observed atmospheric methane mole fraction ($\boldsymbol{y}$) and the model output due to imperfections in the model and measurement uncertainty, which is accounted for by the error term ϵ.

Starting from an initial guess at the model inputs, the inputs can be adjusted so that the model output better matches the observations using Bayes' Theorem:

$$P(\boldsymbol{x}|\boldsymbol{y}) \propto P(\boldsymbol{y}|\boldsymbol{x})P(\boldsymbol{x}). \tag{1.12}$$

The prior belief of the model inputs is described by the probability distribution function $P(\boldsymbol{x})$. This should be independent of the observations, and is informed by the range of bottom-up emissions estimates. $P(\boldsymbol{y}|\boldsymbol{x})$ is the likelihood function and describes how likely the model output is to be consistent with observations for

a set of model input values, which will depend on the error term ϵ from Equation 1.11. The posterior probability function $P(\boldsymbol{x}|\boldsymbol{y})$ describes the probability of the input parameters based on the observations (and their uncertainties) and the prior probability of the input parameters.

In order to find the optimal model input parameters, the value of $\boldsymbol{x}$ which maximises the probability of $P(\boldsymbol{x}|\boldsymbol{y})$ must be found. In a less statistical setting, this means that the cost function ($J(\boldsymbol{x})$),

$$J(\boldsymbol{x}) = (\boldsymbol{y} - F(\boldsymbol{x}))^T \boldsymbol{R}^{-1} (\boldsymbol{y} - F(\boldsymbol{x})) + (\boldsymbol{x} - \boldsymbol{x}_i)^T \boldsymbol{P}^{-1} (\boldsymbol{x} - \boldsymbol{x}_i), \tag{1.13}$$

must be minimised. Here, $\boldsymbol{x}_i$ is the initial input parameter vector, and $\boldsymbol{R}$ and $\boldsymbol{P}$ are the covariance matrices of the observations and the prior respectively. Further details on the method can be found in Tarantola (2005).

Another inverse method is history matching, the iterative process of adjusting model inputs until the output closely matches observations. This involves identifying, and removing, regions of the parameter space that are unlikely to match the observations, allowing more likely regions to be better sampled. This method is used in this thesis and is further discussed in Section 1.8.3.

1.7 Possible drivers of recent change in the global methane budget

This thesis focuses on the recent plateau and subsequent growth in methane mole fraction as it is one of the most well-studied periods with plentiful atmospheric data. Previous studies use different methods, different assumptions, and different models to come to different conclusions about the cause of these observations, with uncertainty ranges that do not overlap. In this section, some of these studies are examined to demonstrate the uncertainties surrounding the determination of the methane budget.

1.7.1 Estimates from bottom-up methods

Bottom-up studies suggest many different sources that could explain some or all of the recent observations. For example, Bousquet et al. (2011) used a bottom-up wetland process model to infer positive global methane emission anomalies for the years 2006 to 2008 (compared to 1999-2006). Although the wetland emissions anomaly in the latitude band 30-50 °N was close to zero, so this increase was driven by wetlands outside of this band. A similar positive global methane emission anomaly is presented in Bloom et al. (2017), who used an ensemble of wetland process models to estimate wetland emissions for 2001-2015. However, this study does not see a consistent wetland emission year-to-year increase beyond 2008, though the emissions remain higher than during the methane plateau.

Anthropogenic sources have also been suggested to have played a key role in the change of the methane growth rate. EDGAR 4.2 (Crippa et al. 2018) is an anthropogenic emission inventory that includes emission estimates for many anthropogenic methane sources. This inventory suggests that the cause of the plateau is reduced fossil fuel emissions during the late 1990s and early 2000s. Crippa et al. (2018) also explains the renewed growth in methane by increasing fossil fuels, alongside agriculture, and waste.

1.7.2 Estimates from observations alone

Some studies infer changes in the methane budget using the observations alone (Section 1.4). For example, Simpson et al. (2006) uses the mole fraction of methane, alongside ethane (C_2H_6) and tetrachloroethene (C_2Cl_4) to look at the influence of biomass burning on fluctuations in the methane growth rate. Both C_2H_6 and C_2Cl_4, like methane, are predominantly removed from the atmosphere by reaction with OH. C_2H_6 is emitted with methane by fossil fuels and biomass burning, whereas C_2Cl_4 is only released by industrial solvent emissions. Therefore, changes in both methane and C_2H_6 mole fractions could be caused by either changes in OH, fossil fuels, or biomass burning. The C_2Cl_4 mole fraction offers a way to differentiate sink

or source changes, as if changes in C_2Cl_4 are uncorrelated with changes in CH_4 and C_2H_6, it would suggest that emissions, rather than OH, have changed. This study concludes that many of the fluctuations in the methane growth rate between 1996 and 2004 were due to changes in biomass burning.

Dlugokencky et al. (2009) examines the methane mole fraction and δ^{13}C-CH_4 measurements across the NOAA network, and concluded that high latitude northern hemisphere wetlands were a key contributor to the renewed methane growth in 2007. This is because the methane mole fraction at the most northerly station in the network increased more than the global average and global δ^{13}C-CH_4 became more negative. However, Bousquet et al. (2011) challenges this conclusion as transport in the tropics is vertically efficient, whereas transport at high latitudes in horizontally efficient. This means that an emissions release in the tropics will result in a smaller rise in the methane mole fraction at the surrounding surface stations than for the high latitudes. This demonstrates a key issue in inferring methane fluxes from surface atmospheric data alone, as atmospheric transport can have a large effect on what is observed. Therefore, many studies have combined the atmospheric observations with an atmospheric model in order to infer changes to the methane budget, and these studies will be discussed in the following section.

1.7.3 Estimates using observations and models

Estimates using three-dimensional chemical transport models

Three-dimensional CTMs (Section 1.5.1) are computationally expensive and inverse methods (Section 1.6) require repeated model runs, which are often unfeasible. This issue can be overcome by using model-derived sensitivities of modelled outputs to changes in sources or sinks instead of the model itself. These sensitivities can be multiplied by a small change in the parameters to calculate the change in the output methane mole fraction and δ^{13}C-CH_4 from an existing model simulation. Four examples are discussed here: use of the adjoint model in Bousquet et al. (2011), Bergamaschi et al. (2013), and Rice et al. (2016); and linear sensitivities have also

been calculated using finite difference approaches for basis function decompositions of the source or loss fields (e.g. in McNorton et al. (2018)). The adjoint calculates the sensitivity of the model output to the inputs for a particular set of input values. This sensitivity can be used instead of the model F in Equation 1.11, allowing an analytical solution for the optimal parameters, or the sensitivity can be iteratively calculated in order to find the nearest minimum in the cost function (Equation 1.13) by gradient descent.

Adjoint models can be hard to code and are fixed to one particular model version, so are not widely applicable. It is also hard to estimate the uncertainty in the predicted fluxes when using the adjoint and they usually assume prior parameter distributions are Gaussian. Despite these limitations, adjoint models are powerful tools because they can solve for thousands of parameters (e.g. monthly emissions from every grid cell) and three examples are explored here. The first is Bousquet et al. (2011), who used the methane mole fraction measurements from 68 surface stations and the adjoint of a three-dimensional CTM to infer that the renewed methane growth in 2007 was caused by increased tropical wetland emissions. Two different inversion methods were presented in the study, which were shown to agree well on a global scale. One inversion gives information on the monthly emissions from different source types in 11 large regions, whereas the other infers the total weekly fluxes from each grid cell, demonstrating the vast number of input parameters possible for adjoint models. However, this study does not include δ^{13}C-CH_4 measurements, so source attribution is potentially limited. Additionally, the OH concentration is not solved for in the inversion (although OH is interannually varying, consistent with methyl chloroform observations), ignoring a large source of uncertainty.

Bergamaschi et al. (2013) uses the adjoint of a different three-dimensional CTM, with satellite data in addition to the surface station data. The inversion infers the monthly emissions in each grid cell for four different source types, and is repeated for nine different settings that include different observations, satellite bias corrections, bottom-up inventories, and OH distributions. This study infers that the renewed methane growth comes predominantly from the tropics and the mid-latitudes of the

northern hemisphere, where fluxes from anthropogenic sources increased. However, the derived increase is smaller than the EDGAR 4.2 trend. Wetland emissions also increased around 2007 in high northern latitudes and the tropics, qualitatively similar to Bousquet et al. (2011), but this was not sustained in later years. Whilst all inversions performed in this study are broadly consistent, there are significant differences in the inference using just the surface station data or both the surface station and satellite data. This is particularly so in the tropics, where the satellite can provide more constraint, though the authors stress the potential influence of satellite biases on satellite inferred fluxes. Like Bousquet et al. (2011), this study does not include δ^{13}C-CH_4 measurements, and the OH concentration is interannually repeating in the inversion.

Rice et al. (2016) uses methane mole fraction and δ^{13}C-CH_4 surface measurements, alongside an adjoint model, to infer monthly emissions in ten source categories covering different source types and locations. 53 perturbed inversions are used as sensitivity tests to quantify the uncertainty in the results, with all inversions being broadly consistent. This study concludes that the plateau in methane concentrations and subsequent regrowth was primarily due to the levelling off and then growth in anthropogenic sources (like Bergamaschi et al. (2013)), predominantly gas and oil, but with contributions from coal, ruminants, and waste. This work also infers decreasing biomass burning emissions over the previous decades, and decreasing wetland emissions during the renewed methane growth in 2007, unlike the two previously described adjoint model studies. In a further difference to the previous studies, a fixed-lag Kalman smoother was used to reduce the computational burden, meaning that only 11 months of observations (not the whole time series) is used to infer the fluxes. This has been shown to infer relatively consistent fluxes to mole fraction inversions using all observations (Bruhwiler et al. 2005), but may have a larger impact on the inference from δ^{13}C-CH_4 measurements which take a long time to propagate (Tans 1997). This study also does not solve for OH, the most uncertain term in the methane budget, and whilst δ^{13}C-CH_4 measurements were included, the source δ^{13}C-CH_4 signatures were not optimised.

McNorton et al. (2018) estimated OH in their inversion, using the methane mole fraction and δ^{13}C-CH_4 surface measurements, and the linear sensitivities of a three-dimensional CTM. Linear sensitivities present a problem because the loss of methane depends on the amount of methane as well as the removal species (e.g. OH), so the effect on the methane mole fraction is non-linear with respect to the concentration of the removal species. This study also performs independent inversions for each year, so December emissions are constrained by only one month of observations whereas January emissions are constrained by twelve. However, the response of the model will not just depend on emissions from that year, but for a time before that, possibly decades for the δ^{13}C-CH_4 measurements (Tans 1997). This inversion solves for monthly emissions from different source types in five large regions and monthly global OH. This study inferred that the renewed growth in methane in 2007 was caused by a combination of decreased OH, increased energy sector emissions (mainly in Africa and the Middle East and southern Asia and Oceania), slightly increased wetland emissions (mainly in northern Eurasia), and slightly decreased biomass burning emissions. δ^{13}C-CH_4 measurements were shown to add valuable constraint, but source δ^{13}C-CH_4 signatures are fixed, as is the Cl sink, so the uncertainties are likely underestimated.

Estimates using two-dimensional box models

A popular alternative to the three-dimensional CTM is a two-dimensional box model, which is a much simpler representation of the atmosphere, but is less computationally expensive than a three-dimensional CTM. As a result, many inverse methods used to find methane fluxes have used this type of atmospheric transport model. However, generally there is no interannual variability in transport and a limited spatial resolution in these models. The limited spatial resolution means that only a zonal mean of the observations can be used, rather than individual measurement stations, and so source attribution relies on δ^{13}C-CH_4 or tracers such as ethane.

The first model discussed in this section is the two-dimensional box model in Nisbet et al. (2016), which uses four latitude bands, and surface measurements of the

methane mole fraction and δ^{13}C-CH_4 to infer the monthly emissions and losses of methane. This study concludes that biogenic emissions, probably tropical wetlands, are the most likely cause of the renewed methane growth in 2007 (like Bousquet et al. (2011)). However, this study only predicts the total flux and the total δ^{13}C-CH_4 source signature rather than the different source types, making objective source attribution difficult. Also two separate inversions are performed to solve for emissions and losses, so the possibility of combined source and sink changes is not covered.

Schaefer et al. (2016) used a one-box model with surface measurements of methane mole fraction and δ^{13}C-CH_4 to infer the total annual emissions of methane. In this study, an inversion is used to fit the data until 1993 to investigate the plateau, and until 2007 to investigate the renewed growth. The model is then run forward using the derived base source, which is perturbed to test how changing total emissions and total source δ^{13}C-CH_4 matches the changes in the observations. From this they infer that the plateau in methane mole fractions was caused by decreasing fossil fuel emissions, and the renewed growth was driven by biogenic sources, probably agriculture. Using the interannual variability in OH derived from methyl chloroform improves the fit of the perturbations to the observations, but the impact of varying OH further was not investigated. Both Nisbet et al. (2016) and Schaefer et al. (2016) provide subjective estimates of the cause of the renewed growth from their inferred source δ^{13}C-CH_4 but without considering the possibility that multiple source changes could have occurred. For example, biomass burning is a minor source but has a much less negative δ^{13}C-CH_4, so decreasing this source would allow another source, such as fossil fuels to increase and produce a declining δ^{13}C-CH_4 (as in Rice et al. (2016), McNorton et al. (2018)).

Hausmann et al. (2016) use a two-box model covering the two hemispheres alongside methane and ethane mole fraction observations to infer annual fossil fuel methane emissions. Fossil fuel emissions were found to increase significantly during the period of renewed methane growth (like Bergamaschi et al. (2013), Rice et al. (2016), McNorton et al. (2018)). However, this study assumes that all the ethane changes are due to fossil fuels, when biomass burning or OH changes could have contributed.

Additionally, only the modelled output and observations of one surface station is used, and a linear trend in fossil fuel emissions is assumed.

Worden et al. (2017) inferred biomass burning methane emissions decreased after the renewed growth in 2007, using carbon monoxide as a tracer for biomass burning methane emissions and an adjoint model. This biomass burning emission is input to a one-box model, and the fossil fuel and biogenic emissions are adjusted to broadly match surface observations of the methane mole fraction and δ^{13}C-CH_4. This decrease in biomass burning allows for increased fossil fuel emissions and wetlands to drive the renewed methane growth and be consistent with the δ^{13}C-CH_4 observations, (like Rice et al. (2016) and McNorton et al. (2018)). This study did not allow OH to vary, and used a box model method that assumes a linear trend in emissions from 2007.

Rigby et al. (2017) and Turner et al. (2017) use different hemispheric box models with surface measurements of methane mole fraction, δ^{13}C-CH_4, and methyl chloroform mole fraction to infer the annual changes in hemispheric methane emissions, source δ^{13}C-CH_4, OH concentration, and methyl chloroform emissions. Both studies conclude that OH could have played a key role in the plateau and renewed growth of methane (like McNorton et al. (2018)), but the uncertainties are large. These studies use different methods to thoroughly sample the possible parameter space, which allows a more complete exploration of the uncertainty in the optimal parameters than the analytical solution or gradient descent to a local minimum. Both carried out inversions with fixed OH, which required a sudden increase in emissions in 2007 to match the observed increase in methane mole fraction, unlike when OH is optimised. In Rigby et al. (2017) the model is also run forward with the derived OH concentration which can also explain the increase in ethane mole fraction that Hausmann et al. (2016) attributed to fossil fuel emissions. There are differences in the most likely results of these two studies: Rigby et al. (2017) infer gradually increasing methane emissions from 2007, whereas Turner et al. (2017) infer a decrease. Their conclusions demonstrate that the problem is underdetermined and the solutions depend on the assumptions made.

Summary of possible drivers of observed methane mole fraction changes

The results of these studies provide many different possible changes in the methane budget that explain the atmospheric observations, with uncertainty ranges that do not overlap. This suggests that, in general, the problem is under-determined and the uncertainties are under-estimated. As suggested in Turner et al. (2017), the results of many of these studies are dependent on the prior assumptions. For example, studies that optimise OH tend to find that OH has decreased since 2007 (Rigby et al. 2017, Turner et al. 2017, McNorton et al. 2018). Whereas, studies that optimise biomass burning tend to find that biomass burning has decreased (Rice et al. 2016, Worden et al. 2017, McNorton et al. 2018), which allows fossil fuels to increase and still produce a declining δ^{13}C-CH_4. Studies that optimise many source categories tend to infer changes in a mixture of sources and sinks (Rice et al. 2016, McNorton et al. 2018). Whereas studies that solve for a total methane source and total δ^{13}C-CH_4, without optimising OH and biomass burning, tend to conclude that biogenic emissions have increased (Nisbet et al. 2016, Schaefer et al. 2016).

Therefore, in order to learn more about the methane budget, we need to use as much of the available data and the most accurate atmospheric model possible, with a thoroughly quantified uncertainty estimate. Many global methane inversions have been done with box models, which generally have a low spatial resolution and lack interannual variability in transport. This prevents surface station data being fully utilised as the data must be combined to a zonal mean. This hinders inference on the changes in different source types, which have different spatial distributions and so the observations at different stations change at different times. These problems can be avoided by using a three-dimensional CTM, however these models are so computationally expensive that linear sensitivities or adjoint code, rather than repeated runs of the model, must be used. However, neither of these methods allows a thorough exploration of the parameter space and it is difficult to quantify the uncertainties. Additionally, linear sensitivities do not account for the non-linearity in methane losses; and adjoint code is not widely available and Gaussian assumptions usually have to be made. There is, however, a way to produce the three-dimensional

CTM output but at the speed of the box model, with a reliable uncertainty estimate: the Gaussian process emulator. This method is described in Section 1.8, and this thesis demonstrates how to apply Gaussian process emulation to estimate the methane sources and sinks from the observations.

1.8 The basics of Gaussian process emulation

The problem of efficiently estimating the relationship between uncertain inputs and observable outputs of a complex model has been explored in other research communities using emulation. An emulator is a statistical approximation to a more complex model, often using a Gaussian process (O'Hagan 2006, Ebden 2015). This technique has been applied to a large variety of scientific problems, for example: parameter optimisation in models describing galaxy formation (Vernon et al. 2010), influenza epidemics (Farah et al. 2014), and the Greenland ice sheet (Chang et al. 2014); uncertainty quantification in the biospheric carbon flux (Kennedy et al. 2008), aerosol effective radiative forcing (Regayre et al. 2018), and concentrations of cloud condensation nuclei (Lee et al. 2012); and sensitivity analysis in aerosol models (Lee et al. 2011).

1.8.1 A one-dimensional example

In this work, a Gaussian process is used as the emulator. This is a form of non-parametric curve fitting, the mathematics of which is explained in Section 1.8.2. The Gaussian process method is illustrated here by a simple one-dimensional example, shown in Figure 1.8.1. In order to build a Gaussian process, a set of known complex computer simulator outputs are required (the blue points in Figure 1.8.1), this is known as the training dataset. The Gaussian process effectively interpolates between the training points to enable prediction of the simulator output at untested inputs. The method not only predicts the simulator output value (the black line in Figure 1.8.1), but also estimates the error in the prediction (the grey shading in Figure 1.8.1), which depends on how close the test input is to the training dataset.

The orange point in Figure 1.8.1 is the Gaussian process prediction of an unknown complex computer simulation output and the orange bar represents the error in the prediction. The error in this prediction is large because it is not bounded by training data points. In this work, such errors are avoided by not allowing prediction outside of the range of the training dataset.

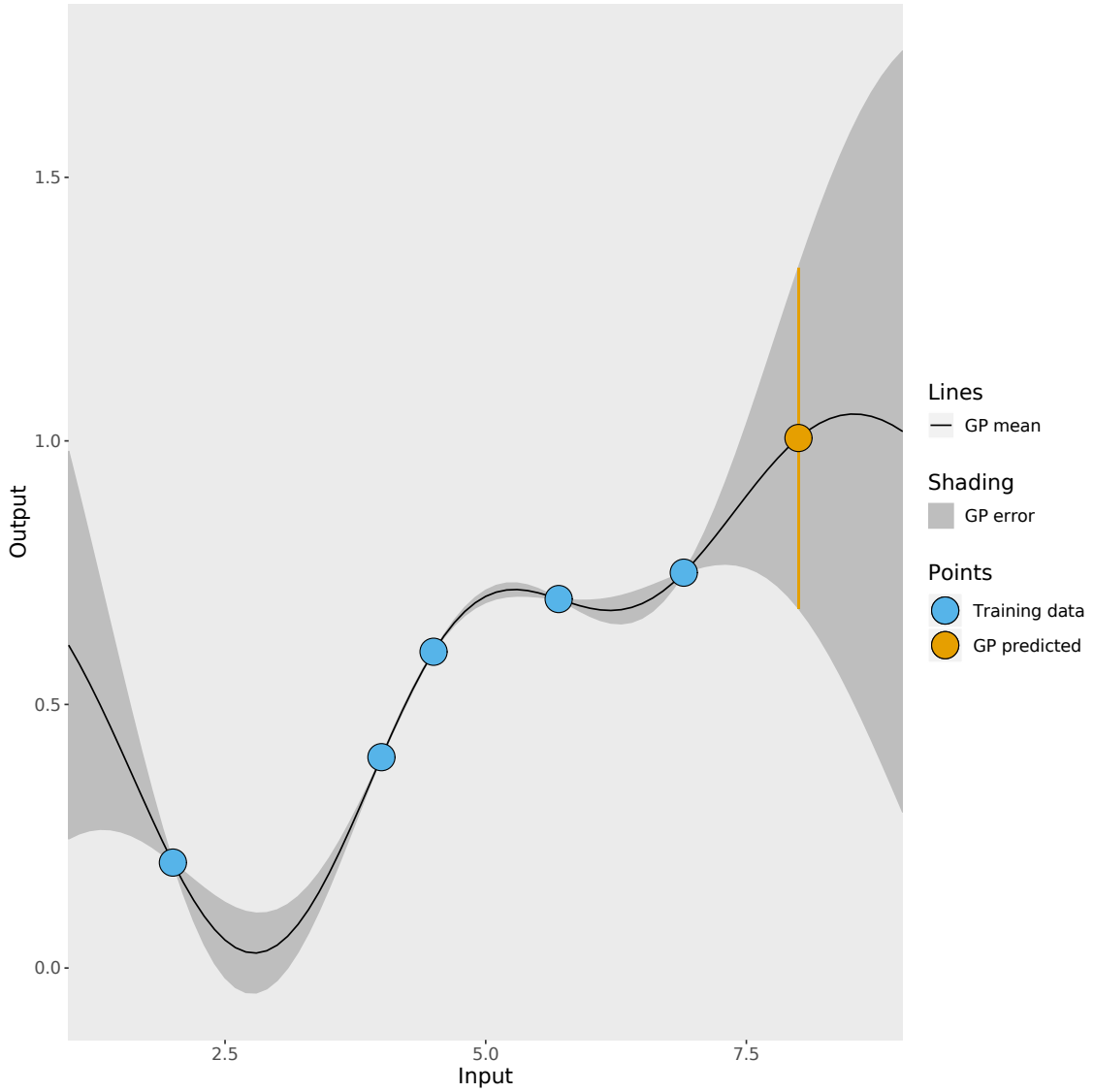

Figure 1.8.1: A simple one-dimensional example of a Gaussian process (GP). The blue points represent known outputs of the complex computer simulation, and the black line is the mean of the Gaussian process which interpolates between the known outputs. The error in the prediction is represented by the grey shading. The orange point is the Gaussian process prediction of an unknown complex computer simulation output and the orange bar represents the error in the prediction.

1.8.2 The mathematics of Gaussian process emulation

Gaussian process emulation predicts an output value for a set of untested input parameter values, given a training set of corresponding inputs and outputs. There are other common techniques that could be used if the form of underlying function that maps inputs to outputs is known. For example, linear regression if the underlying function is linear, or polynomial fitting if the underlying function is a polynomial. Gaussian process emulation achieves the same outcome but does not assume the form of the underlying function. It requires only one main assumption: the outputs follow a multivariate Gaussian distribution.

The Gaussian process is defined by its mean and covariance functions. It is often sufficient to assume that the mean function is zero, though in this work, the mean function is a multiple linear regression as the system is close to linear. The covariance function is a measure of how similar input sets are, and decays as the distance between the inputs increase. There are several widely used covariance functions, and the choice depends on the assumptions being made. The most popular is the squared exponential, which works well for smooth functions. This covariance function is used in this work as there are no discontinuities or sharp changes in the methane observations due to input parameter variation. The $(i,j)^{\text{th}}$ element of the covariance matrix (K) is given by

$$\eta_{ij} = \sigma_f^2 \exp\left(-\sum_{k=1}^{m} \frac{(x_{k,i} - x_{k,j})^2}{l_k^2}\right), \tag{1.14}$$

where the maximum covariance is σ_f^2, x_k is the value of the k^{th} input parameter, and l_k is the length scale parameter to be optimised during training.

In order to predict an output value $(\boldsymbol{y}*)$ at a new set of input parameters $(\boldsymbol{x}*)$, the fact that the output is a sample from the joint multivariate Gaussian distribution of the training data $(\boldsymbol{y})$ and the data to be tested is used:

$$\begin{bmatrix} \boldsymbol{y} \\ \boldsymbol{y}* \end{bmatrix} \sim \mathcal{N}\left(m(\boldsymbol{x}*), \begin{bmatrix} K(\boldsymbol{x},\boldsymbol{x}) & K(\boldsymbol{x},\boldsymbol{x}*) \\ K(\boldsymbol{x}*,\boldsymbol{x}) & K(\boldsymbol{x}*,\boldsymbol{x}*) \end{bmatrix}\right), \tag{1.15}$$

where m is the mean function and $\boldsymbol{x}$ is the training dataset inputs. This means that the expected value of $\boldsymbol{y}*$ is

$$E(\boldsymbol{y}*) = m(\boldsymbol{x}*) + K(\boldsymbol{x}*, \boldsymbol{x})K(\boldsymbol{x}, \boldsymbol{x})^{-1}\boldsymbol{y}, \tag{1.16}$$

and the uncertainty, in terms of variance, in the estimate is

$$V(\boldsymbol{y}*) = K(\boldsymbol{x}*, \boldsymbol{x}*) - K(\boldsymbol{x}*, \boldsymbol{x})K(\boldsymbol{x}, \boldsymbol{x})^{-1}K(\boldsymbol{x}, \boldsymbol{x}*). \tag{1.17}$$

The Gaussian process method is further described in Rasmussen & Williams (2006), and some simple tutorials are available in O'Hagan (2006) and Ebden (2015).

1.8.3 History matching

History matching is the iterative process of adjusting the inputs of a model until it closely matches observations. This technique has been widely used. For example, in oil reservoir modelling (Craig et al. 1996, 1997) the inputs of an oil reservoir model are tuned to match observed oil production and pressure profile of the well. History matching can be used in combination with Gaussian process emulation as in Vernon et al. (2010). Here, emulators are created and compared to observations, so that regions of the emulator input parameter space can be ruled out as implausible. A new set of emulators is then trained by running the complex model over this reduced parameter space, and these emulators will be more accurate over these parameter values. The process can be repeated as many times as required to find the plausible input space. This thesis applies this technique to the methane budget to demonstrate the range of plausible values of the methane sources and sinks, rather than the optimised values presented by the studies in Section 1.7.

1.9 Thesis motivation

Methane is an important greenhouse gas (Section 1.1), but the drivers behind recent atmospheric observations remain unexplained (Section 1.7). There have been

many studies that explore the possible reasons for the pause in growth during the early 2000s and the renewed growth since 2007, but no consensus has been reached, with sources and sinks such as OH, wetlands, agriculture, and fossil fuels all being implicated as key players. Many of these studies have been done using two-dimensional box models (Section 1.5.2), because they run so much faster than the three-dimensional CTMs (Section 1.5.1). However, this speed comes at a price: reduced spatial resolution and no interannual variability in transport. Those studies that do use a three-dimensional CTM by calculating linear sensitivities or using adjoint code, struggle to use the most accurate inversion methods and to do a comprehensive uncertainty estimate.

There is another way to speed up three-dimensional CTMs, that maintains the spatial resolution, includes the interannual variability in transport, and allows uncertainty to be estimated easily: a Gaussian process emulator (Section 1.8). The aim of this thesis is to apply this technique to gain understanding of the methane budget. This will be done using emulators that output the surface hemispheric mean methane mole fraction and δ^{13}C-CH_4 of the three-dimensional CTM, which effectively form a two-dimensional box model. This approach could also be extended to emulate the output of each three-dimensional CTM grid cell, but this is beyond the scope of this thesis.

There are limitations to this method too. It is only possible to explore about 30 model input parameters (whereas adjoint models can estimate thousands of parameters), so some parameters will have to be fixed and remain unexplored. In this work, spatial distributions and some temporal trends of sources and sinks were fixed, unlike many previous studies which group together similar sources in order to allow variation in spatial distributions and temporal trends. Ideally, all of these parameters would be allowed to vary as they are all uncertain. In this thesis, the decision was taken to primarily examine the uncertainty in the source types, as many sources that are lumped together (e.g. wetlands, fresh water, agriculture, and rice are often combined to a total biogenic source) have large uncertainties, very different spatial distributions, different temporal trends, and are controlled different factors. Ulti-

mately, if we are to reduce methane emissions, knowing the source type causing the growing methane mole fraction is vital.

Chapter 2 describes how a three-dimensional global CTM can be run repeatedly in order to create a training dataset for Gaussian processes that mimic the three-dimensional CTM output. How these emulators are trained and validated is presented in Chapter 3, before being used to investigate the methane budget. Two analyses to better understand the methane budget are conducted: a sensitivity analysis in Chapter 4 and the sources and sinks are constrained by matching to observations in Chapter 5.

Chapter 2

Development of a global atmospheric methane simulation and an emulator training dataset

2.1 Introduction

The aim of this thesis is to create and use emulators that approximate the hemispheric output of a three-dimensional global chemical transport model (CTM). The well-established Model for Ozone and Related Chemical Tracers (MOZART) (Emmons et al. 2010) was used for this purpose. However, a key benefit of the method developed here is that it could be readily applied to any CTM.

The generation of a simulation of the methane mole fraction and δ^{13}C-CH_4 using MOZART is discussed in Section 2.2. In Section 2.3, MOZART is used to generate 270 methane simulations with different source magnitudes, source δ^{13}C-CH_4 values, and sink magnitudes in order to create a training dataset (Section 1.8.1) for the Gaussian process emulators. The training dataset is compared to the observations in Section 2.4, and the observations are shown to lie within the envelope of the MOZART output ensemble. The model-measurement discrepancy error and the MOZART "invariant parameter error" are examined in Section 2.5. The invariant parameter error stems from holding some parameters constant in the training

dataset. As far as we are aware, this term has not been considered in other top-down methane studies. These observations and errors will become key in Chapter 5, where the emulators are used to compare methane simulations to the observations and implausible combinations of sources and sinks are ruled out.

2.2 Development of a global atmospheric methane model simulation

2.2.1 The chemical transport model setup

In this thesis, we create a set of emulators that provide a statistical approximation of the outputs of the MOZART model (Emmons et al. 2010), an offline, global three-dimensional CTM, for a set of uncertain inputs. In this work, 56 vertical model levels were used, from the Earth's surface to about 48 km. However, only the bottom six levels (up to about 1 km) were saved for analysis to reduce the storage space required. The model was run at 12.00 ° N × 11.25 ° W resolution, with MERRA reanalysis meteorological fields (Rienecker et al. 2011) for 1995 to 2012. The model's time step was one hour, with data output on a 6-hourly basis (consistent with the time step of the MERRA fields). In this work, the model's chemistry is offline, the effects of which are further discussed in Section 2.2.2.

The input parameters to MOZART that are explored in this work describe the methane sources and losses (Section 1.2), which are set up similarly to Ganesan et al. (2018). The sources parameterised in the model are: wetlands, fresh water, agriculture, rice, waste, fossil fuels, biomass burning, volcanoes, termites, hydrates, and oceans. The methane losses included are the reactions of methane with the hydroxyl radical (OH), tropospheric chlorine radicals (Cl), net stratospheric loss (due to reaction with Cl and $O(^1D)$), and methanotrophic loss in soils. The stratospheric loss is a weighted contribution of Cl and $O(^1D)$ with the ratio given in Saunois et al. (2016), and the soil loss is put into the model as negative emissions with fractionation calculated as in Lassey et al. (2007). A summary of the input fields used in

the model is given in Table 2.1.

For each MOZART simulation, the model was spun up (Section 1.5.3) from a steady state atmosphere for 30 years with repeating 1995 meteorology, and 1996 emissions and losses. Following spin up, the model was run for 1996-2012, with time varying meteorology and emission and loss fields. Only 2000-2012 was analysed to allow for any transient signals following spin-up. This time period was chosen to examine the cause of the renewed methane growth in 2007, with 2000 being an appropriate starting point because INSTAAR δ^{13}C-CH_4 data (Section 1.4.3) becomes available around this time.

Source	Reference	Temporal resolution	Years
Wetlands	Wetcharts (Bloom et al. 2017)	monthly	2001-2012 (1996 – 2000 are 2001 repeating)
Fresh water	This work (see Section 2.2.3)	annual	climatology
Agriculture	EDGAR 4.32 (Crippa et al. 2018)	annual	1996-2012
Rice	Yan et al. (2009)	monthly	2000 repeating
Waste	EDGAR 4.32 (Crippa et al. 2018)	annual	1996-2012
Fossil fuels (includes biofuel)	EDGAR 4.32 (Crippa et al. 2018)	annual	1996-2012
Biomass burning	GFED4s (van der Werf et al. 2010)	monthly	1997-2012 (1996 is the mean of all years)
Volcanoes	Etiope & Milkov (2004)	annual	climatology
Termites	Fung et al. (1991)	annual	climatology
Hydrates	Fung et al. (1991)	annual	climatology
Oceans	Lambert & Schmidt (1993); Houweling et al. (1999)	annual	climatology
Loss			
OH	Spivakovsky et al. (2000)	monthly	climatology
Stratosphere	Velders (1995), Patra et al. (2011)	monthly	climatology
Cl	Sherwen et al. (2016)	monthly	2005 repeating
Soil	Murguia-Flores et al. (2018)	monthly	1996-2009 (2010-2012 is 2009 repeating)

Table 2.1: The emission and loss fields input to MOZART, along with their temporal resolution and the years covered by the fields.

The different emission and loss fields have been scaled to the mean magnitude, source δ^{13}C-CH_4, and loss kinetic isotope effects (KIEs) in the literature. The literature ranges of the loss KIEs are examined in Section 2.2.4, the source magnitudes were taken from Saunois et al. (2016), and the source δ^{13}C-CH_4 were taken from Schwietzke et al. (2016). These ranges are further discussed in Section 2.3. Using these mean values produces a methane simulation like that shown in Figure 2.2.1. This

simulation has a greater methane mole fraction trend than the observations, as well as a more negative δ^{13}C-CH_4, and an upward δ^{13}C-CH_4 trend rather than the downward trend seen in the observations. The trends from the emissions inventories are what causes the growth in methane around 2007, which are shown in Figure 2.2.2. This figure shows that fossil fuels, agriculture, waste, and wetlands all contribute to the positive trend in methane mole fraction in this simulation.

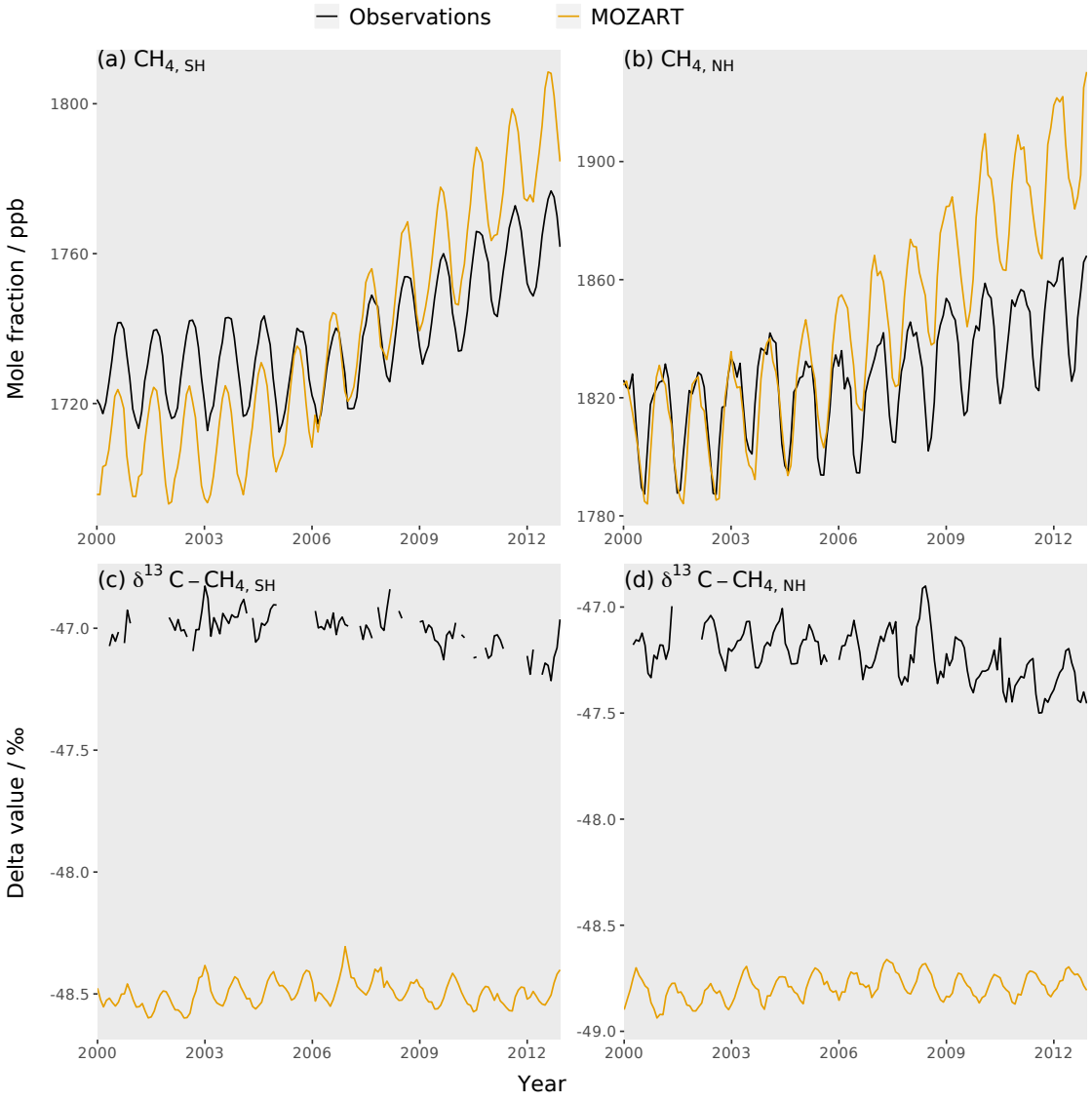

Figure 2.2.1: The MOZART methane simulation using mean parameter values (orange line) compared to the observations (black line) for four measures: (a) the southern hemisphere methane mole fraction, (b) the northern hemisphere methane mole fraction, (c) the southern hemisphere δ^{13}C-CH_4, and (d) the northern hemisphere δ^{13}C-CH_4.

Figure 2.2.2: The difference between the annual mean of the unscaled emission inventories and their temporal mean over 1996-2012. Negative values indicate a year with below average emissions for that source, positive values indicate a year with above average emissions.

2.2.2 The implications of offline chemistry

In this work, the model's chemistry is offline, meaning that the hydroxyl radical concentration in the model is fixed by the input fields and is not reduced by reaction with methane. This means that the positive feedback (described in Sections 1.1 and 1.2.2) where increasing methane emissions decrease the OH concentration, allowing the methane mole fraction to rise further, is not present. Nguyen et al. (2020) showed that using offline chemistry can affect the results of methane inverse modelling studies, and if the methane mole fraction continues to increase, the feedback will become increasingly important for a given perturbation (e.g. Prather (1996)). Whilst offline chemistry does remove the important non-linearity between methane emissions and methane mole fraction, the non-linearity remains for the loss processes.

This non-linearity can be demonstrated by consideration of the methane mole fraction in steady state. Consider the rate of change of the methane mole fraction with respect to time (t) in a simple one box-model, which only includes the emission of methane (E) and the loss of methane by reaction with OH:

$$\frac{d[\mathrm{CH_4}]}{dt} = E - k[\mathrm{CH_4}][\mathrm{OH}], \tag{2.1}$$

where k is the rate constant for the reaction of OH and CH_4, and $[CH_4]$ and [OH] are the methane mole fraction and the concentration of OH respectively. The steady state mole fraction of CH_4 ($[CH_4]_{ss}$) can be derived from Equation 2.1 as:

$$[\mathrm{CH_4}]_{ss} = \frac{E}{k[\mathrm{OH}]}. \tag{2.2}$$

Therefore, if [OH] is held constant, then $[CH_4]_{ss}$ is proportional to E, and so changes in emissions result in a linear change to $[CH_4]_{ss}$. However, if E is held constant, then $[CH_4]_{ss}$ is proportional to $1/[\mathrm{OH}]$, and so changes in [OH] result in a non-linear change to $[CH_4]_{ss}$. This non-linearity is shown to be significant over a large range of [OH] in Figure 2.2.3. Similar non-linearities are present for the loss of methane by Cl and in the stratosphere, though the smaller magnitude of these losses means that these non-linearities are less important than OH to the methane budget.

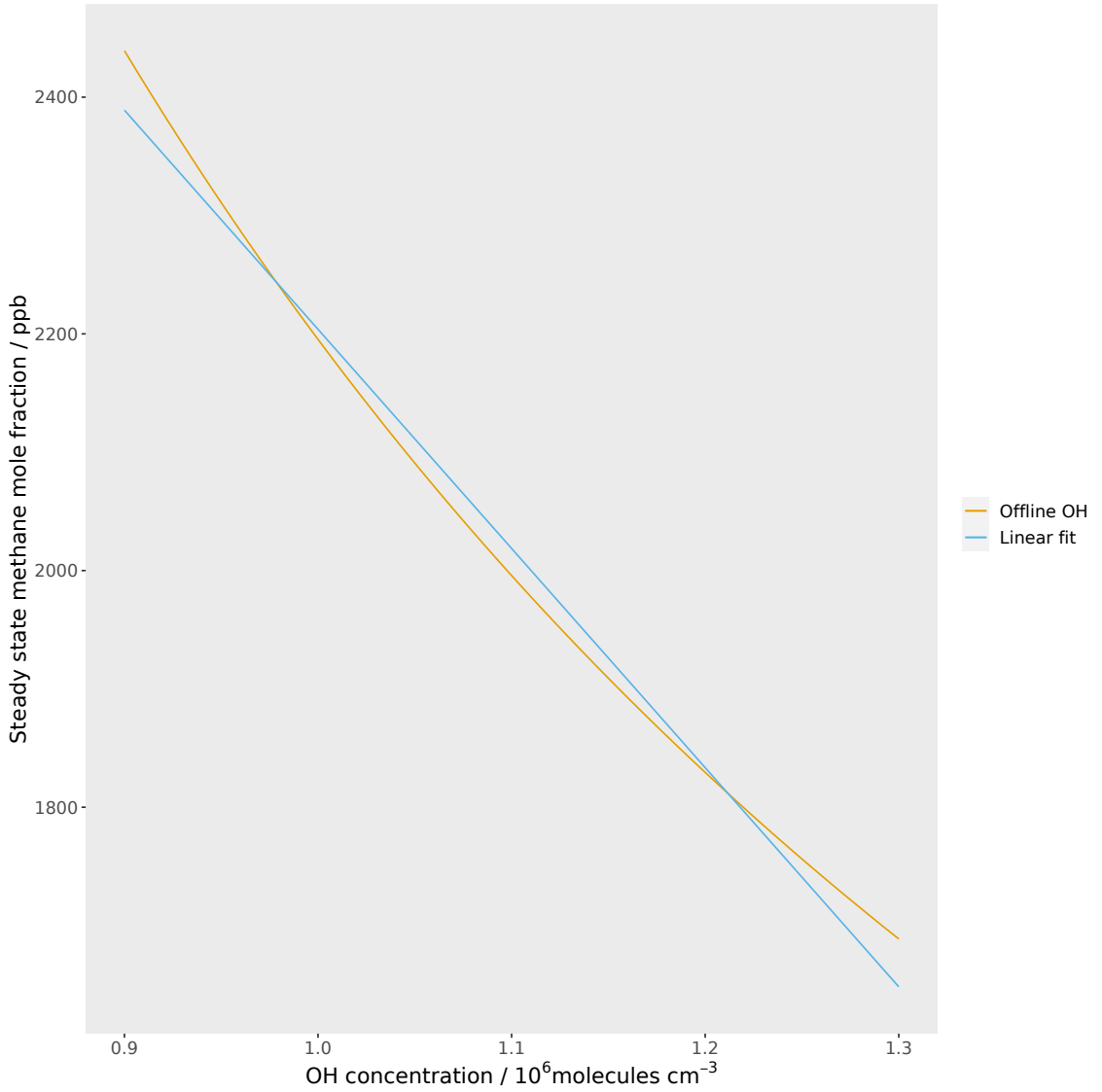

Figure 2.2.3: An illustration of how offline chemistry still leads to non-linearity in the methane system: the OH concentration has a non-linear affect on the steady state methane mole fraction. This is a plot of Equation 2.2, where the value of E used is 700 Tg yr^{-1} and k is 3.7×10^{-15} molecules cm^{-3} s^{-1}.

2.2.3 Creation of a freshwater emissions map

The importance of the freshwater source, which, as far as we are aware, has not been included as a separate methane source in any previous atmospheric methane modelling studies, was introduced in Section 1.2.1. It is a large source, albeit highly uncertain (Wik, Thornton, Bastviken, Uhlbäck & Crill 2016), with a potentially large climate feedback, so, we propose that it is critical to include it in atmospheric

modelling studies. In this thesis, the first simple global freshwater map for atmospheric methane modelling is constructed.

Method

The production of a global freshwater map of methane flux is limited by the resolution and accuracy of freshwater maps. Two of the main global freshwater databases are the Global Lakes and Wetlands Database (GLWD) (Lehner & Döll 2004) and GLObal WAter BOdies (GLOWABO) (Verpoorter et al. 2014), which are compiled in different ways. GLWD is compiled from maps, registers, and archives (which can be incomplete, especially for small water bodies) whereas GLOWABO is compiled using high resolution satellite data and image recognition. GLOWABO covers all lakes greater than 0.002 km^2, whereas GLWD only covers permanent, open freshwater bodies larger than 0.1 km^2. It is currently not possible to detect the smallest ponds (less than 0.001 km^2) globally with maps or satellites, and their emissions can be confused with wetlands (Thornton et al. 2016). However, they are thought to be a significant proportion of emissions (Holgerson & Raymond 2016).

In this work, the Global Lakes and Wetlands Database (GLWD) (Lehner & Döll 2004) was used to create a global map of the locations of freshwater bodies. This map was chosen over GLOWABO because it includes lakes, reservoirs, and rivers reported as separate categories, each of which releases different amounts of methane (Wik, Varner, Anthony, MacIntyre & Bastviken 2016, Guérin et al. 2006, Yang 2019), although this separation was not used in this version of the methane emission map due to the small number of samples of these freshwater categories (Bastviken et al. 2011, Stanley et al. 2016). Methane emissions from each water body was weighted according to its percentage of the freshwater area, to give a global total of 120 $Tg\,yr^{-1}$ (Saunois et al. 2016). The Earth was split into three latitude bands: tropical (less than 30 ° N and S), mid-latitudes (30-50 ° N and S), and high-latitudes (more than 50 ° N and S), and weighted according to Saunois et al. (2016) to account for the different climatic conditions: 49 % of global freshwater methane emissions are tropical, 33 % in the mid-latitudes, and 18 % in the high-latitudes. The emissions

map is time-invariant due to a lack of observational evidence of seasonal variability caused by the highly variable nature of freshwater emissions and the limited amount of continuous measurements (Natchimuthu et al. 2016, Wik, Thornton, Bastviken, Uhlbäck & Crill 2016). However, freshwater emissions have a strong temperature dependency and so it is possible that freshwater emissions have a seasonal cycle with a large amplitude (Wilkinson et al. 2015). The freshwater emissions distribution used in this work can be seen in Figure 2.2.4.

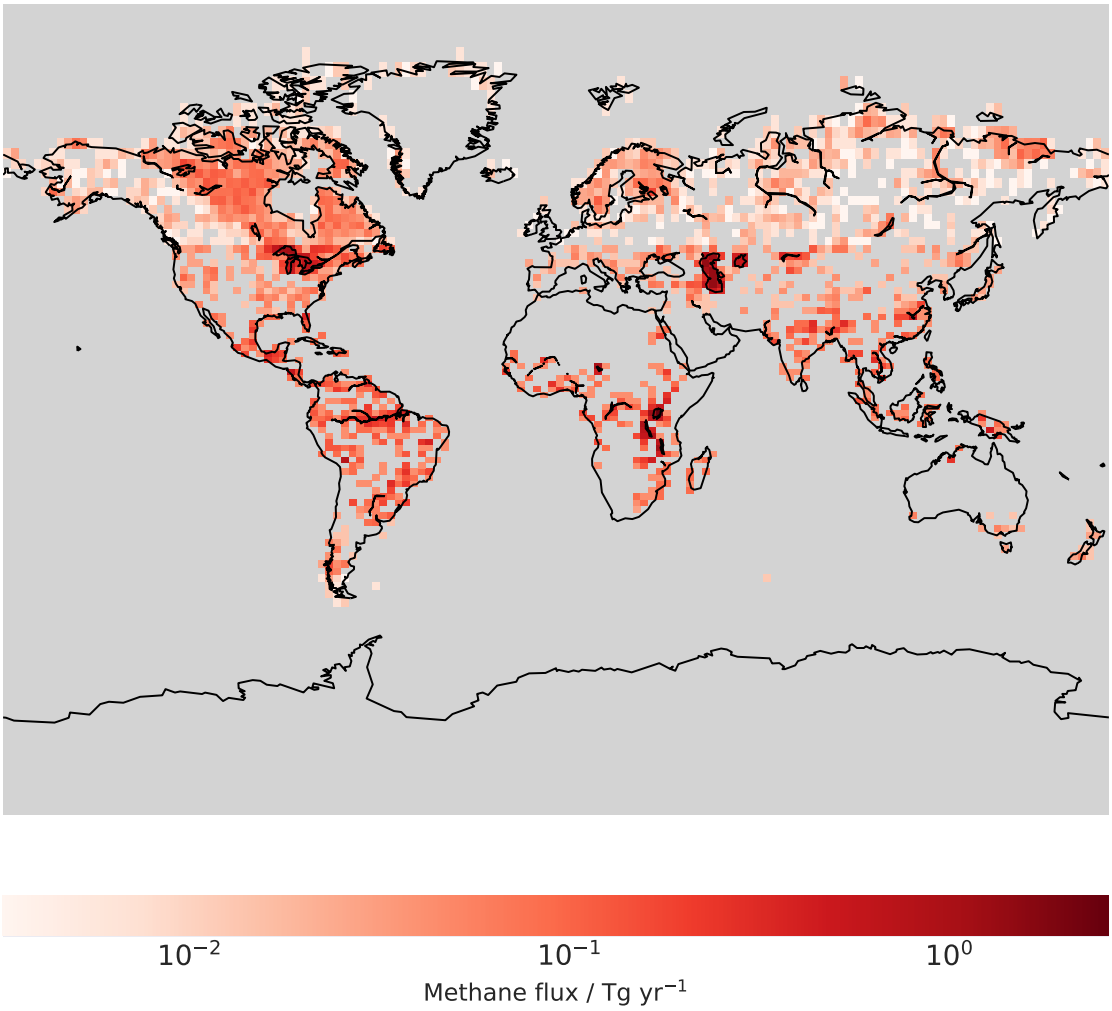

Figure 2.2.4: The global distribution of freshwater methane emissions used in this work. Total methane emissions are 120 Tg yr^{-1} (Saunois et al. 2016), which is distributed according to the freshwater area in three latitude bands as described in the text.

The importance of the inclusion of a freshwater map

Fresh water is an important source because of its potentially large magnitude and uncertainty (Figure 1.2.1). By not considering this source, top-down studies may erroneously attribute freshwater emissions to another source. In Figure 2.2.5, the spatial correlation in the annual mean for the year 2000 between the different sources are shown. There are only weak correlations, so the sources are largely spatially independent. In Figure 2.2.6, the freshwater source spatial distribution is compared to the source it is expected to be most similar to: wetlands (termites also look similar in Figure 2.2.5 but they are a minor source that is generally not optimised in top-down studies). Wetland emissions are dominant in the Amazon, South East Asia, and some parts of Africa, whereas freshwater emissions are dominant in the northern latitudes, particularly in North America and other parts of Africa. Therefore, fresh water is a spatially distinct source and should be included in modelling to accurately reproduce methane observations. This spatial distribution difference of the sources is also true for hemispheric emissions as seen in Figure 2.2.7, where the percentage of methane emissions in the northern hemisphere for all the sources used in this thesis are shown. Fresh water is significantly more northern hemisphere dominant than wetlands. If the freshwater source is not included, it is likely that changes in the freshwater emissions would be attributed to a combination of sources, because no single source is very similarly spatially distributed. For example, a combination of wetlands (for its somewhat similar spatial distribution), and agriculture and fossil fuels (which have larger northern hemisphere emissions than wetlands, like fresh water).

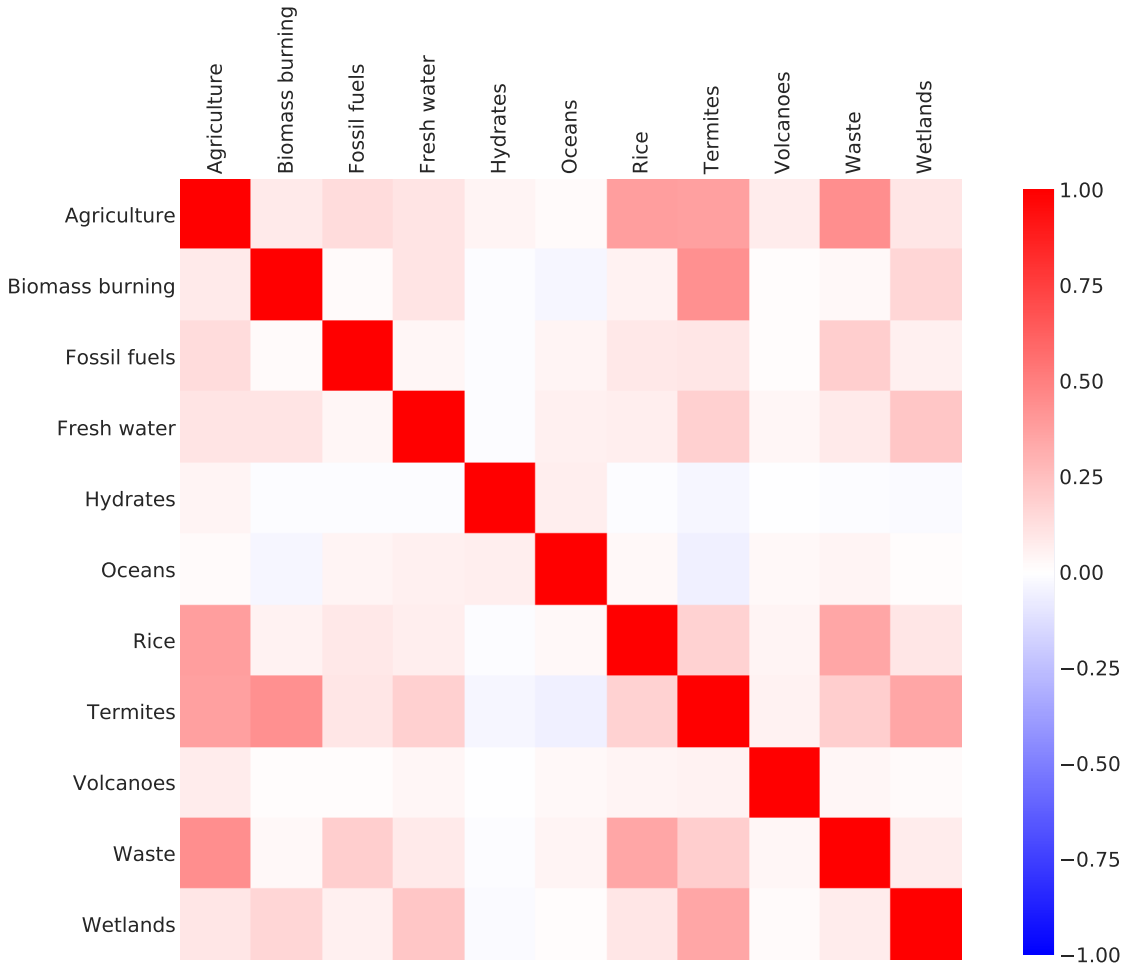

Figure 2.2.5: A spatial correlation matrix between the methane source maps for the annual mean of 2000. All grid cells with no emissions (over oceans for example) have been excluded. The maps have been normalised so that the largest value in a MOZART grid cell for a source is one, and the lowest is zero.

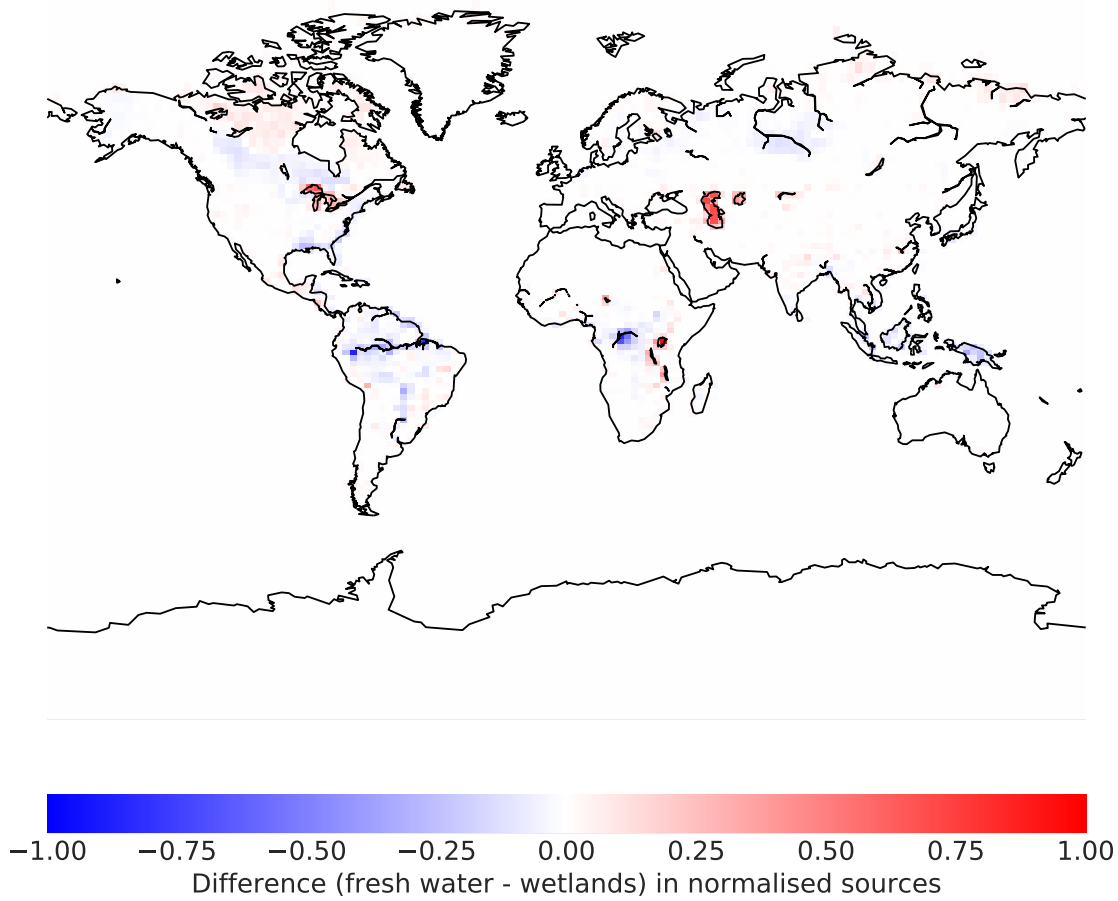

Figure 2.2.6: The difference in the distribution of the freshwater and wetland sources for the annual mean of 2000. All grid cells with no emissions (over oceans for example) have been excluded. The source maps have been normalised so that the largest value in a MOZART grid cell for a source is one, and the lowest is zero.

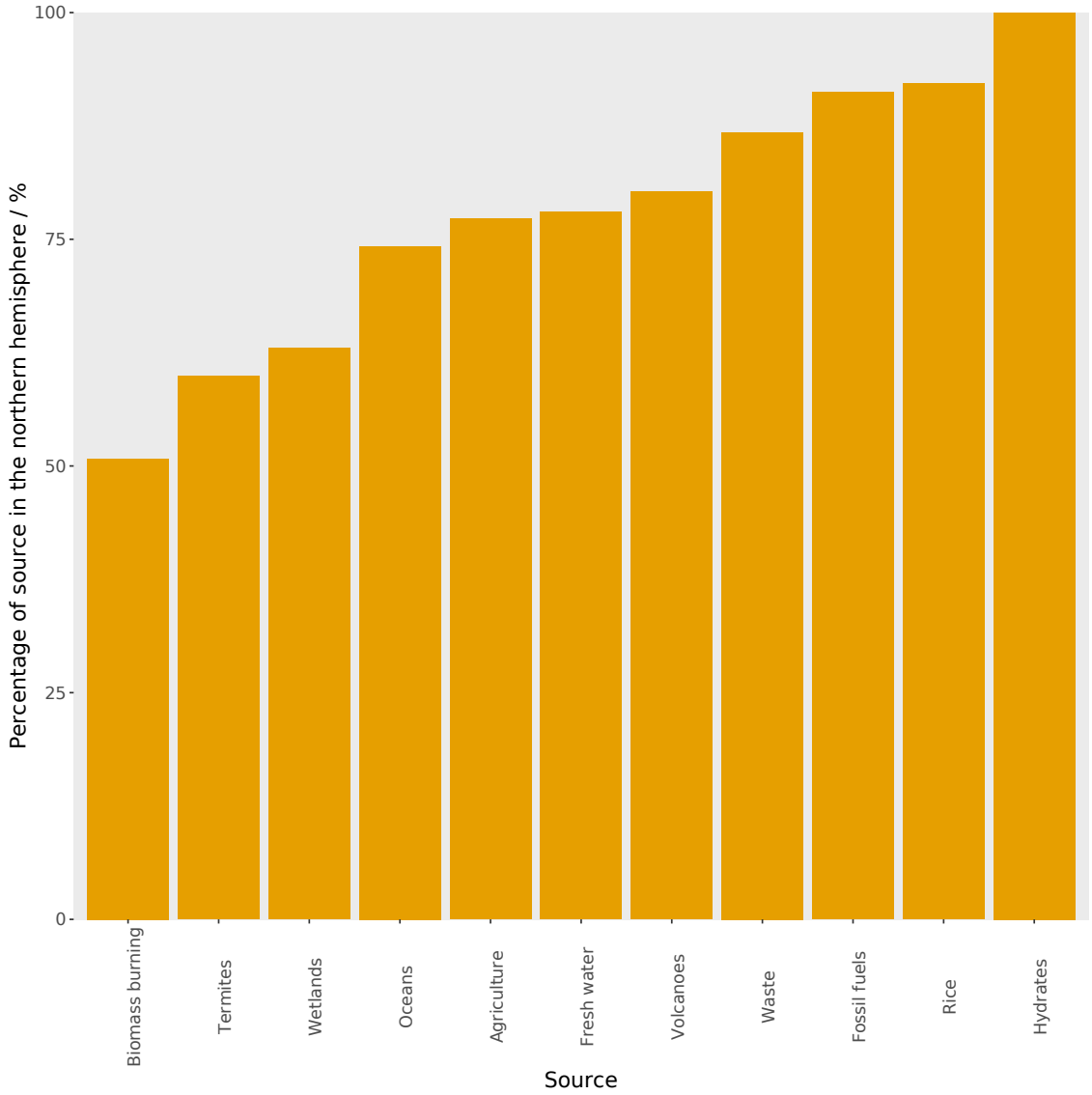

Figure 2.2.7: The percentage of methane emissions in the northern hemisphere for the 2000 annual mean of each emissions map used in this thesis.

This freshwater emissions map is very simple and there are several improvements that could be made. For example, one improvement would be more careful consideration of which water bodies to include, as the Caspian Sea is saline so could be removed or reduced (e.g. Liu & Boone (1991), Pattnaik et al. (2000)). Additionally, the relationship between freshwater body area and methane emissions could be made into power law (e.g. Bastviken et al. (2004), Wik, Varner, Anthony, MacIntyre & Bastviken (2016)); and freshwater body depth is also a key variable in predicting methane emissions from ebullition that is not considered here (Bastviken et al. 2004). The power law relationship means that the many small water bodies missing

from GLWD are important (Holgerson & Raymond 2016), and ideally lakes from the higher resolution GLObal WAter BOdies database (GLOWABO) (Verpoorter et al. 2014) should be included. Lake depths for the largest lakes are also included in Kourzeneva et al. (2012), so there is potential to combine all available databases. Variables such as temperature and water body type would also ideally be included (e.g. Yvon-Durocher et al. (2014), Wik, Varner, Anthony, MacIntyre & Bastviken (2016)). The suggested improvements to this map are not required for this work, as the map is latitude-band weighted, so the hemispheric distribution is consistent with bottom-up estimates and will not majorly impact the results.

2.2.4 Loss kinetic isotope effect range

The literature values for the kinetic isotope effects (KIEs) for the reactions of methane were collated, and a range of possible values chosen.

Reaction of CH_4 and OH

There are a range of recorded literature KIEs for this reaction which are listed in Table 2.2. The KIE is calculated by comparing the reaction rate of $^{12}CH_4$ and OH with that for $^{13}CH_4$ and OH. Rust & Stevens (1980) had experimental difficulties and recorded a wide range of values (1.0003 to 1.0078) and Davidson et al. (1987) was superseded by Cantrell et al. (1990). This leaves only Saueressig et al. (2001) and Cantrell et al. (1990). In this work, the two standard deviation range is taken as $^{13C}KIE_{OH}$=1.0035-1.0043, from the accepted value of Saueressig et al. (2001).

	Reference	KIE	Two standard deviations
Experimental	Saueressig et al. (2001)	1.0039	0.0004
	Cantrell et al. (1990)	1.0054	0.0009
	Davidson et al. (1987)	1.010	0.007
	Rust & Stevens (1980)	1.0036	0.0026
Theoretical	Gupta et al. (1997)	1.010	
	Melissas & Truhlar (1993)	1.005	
	Lasaga & Gibbs (1991)	1.007	

Table 2.2: Literature values reported for the kinetic isotope effect of CH_4 and OH.

Reaction of CH_4 and $O(^1D)$

There are very few studies of the KIE of this reaction: Saueressig et al. (2001) report a value of 1.013, whereas Davidson et al. (1987) report a value of 1.001 from a single experiment. In this work, we take only the accepted value from Saueressig et al. (2001), which the authors report as having a negligible uncertainty.

Reaction of CH_4 and Cl

Table 2.3 shows the range of values for $^{13C}\text{KIE}_{Cl}$ in the literature. There is good agreement between the experimental literature values. Taking the full range of the two standard deviation uncertainty of these three studies, gives a range of 1.062 to 1.068.

	Reference	KIE	Two standard deviations
Experimental	Tyler et al. (2000)	1.0621	0.0001
	Crowley et al. (1999)	1.066	0.002
	Saueressig et al. (1995)	1.066	0.002
Theoretical	Roberto-Neto et al. (1998)	1.06	
	Gupta et al. (1997)	1.034	
	Tanaka et al. (1997)	1.026	

Table 2.3: Literature values reported for the kinetic isotope effect of CH_4 and Cl.

Loss of CH_4 by soil

The literature values of ${}^{13C}\text{KIE}_{soil}$ are reported in Table 2.4. There is good agreement between these values and so the full range of values are used, giving a two standard deviation range of 1.016 to 1.026.

Reference	KIE	Two standard deviations
Snover & Quay (2000)	1.0173	0.0020
	1.0181	0.0008
Reeburgh et al. (1997)	1.023	
	1.026	
Tyler et al. (1994)	1.022	0.008
King et al. (1989)	1.026	
	1.016	

Table 2.4: Literature values reported for the kinetic isotope effect of CH_4 and soil.

KIEs for MOZART

The literature KIEs are transformed into values for the corresponding MOZART loss files, given in Table 2.5. This means converting ${}^{13C}\text{KIE}_{O(1D)}$ and ${}^{13C}\text{KIE}_{Cl}$ to a stratospheric value. An estimated 20 to 35 % of the stratospheric loss of methane is due to Cl, and 25 % due to $O(^1D)$ (Saunois et al. 2016) (the rest is OH which

is covered by the OH loss field). These fractions were used to create a weighted average fractionation value of 1.0402 in Table 2.5.

	Minimum	Maximum	Default value
$^{13C}\text{KIE}_{OH}$	1.0037	1.0041	1.0039
$^{13C}\text{KIE}_{STRAT}$	1.035	1.044	1.0402
$^{13C}\text{KIE}_{Cl}$	1.0635	1.0665	1.065
$^{13C}\text{KIE}_{soil}$	1.0185	1.0235	1.021

Table 2.5: The full range of KIEs used in the MOZART simulations. The default value is used in all training simulations and the range represents one standard deviation which is the range considered in Section 2.5.2.

2.3 Creation of the CTM training dataset

To create a training dataset for the Gaussian process emulators, a set of methane simulations with different model inputs must be created. Which model inputs to vary and their uncertainty ranges are discussed in Section 2.3.1, and Section 2.3.2 discusses how to sample from these ranges to efficiently cover the parameter space.

2.3.1 The chemical transport model inputs and their ranges

Six groups of input parameters are explored: source magnitudes, source δ^{13}C-CH_4, loss magnitudes, loss kinetic isotope effects, temporal trend variation for the largest emissions or losses, and initial conditions. In order to simplify the analysis, the smallest terms in the methane budget, termites, hydrates, and oceans, were held constant and not included in the emulator development. This cut-off is somewhat arbitrary, and is shown in Fig. 1.2.1. The uncertainty associated with fixing these terms is explored and will be discussed in Section 2.5.2. Once the input parameters have been chosen, it is important to find their possible ranges so that a set of model simulations covering these values can be created. This is achieved by scaling the

magnitude, δ^{13}C-CH_4, and trends of the fields in Table 2.1. These simulations form the training dataset for Gaussian process emulation.

The minimum and maximum values for the sources are shown at the top of Table 2.6. Where only one value is given, the parameter was held constant at this value. The range of possible magnitudes of emissions were based on the range of literature values as summarised in Saunois et al. (2016), and the range of possible δ^{13}C-CH_4 values were taken as the three standard deviation range from Schwietzke et al. (2016).

The minimum and maximum values for the losses are given in the middle of Table 2.6. Reaction rate constants of methane with OH, Cl, and O(^{1}D) are fixed at the values given by Burkholder et al. (2015). Whilst there is some uncertainty in these rate constants, the influence of the uncertainties in these terms will be similar to that of their respective loss magnitudes (but not identical as the rate constant uncertainty is temperature dependent). The loss fields are scaled with the magnitudes taken from the range of literature values (Saunois et al. 2016), and kinetic isotope effects (KIEs) were decided by averaging literature values (King et al. 1989, Tyler et al. 1994, Saueressig et al. 1995, Reeburgh et al. 1997, Crowley et al. 1999, Snover & Quay 2000, Tyler et al. 2000, Saueressig et al. 2001) detailed in Section 2.2.4.

For the five largest methane emissions or losses (OH, wetlands, fresh water, agriculture, and fossil fuels), we allowed the overall inventory or process model trend to vary by ±20 %. This set of parameters was included to explore the influence of possible uncertainties in the trends. This parameter range is somewhat arbitrary, but was designed to be inclusive of the majority of plausible values. For example, the OH concentration trend for this period has been proposed to be nearing +10 % (Stevenson et al. 2020); -8 ± 11 % or -11 ± 11 % for 2004 to 2014 using either AGAGE or NOAA data, respectively (Rigby et al. 2017); or around 7 % for 2003 to 2016 (Turner et al. 2017). Given the large uncertainties derived in these studies, a trend range of ±20 % is plausible.

The final set of parameters control the spin-up (Section 1.5.3). To emulate the

response of the methane mole fraction and δ^{13}C-CH_4 to the spin-up, three factors were varied during this period: the total source magnitude, the total source δ^{13}C-CH_4, and an imbalance in magnitude between sources and losses. The ranges of these parameters are given at the bottom of Table 2.6.

Source	Magnitude / $Tg\,yr^{-1}$	Delta value / ‰	Trend / %
Wetlands	136, 250	-63.3, -59.7	-20, 20
Fresh water	54, 198	-64.6, -59.8	-20, 20
Agriculture	86, 122	-75.2, -58.4	-20, 20
Rice	21, 40	-66.0, -58.2	
Waste	46, 69	-57.7, -53.5	
Fossil fuel (includes biofuel)	104, 162	-45.1, -38.4	-20, 20
Biomass burning	14, 29	-27.9, -16.5	
Volcanoes	27, 62	-46.1, -41.9	
Termites	9.6	-65.0	
Hydrates	0	-62.2	
Oceans	16	-57.9	
Loss	Magnitude / $Tg\,yr^{-1}$	KIE	Trend / %
OH	414, 730	1.0039	-20, 20
Stratosphere	6, 55	1.0397	
Cl	12, 41	1.0640	
Soil	8, 52	1.0215	
Spin-up	Magnitude / $Tg\,yr^{-1}$	Delta value / ‰	
Spin-up source	495, 976	-59.5, -52.4	
Spin-up source minus loss	10, 65		

Table 2.6: A table of the ranges of the 28 input parameters to MOZART that were varied in the training simulations, hence also in the emulators, and in the analysis. Where one value is given, the value is held constant for all simulations. Where two values are given, they are the lower and upper limit, respectively.

2.3.2 Sampling the parameter space

The generation of the training dataset is the most time consuming step as running the CTM takes far longer than building or running the emulators. Therefore, it is

important to create the smallest number of simulations possible to train accurate emulators. This can be achieved through the choice of input parameter combinations for the simulations. Each parameter described in Table 2.6 is assigned a uniform probability distribution over the range given. In order to sample from the distributions in a way that effectively covers the parameter space, a maximin Latin hypercube was used (McKay et al. 1979, Morris & Mitchell 1995). In Latin hypercube sampling, the parameter space is divided into equally probable subsections according to the number of samples. The samples are then distributed into these subsections so that there is a sample in each subsection for each parameter. For example, a two-dimensional parameter space with uniform parameter distributions would be divided into a square grid with 100 cells if 10 samples were to be taken. A random sampling pattern is then chosen so that there is a sample in each of the 10 rows and columns. The maximin version of the Latin hypercube means that the samples are additionally arranged so that the minimum distance between samples is maximised. In this work, a training dataset of 270 MOZART simulations was created and used to build a Gaussian process to emulate MOZART in Chapter 3.

2.4 Comparison of the model output and observations

In order to constrain the methane budget, the training dataset will be used to train a Gaussian process emulator in Chapter 3, the outputs from which will be compared to observations in Chapter 5. Therefore, in Sections 2.4.1 and 2.4.2 the observations and the MOZART simulation outputs are processed similarly so that they are comparable. Then in Section 2.4.4, the MOZART outputs and the observations are compared to check that the observations lie within the envelope of the MOZART training simulations.

2.4.1 Processing of observations

The global network of atmospheric monitoring stations, described in Section 1.4, is used to derive an observational time series of hemispheric monthly means. The baseline methane mole fraction and δ^{13}C-CH_4 at each station in the National Oceanic and Atmospheric Administration (NOAA) carbon cycle greenhouse gases network (Dlugokencky et al. 2017, White et al. 2018) was plotted against the methane mole fraction and δ^{13}C-CH_4 from the corresponding MOZART grid cell. MOZART grid cells that exhibited substantial above-baseline variability (likely an artefact of the coarse resolution) were discarded. Measurement stations that do not have approximately continuous records for the period of interest (more than 9 out of 13 years) were also discarded. The remaining 26 stations measuring methane mole fraction and 10 stations measuring δ^{13}C-CH_4 are listed in Table 2.7, and their locations are shown in Fig. 2.4.1.

Station	Latitude / ° N	Longitude / ° W	Altitude / masl	Mole fraction	δ^{13}C-CH_4
Alert, Nunavut, Canada	82	297	195	x	x
Terceira Island, Azores, Portugal	39	333	24	x	
Baring Head Station, New Zealand	-41	175	90	x	
Tudor Hill, Bermuda, UK	32	295	60	x	
Cold Bay, Alaska, USA	55	197	32	x	
Cape Grim, Tasmania, Australia	-41	145	164	x	x
Crozet Island, France	-46	52	202	x	
Easter Island, Chile	-27	251	57	x	
Mariana Islands, Guam	13	145	7	x	
Halley Station, Antarctica, UK	-76	334	35	x	
Storhofdi, Vestmannaeyjar, Iceland	63	340	127	x	
Izana, Tenerife, Canary Islands	28	344	2378	x	
Key Biscayne, Florida, USA	26	280	6	x	
Cape Kumukahi, Hawaii, USA	20	205	9	x	x
Mace Head, County Galway, Ireland	53	350	26	x	x
Sand Island, Midway, USA	28	183	8	x	
Mauna Loa, Hawaii, USA	20	204	3419	x	x
Niwot Ridge, Colorado, USA	40	254	3526		x
Palmer Station, Antarctica, USA	-65	296	15	x	
Ragged Point, Barbados	13	301	20	x	
Shemya Island, Alaska, USA	53	174	28	x	
Tutuila, American Samoa	-14	189	53	x	x
South Pole, Antarctica, USA	-90	335	2817	x	x
Summit, Greenland	73	322	3215	x	
Syowa Station, Antarctica, Japan	-70	40	16	x	
Tae-ahn Peninsula, Republic of Korea	37	126	21		x
Ushuaia, Argentina	-55	292	32	x	
Mt. Waliguan, People's Republic of China	36	101	3815		x
Ny-Alesund, Svalbard, Norway	79	12	479	x	

Table 2.7: All NOAA stations used in this work, along with their latitude, longitude, altitude, and the type of measurement. The units of the altitude data is metres above sea level (masl).

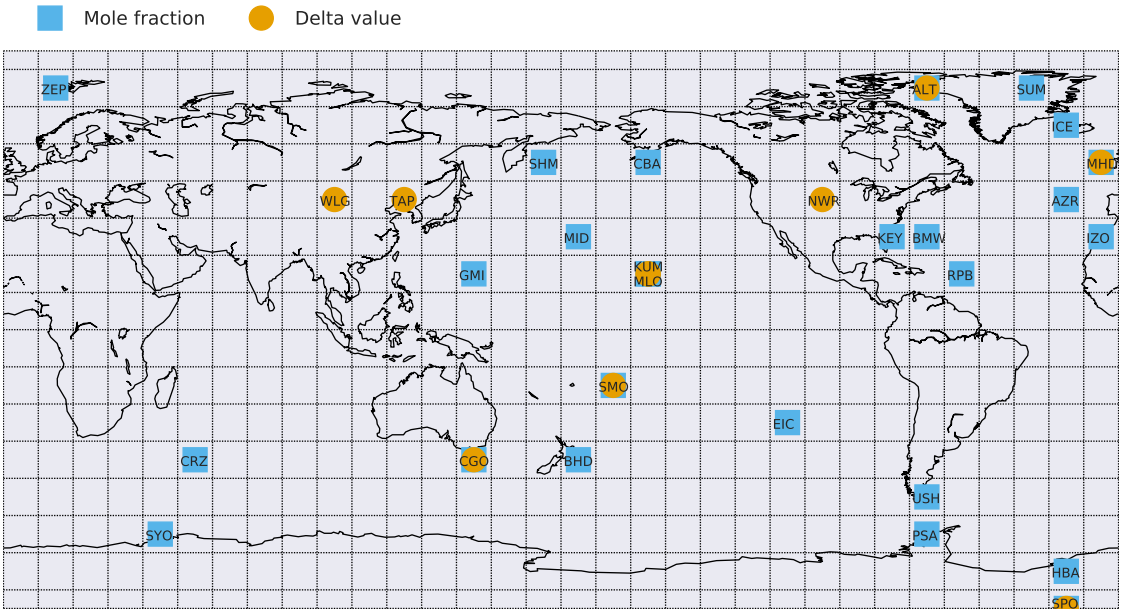

Figure 2.4.1: Map of the measurement stations used in this thesis in their corresponding MOZART grid cells (the dashed two-dimensional grid), as well as the measurement type: blue squares are methane mole fraction and orange circles are δ^{13}C-CH_4 stations. Each station is labelled with the NOAA three character station code. Where two stations appear in an identical two-dimensional grid cell, the stations are located at different altitudes, so are in different MOZART grid cells in three dimensions.

Each station is matched to a MOZART grid cell based on its mean latitude, longitude, and altitude. Some of the stations that have been matched to the sixth model level should have been at a higher model level, but since only the lowest six model levels were saved for analysis (Section 2.2.1), this was not possible. The sixth model level is at an altitude of about 1 km, so the six sites above this in Table 2.7 are affected. A monthly mean was calculated for each station. To calculate the hemispheric mean, the station monthly means are split into the northern and southern hemispheres. They are then combined using a sine latitude-weighted mean, producing a hemispheric monthly mean time series. Where monthly means were available for fewer than three stations, that month was omitted from the analysis to avoid bias due to sub-sampling of the intra-hemispheric gradient.

2.4.2 Processing of MOZART outputs

The MOZART outputs will be used to create emulators in Chapter 3, so they have to be processed slightly differently to the observations. The time correlation structure of the emulators (Section 3.2.2) means that the methane output in all the MOZART grid cells must contribute to the hemispheric monthly mean, regardless of whether there are measurements for that month or not. Therefore, every 6-hourly MOZART output in the grid cells matching the chosen stations is included in the hemispheric mean. Otherwise, the MOZART output values are calculated like the observations in Section 2.4.1, except that median monthly values are calculated (instead of the mean for the observations). This is because the observations are filtered to remove pollution events, and so any high methane mole fraction events in MOZART should also be removed.

2.4.3 Combining outputs to summary outputs

In this thesis, the model outputs and observations are sometimes combined as a global mean, inter-hemispheric difference, and trend of the methane mole fraction and δ^{13}C-CH_4. The global mean is defined as the temporal mean of the mean of the northern and southern hemispheres, the inter-hemispheric difference is the temporal mean of the northern hemisphere minus the southern hemisphere, and the trend is the global mean in December 2012 minus December 2000.

2.4.4 Comparison of MOZART training dataset and observations

Here, the training dataset is compared to observations, in order to check that the observations lie within the envelope of the MOZART output ensemble. The temporal mean of the global mean, the temporal mean of the inter-hemispheric difference, and trend (Section 2.4.3) for the methane mole fraction and δ^{13}C-CH_4 outputs for each MOZART simulation are presented in Figure 2.4.2. In this figure, the distribution of the MOZART simulations (orange bars) can be compared to the black line of the

observations, which shows overlap between MOZART and the observations by all measures. However, the observed inter-hemispheric differences lie close to the edge of the distribution, which is likely because of the fixed spatial distributions of the sources and sinks (further discussed in Section 5.6).

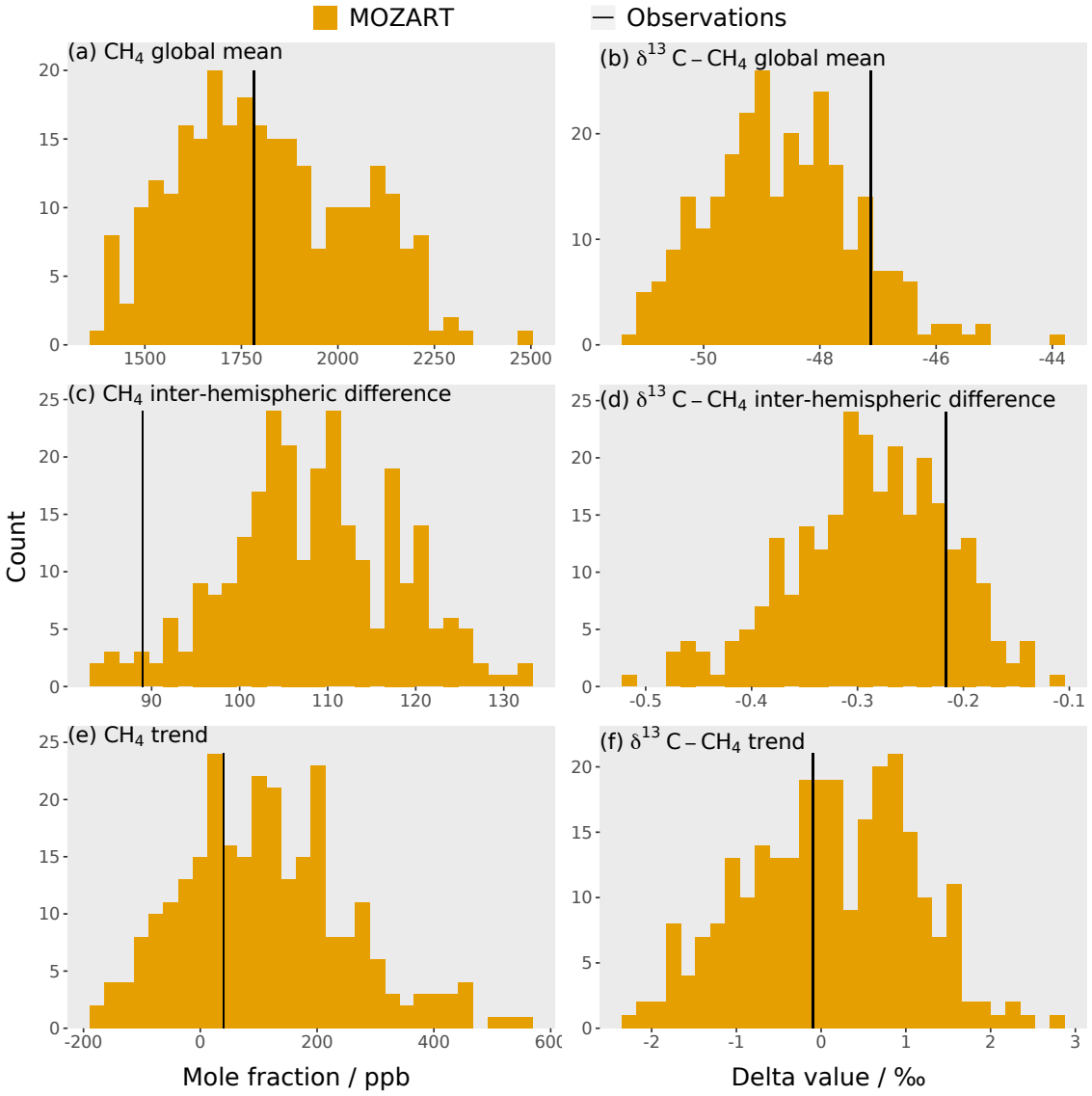

Figure 2.4.2: Histograms of the 270 three-dimensional CTM training simulations for six outputs: (a) methane mole fraction global mean, (b) δ^{13}C-CH_4 global mean, (c) methane mole fraction inter-hemispheric difference, (d) δ^{13}C-CH_4 inter-hemispheric difference, (e) methane mole fraction trend, and (f) δ^{13}C-CH_4 trend. The black lines are the corresponding values for the observations.

2.5 Calculation of uncertainties

There are often multiple ways to quantify uncertainties from complex systems, making uncertainties difficult to calculate. In this section, two uncertainties are calculated: the model-measurement discrepancy error (Section 2.5.1) and the MOZART invariant parameter error (Section 2.5.2). The model-measurement discrepancy error is caused by the uncertainty in the observations and the model's limitations in reproducing the observations. The MOZART invariant parameter error is a systematic error caused by some model inputs being held constant in the training dataset. These uncertainties must be quantified to know how close the MOZART outputs need to be to the observations to be considered statistically consistent.

2.5.1 The model-measurement discrepancy error

The model-measurement discrepancy error is calculated by considering four elements that would cause the model output to differ from the observations. To account for these differences, the standard deviation in 10 000 samples from the uncertainty distributions of these four elements is calculated. The two MOZART simulations in the training dataset closest to the methane mole fraction and δ^{13}C-CH_4 observations were chosen as base simulations, around which these uncertainties are examined.

For each of the 10 000 samples, a random value drawn from a normal distribution with a mean of zero and a standard deviation of the maximum measurement error reported by NOAA (Section 1.4) is added to every 6-hourly output value in each grid cell of the base simulations. The standard deviation is 2.4 ppb and 0.182 ‰ for the methane mole fraction and δ^{13}C-CH_4 respectively, although the δ^{13}C-CH_4 measurement error does briefly go up to 3.2 ‰ in the NOAA dataset, a value of 0.182 ‰ was chosen as this is more representative of the usual maximum measurement error.

The model is limited in its ability to reproduce the observations due to its coarse resolution, this is accounted for by a representation error. To calculate the horizontal representation error, a higher spatial resolution (1.89 °N × 2.50 °W) MOZART

simulation with the mean emissions and losses in the training dataset was used. The range of outputs over the high resolution grid cells within a low resolution grid cell was calculated. The vertical representation error is calculated by taking the range of the output in each low resolution grid cell and the grid cell above and below. For the bottom model level, only the grid cell and the one above is included in the range, and for the sixth model level, the range is calculated for the grid cell and the one below and then doubled, because the seventh model level has been removed (Section 2.2.1). For each of the 10 000 samples, a random value drawn from a uniform distribution between minus half the range and plus half the range is added to every 6-hourly output value in each grid cell of the base simulations for both the horizontal and vertical representation error.

The model hemispheric time series includes all grid cells with measurement stations in every month, regardless of whether there are observations for that station in that month (Section 2.4.2). Therefore, the effect of including different stations in the hemispheric mean is explored by bootstrap resampling. For each of the 10 000 samples, 26 stations for the methane mole fraction and 10 stations for the δ^{13}C-CH_4 (the number of stations included in this study (Section 2.4)) were chosen by sampling the stations with replacement. This resampling method means that a station can be included in a sample anywhere between zero and 26 times for the methane mole fraction, and zero to ten times for the δ^{13}C-CH_4.

The model hemispheric monthly time series includes all 6-hourly outputs at a station (Section 2.4.2), but the observation hemispheric time series includes only approximately four samples in a monthly mean. To include the effect of having differently timed samples in the monthly output, four random time points are chosen to contribute to each station's monthly value in each of the 10 000 samples.

The hemispheric time series is then calculated as in Section 2.4.2, and the standard deviation in the 10 000 samples of the hemispheric time series is used as the model-measurement discrepancy error. This error has a median value of 4.6 ppb and 0.097 ‰ in the southern hemisphere, and 8.6 ppb and 0.078 ‰ in the northern hemisphere.

2.5.2 The MOZART invariant parameter error

In this work, one part of the error in the CTM was calculated: the invariant parameter error. To the best of our knowledge, this term has never been included in atmospheric methane studies before. However, consistent with other studies, it should be noted that other model errors, which are very challenging to calculate, are not included such as model transport uncertainties and higher-order "invariant parameter errors" (e.g. erroneous trends or spatial distributions). Therefore, the estimate presented here is likely to be smaller than the full CTM error. As in Vernon et al. (2010), the uncertainty due to the parameters that were held constant in the training dataset (given in Table 2.8), was calculated. These parameters are the magnitudes and δ^{13}C-CH_4 signatures of the three smallest sources, and the isotopic fractionation of the losses. The kinetic isotope effects of the loss reactions are changed by varying the $^{13}CH_4$ reaction rate and the $^{12}CH_4$ reaction rate held constant. The reaction rate constant (k) can be represented by the Arrhenius equation:

$$k(T) = A \times \exp(-E/RT), \tag{2.3}$$

where T is the temperature, A is the pre-exponential A factor, E is the activation energy, and R is the universal gas constant. It is the A factor that is varied in this thesis in order to change the $^{13}CH_4$ reaction rate, and the ranges used for Cl and the stratospheric loss are given in Table 2.8. The ranges given in Table 2.8 cover one standard deviation, rather than the entire literature range in Table 2.6, so that the MOZART invariant parameter error only accounts for the most plausible range. The OH reaction A factor was also considered, but MOZART only allows the rate constant to be input with two decimal places, and the OH and $^{13}CH_4$ A factor is constant when given to two decimal places over the range of KIEs explored (Table 2.5).

The invariant parameter error was calculated with a set of 90 MOZART simulations with only the invariant parameters varying over a uniform distribution of their ranges in a maximin Latin hypercube design. The covariance matrix of the output of this

set of simulations is used as a measure of the MOZART invariant parameter error. The standard deviation of the diagonal of this inactive parameter matrix can be seen in the following section, and has a mean value of 10 ppb and 0.1 ‰ for the methane mole fraction and δ^{13}C-CH_4, respectively, which is large compared to the observed trends of 40 ppb and -0.1 ‰ over the time period in this work. This error is highly correlated between the two hemispheres and throughout the time series (Section 5.2.2), which will have a significant impact on what can be inferred from the model about the methane budget.

Term	Magnitude / $\mathrm{Tg\,yr^{-1}}$	Delta value / ‰	$^{13}CH_4$ A factor
Termites	5.0, 14.2	-66.7, -63.3	
Hydrates	0.0, 0.9	-63.0, -61.4	
Oceans	8.3, 23.7	-51.7, -44.1	
Soil		-24.0, -19.0	
Chlorine			6.66, 6.68 $\times$ 10^{-12} $\mathrm{cm^3\,molecule^{-1}\,s^{-1}}$
Stratosphere			0.958, 0.966 $\mathrm{s^{-1}}$

Table 2.8: The ranges of possible values of the inactive parameters (from the literature as in Section 2.3.1), where the first number is the minimum and the second number is the maximum.

The MOZART global mean methane mole fraction and δ^{13}C-CH_4 output, averaged over the time series, for each of the 90 simulations is plotted against each of the input parameters in a separate panel in Figures 2.5.1 and 2.5.2, demonstrating the effect of varying the nine invariant parameters on the MOZART outputs. If there is a strong correlation between a parameter's values and the MOZART output, then this parameter dominates the variability caused by varying all the parameter values. For the methane mole fraction, the ocean source magnitude dominates, whereas there is no dominant parameter in the δ^{13}C-CH_4.

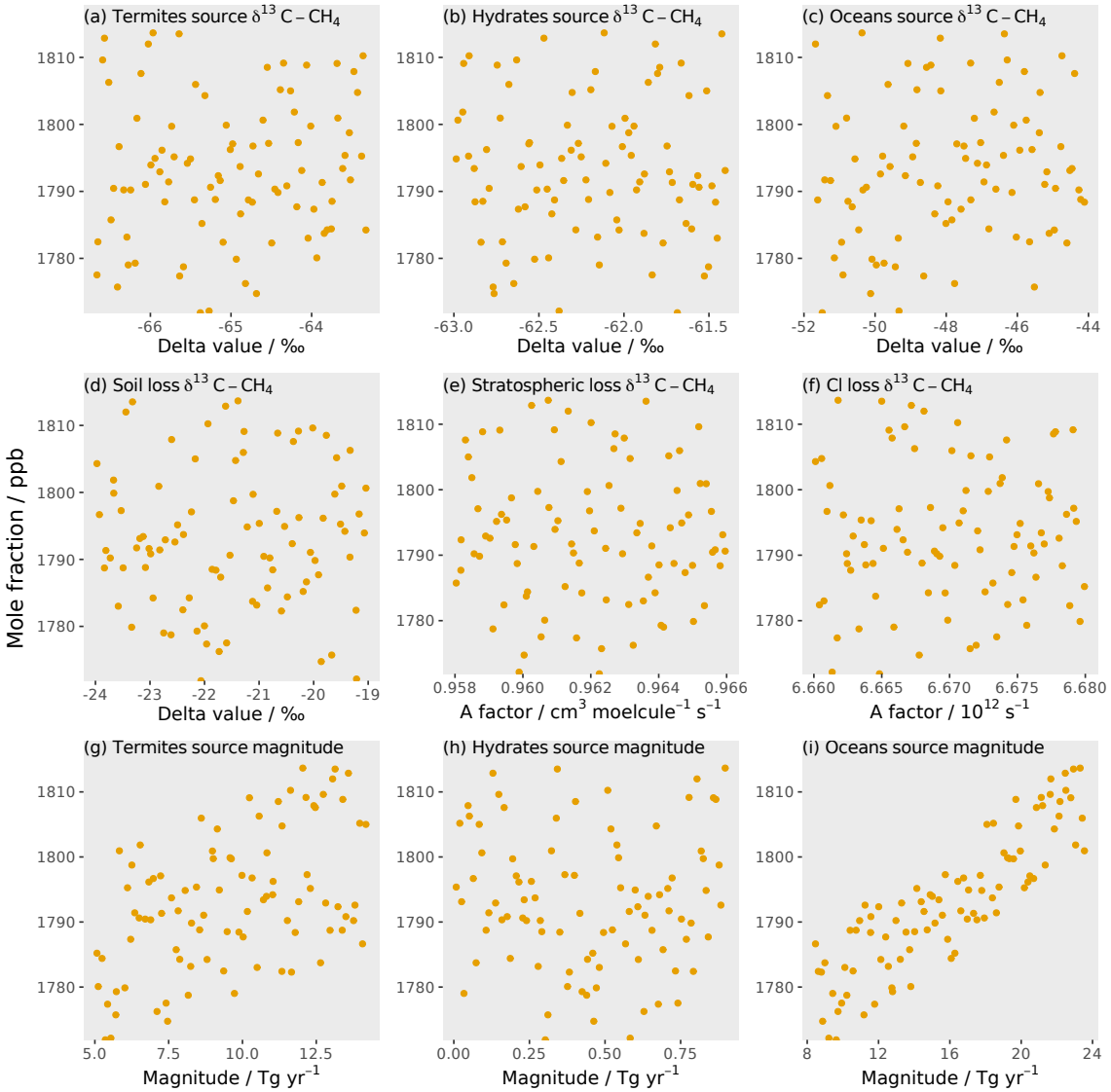

Figure 2.5.1: The same MOZART global mean methane mole fraction output, averaged over the time series, for each of the 90 simulations plotted against each of the input parameter's values in a separate panel.

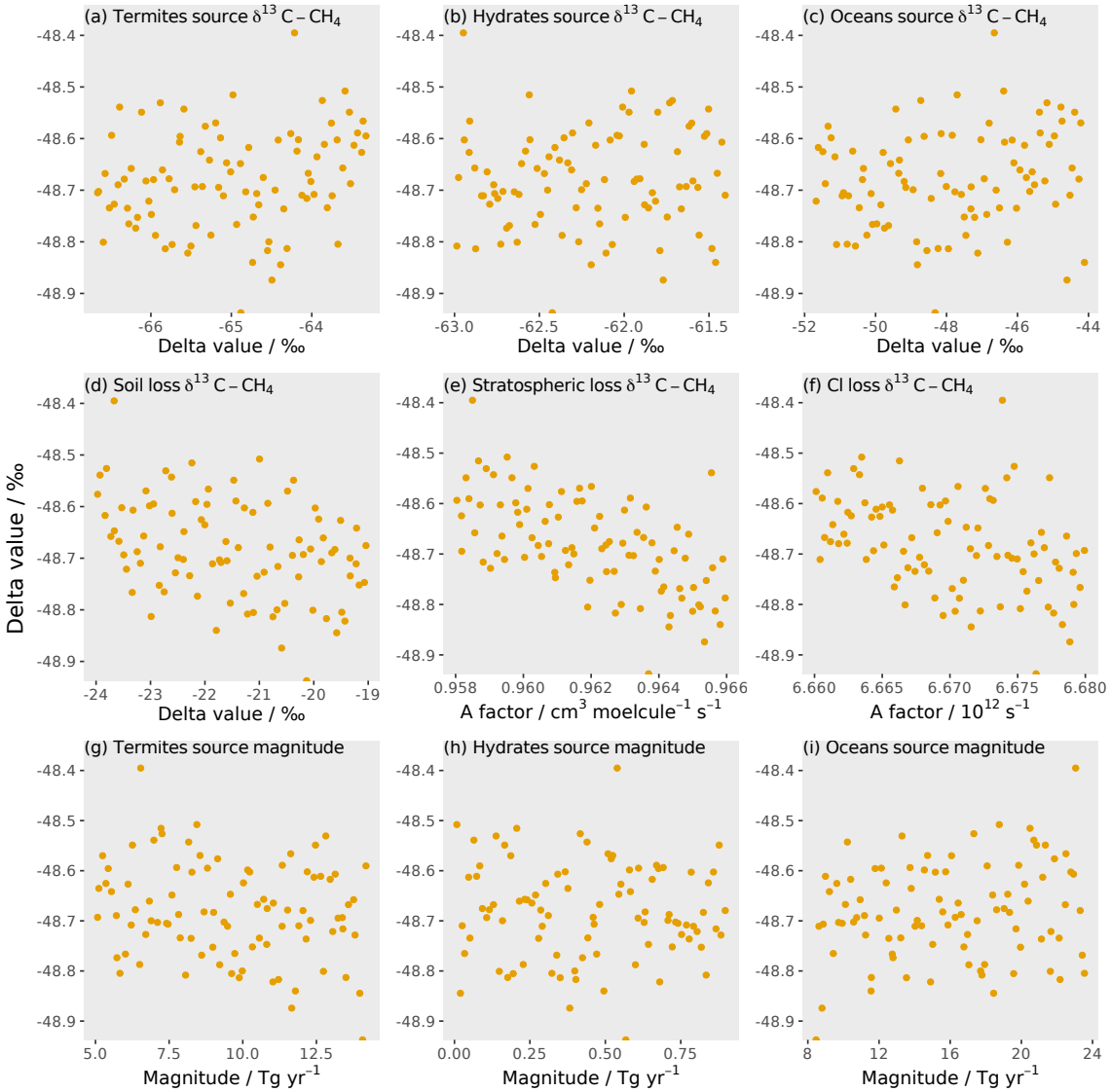

Figure 2.5.2: The same MOZART global mean δ^{13}C-CH_4 output, averaged over the time series, for each of the 90 simulations plotted against each of the input parameter's in a separate panel.

2.5.3 Comparison of the model-measurement discrepancy and MOZART invariant parameter errors

In this section, the model-measurement discrepancy and MOZART invariant parameter errors are compared and combined. In Figure 2.5.3, the two errors are plotted, as well as the total error, calculated by adding the two errors in quadrature. The model-measurement discrepancy and MOZART invariant parameter errors are of similar magnitude, so the MOZART invariant parameter error that, to the best

of our knowledge, has been left out of previous top-down studies has a significant impact on the total error. Therefore, previous studies, that have held uncertain parameters constant, significantly underestimate the total error. This is especially critical given this uncertainty is highly correlated (Section 5.2.2), and has a large impact on what we can learn about the methane budget, as will be seen in Chapter 5.

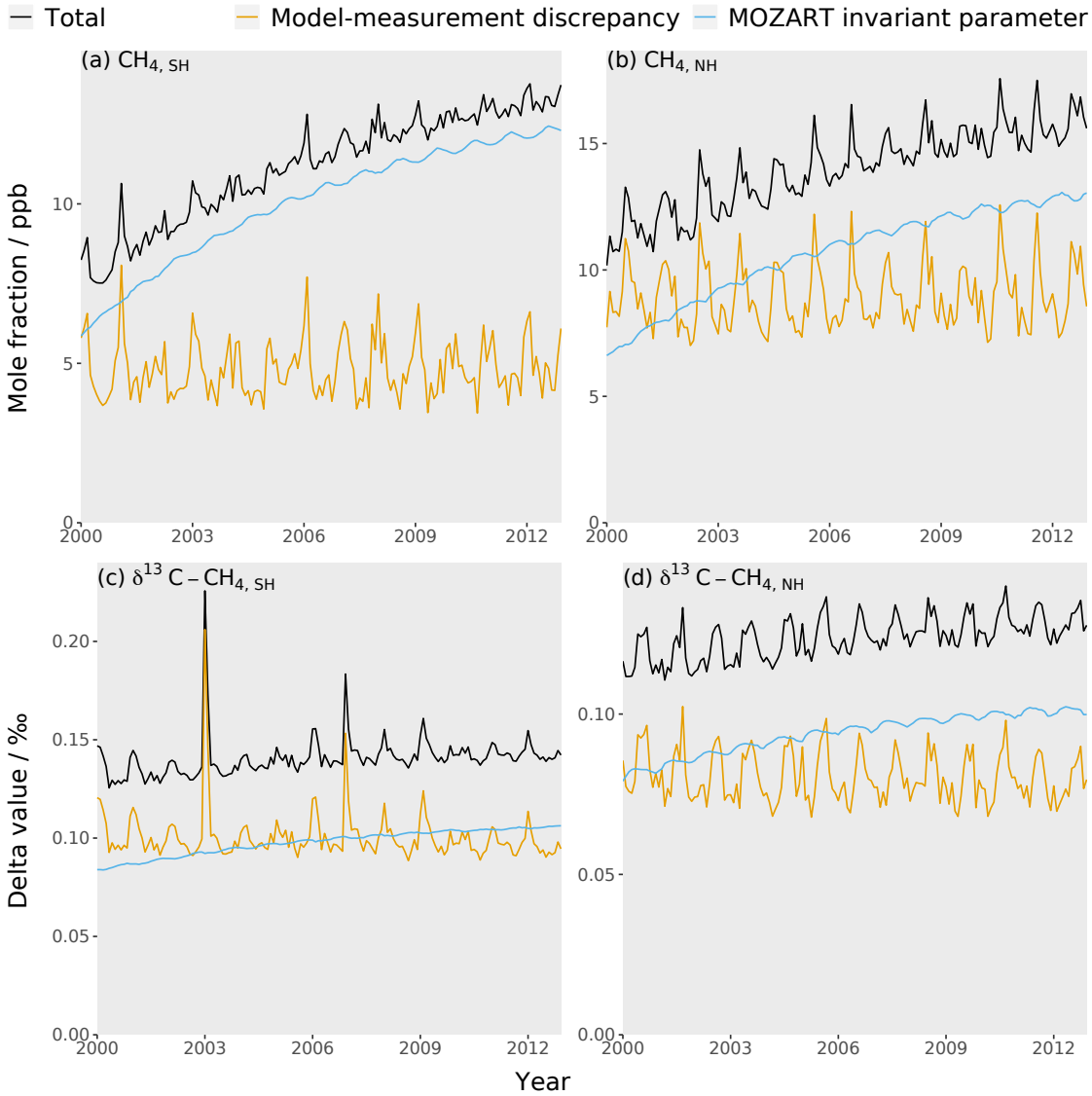

Figure 2.5.3: Comparison of the model-measurement discrepancy error (orange line), MOZART invariant parameter error (blue line), and their combined error (black line): (a) the southern hemisphere methane mole fraction, (b) the northern hemisphere methane mole fraction, (c) the southern hemisphere δ^{13}C-CH_4, and (d) the northern hemisphere δ^{13}C-CH_4.

2.6 Summary

This chapter began with the development of a global three-dimensional CTM simulation of the methane mole fraction and δ^{13}C-CH_4. This simulation includes emissions from 11 sources and four loss processes, with magnitudes and temporal trends taken from bottom-up estimates.

The simulation is the first in atmospheric methane modelling, as far as we are aware, to include freshwater emissions as an independent source. In order to do this, the first global map for freshwater methane emissions for use in atmospheric methane modelling studies was created. Whilst this map is simple, it is an important first step in including this large, though uncertain, methane source in top-down methane studies. The map was shown to be spatially distinct from the other methane source maps, including the source that would be expected to be most similar: wetlands. The inclusion of an independent freshwater map will prevent any possible changes in the freshwater source being attributed to other sources in top-down studies.

Running a methane simulation in MOZART takes 4.5 hours (run on 12 cores of a 2.4 GHz Intel E5-2680 v4 Broadwell CPU), so only a limited number of methane simulations can be produced. This means that to fully utilise this model to constrain the methane budget, it must be sped up. In this thesis, emulators will be created for the MOZART model in order to do this. Therefore, in this chapter, a training dataset of MOZART simulations was created in order to train a Gaussian process emulator. This training dataset is composed of 270 MOZART simulations with 28 input parameters that describe the sources and sinks of methane.

The training dataset was compared to observations, in order to check that the observations lie within the envelope of the MOZART output ensemble. The observations do lie in the range of the MOZART training data, although the inter-hemispheric differences, for both the methane mole fraction and δ^{13}C-CH_4, were towards the edges of the MOZART distributions. Perhaps this suggests that more input parameters that control the inter-hemispheric difference should be included, as all the spatial distributions of the sources and sinks were fixed.

To find the emulator outputs that match observations, it is necessary to quantify the errors in the system. This will be made up of the model-measurement discrepancy error, the MOZART invariant parameter error, and the emulator error added in quadrature. In this chapter, the model-measurement discrepancy error and the MOZART invariant parameter error were calculated and compared. The two error types are of similar magnitude, so the invariant parameter error makes a significant contribution to the total error. The invariant parameter error was calculated by varying some of the parameters that were held constant in the MOZART simulations. As far as we are aware, this error has been left out of previous top-down methane modelling studies. This error is particularly important as it is highly correlated in time and between hemispheres. This means that many previous studies are likely to have underestimated their uncertainty, which will affect what can be learnt about the methane budget.

Chapter 3

Training a Gaussian process to emulate an atmospheric chemical transport model

3.1 Introduction

In the previous chapter, 270 MOZART simulations were created. This is a large number of simulations for a three-dimensional global chemical transport model (CTM) because these models are so computationally expensive. However, for many types of analysis, such as Bayesian optimisation of parameters (Section 1.6), similar numbers of simulations are required to find a local minimum in the cost function (Equation 1.13). Alternatively, a thorough exploration of the posterior probability distribution requires $\sim 10^6$ runs (e.g. Rigby et al. (2017), Turner et al. (2017)), which is unfeasible for a three-dimensional CTM. Therefore, in previous studies a two-dimensional box model, or linear sensitivities or adjoint code for a three-dimensional CTM has been used instead (Section 1.7). The run-time of these two-dimensional box models are less than a second, but they generally have limited spatial resolution and lack interannual variability in transport. Whereas the sensitivities of three-dimensional CTMs make it challenging to fully explore the parameter space and thoroughly quantify the uncertainty in the optimised parameters.

In this work, a new method is developed to maintain the benefits of a three-dimensional CTM whilst allowing rapid computation of the influence of model inputs on the outputs, without assuming linearity and with an estimate of the uncertainty, using a Gaussian process emulator. An emulator is a statistical approximation to a more complex model, often using a Gaussian process (Section 1.8). In this chapter, Gaussian process emulators for MOZART are built and validated. This reduced the time to evaluate MOZART outputs for a given set of inputs from 4.5 hours (run on 12 cores of a 2.4 GHz Intel E5-2680 v4 Broadwell CPU in a supercomputer) to 40 ms (run on a single core of a 1.6 GHz Intel Core i5 CPU in a laptop), provided a training set such as that outlined in Chapter 2 is available.

In this chapter, the methods for training the Gaussian process are first summarised in Section 3.2, and the emulators are then validated in Section 3.3. The number of simulations required to build an accurate Gaussian process is examined in Section 3.4, and the advantages of a Gaussian process over multiple linear regression (which is commonly used in atmospheric methane studies) is examined in Section 3.5.

3.2 Method

3.2.1 Gaussian process setup

Four independent Gaussian process emulators were built using the MOZART training dataset: the inputs are the sources and sinks of methane described in Section 2.3.1, and the output is the MOZART monthly averages described in Section 2.4.2 (the southern hemisphere methane mole fraction, the northern hemisphere methane mole fraction, the southern hemisphere δ^{13}C-CH_4, and the northern hemisphere δ^{13}C-CH_4).

The Gaussian process is defined by its mean and covariance functions (Section 1.8.2). The mean function of the Gaussian process used here is a multiple linear regression as the system is close to linear (Section 1.8.2 and Section 3.5), but this linear mean function does not mean that the relationship between inputs and outputs in the

Gaussian process is linear. The MOZART output is a time series, making the covariance function more complex than the basic method outlined in Section 1.8.2. The modifications to the covariance function are outlined in Section 3.2.2.

3.2.2 Gaussian process emulation for time series outputs

Each MOZART output is a time series of 156 monthly averages (12 months for each of 13 years). These outputs are highly correlated, and to minimise information loss this correlation is accounted for in the emulator covariance. This covariance matrix ($\mathbf{\Sigma}$) is composed using the Kronecker product of a temporal covariance matrix ($\mathbf{\Sigma}_t$) and a parameter covariance matrix ($\mathbf{\Sigma}_x$):

$$\mathbf{\Sigma} = \mathbf{\Sigma}_t \otimes \mathbf{\Sigma}_x. \tag{3.1}$$

The temporal covariance is assumed to be a first order autoregressive model (AR(1)) (its value depends only on the previous month). The temporal covariance matrix ($\mathbf{\Sigma}_t$) is (n, n) dimensional, where n is the number of time points, and its $(i, j)^{\text{th}}$ element is:

$$\zeta_{t,ij} = \frac{\rho^{|t_i - t_j|}}{1 - \rho^2} \tag{3.2}$$

where ρ is the autocorrelation parameter and t is the month. This means that the output of all MOZART grid cells has to be included in every month of the hemispheric average, regardless of there being observations in this grid cell or not. This is because the simple time correlation structure does not account for the possibility of changing spatial distributions effecting the output of different months.

The parameter covariance is assumed to be a squared exponential. The parameter covariance matrix ($\mathbf{\Sigma}_x$) is (p, p) dimensional, where p is the number of training simulations, and its $(i, j)^{\text{th}}$ element is

$$\zeta_{x,ij} = \sigma_f^2 \exp\left(- \sum_{k=1}^{m} \frac{(x_{k,i} - x_{k,j})^2}{l_k^2} \right), \tag{3.3}$$

where σ_f^2 is the maximum covariance, x_k is the value of the k^{th} input parameter, and l_k is the length scale correlation for the k^{th} input parameter.

The emulator parameters, denoted as $\boldsymbol{\phi}$, (ρ in Equation 3.2, σ_f and l_k in Equation 3.3) are optimised by maximising the log-likelihood function:

$$ln(L(\boldsymbol{y}|\boldsymbol{\phi})) = -\frac{1}{2}(\boldsymbol{y} - m(\boldsymbol{x}))^T \boldsymbol{\Sigma}^{-1}(\boldsymbol{y} - m(\boldsymbol{x})) - \frac{1}{2}ln(|\boldsymbol{\Sigma}|) - \frac{np}{2}ln(2\pi), \tag{3.4}$$

where $\boldsymbol{y}$ is the training dataset outputs and $m(\boldsymbol{x})$ is the emulator mean function. This log-likelihood function is optimised with a bounds constrained quasi-Newton method (Gay 1990) started from 28 different random points, and the maximum likelihood emulator of the 28 is chosen. This setup uses an adaptation of the R package, Stilt (Olson et al. 2018).

3.3 Validation of the emulators

It is important to check that the emulators are an accurate approximation of the relationship between the inputs and outputs of MOZART before they are used. A validation dataset (an independent maximin Latin hypercube design of 90 MOZART simulations) is used to confirm this, because it contains inputs and known MOZART outputs that the emulator was not trained on. The emulator predictions for the validation dataset inputs can be compared to the MOZART output, and these differences reveal how accurate the approximation is. There are several graphical comparison methods presented in this section.

3.3.1 Relation of emulator errors and inputs

Differences between the emulator and MOZART should not correlate with the input values. If correlations are present, this indicates either some emulator parameters are not optimal or non-stationarity (Bastos & O'Hagan 2009). In Figures 3.3.1, 3.3.2, 3.3.3, and 3.3.4, the difference between the temporal mean of the prediction for the

four emulators and the MOZART value are plotted against each input parameter value. No correlation is shown for any emulator with any input parameter.

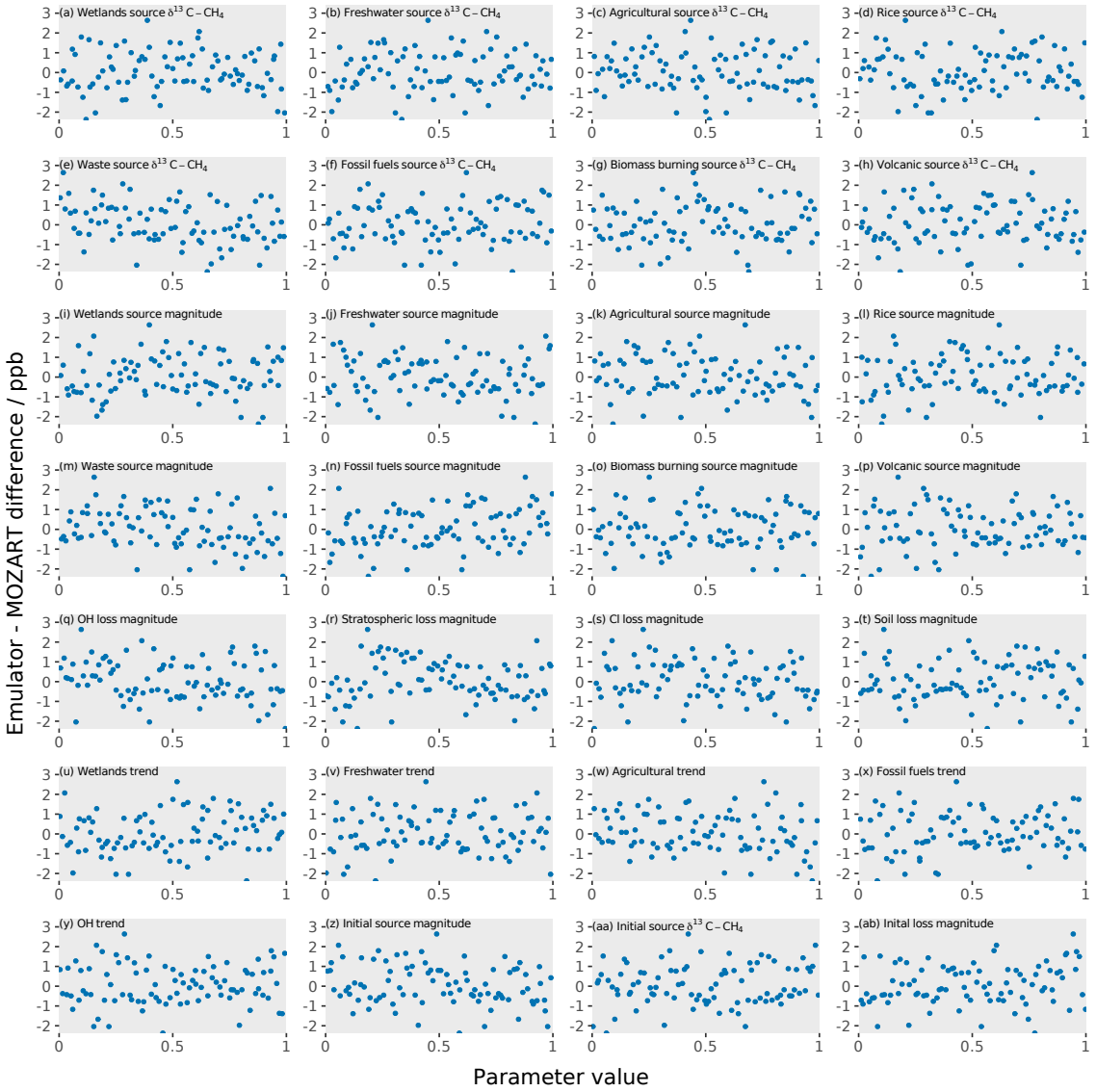

Figure 3.3.1: The difference between the southern hemisphere methane mole fraction emulator and the true value in the MOZART model for each of the 90 validation simulations, averaged over the time series, is plotted against the value of each input parameter in a separate panel.

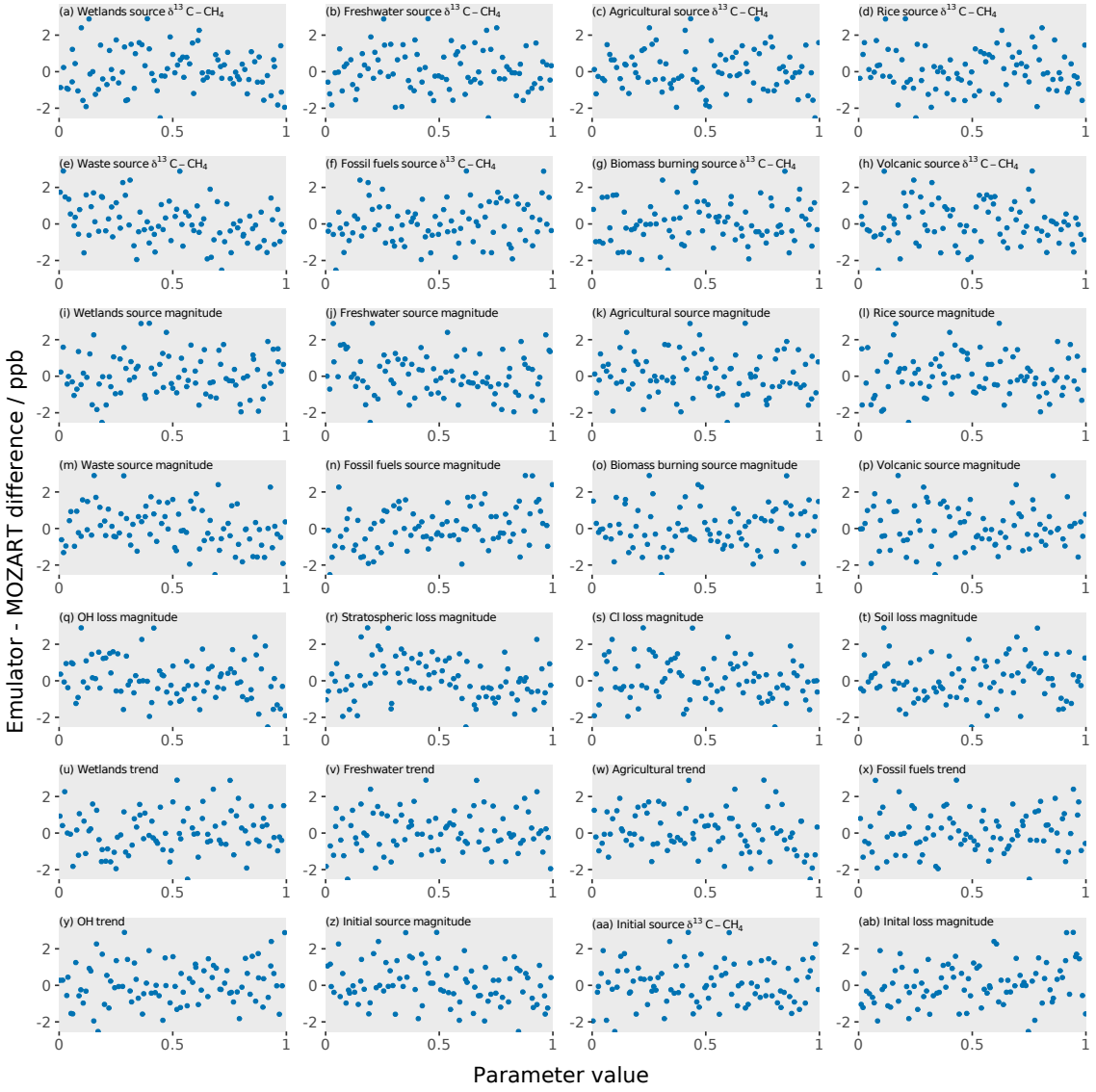

Figure 3.3.2: The difference between the northern hemisphere methane mole fraction emulator and the true value in the MOZART model for each of the 90 validation simulations, averaged over the time series, is plotted against the value of each input parameter in a separate panel.

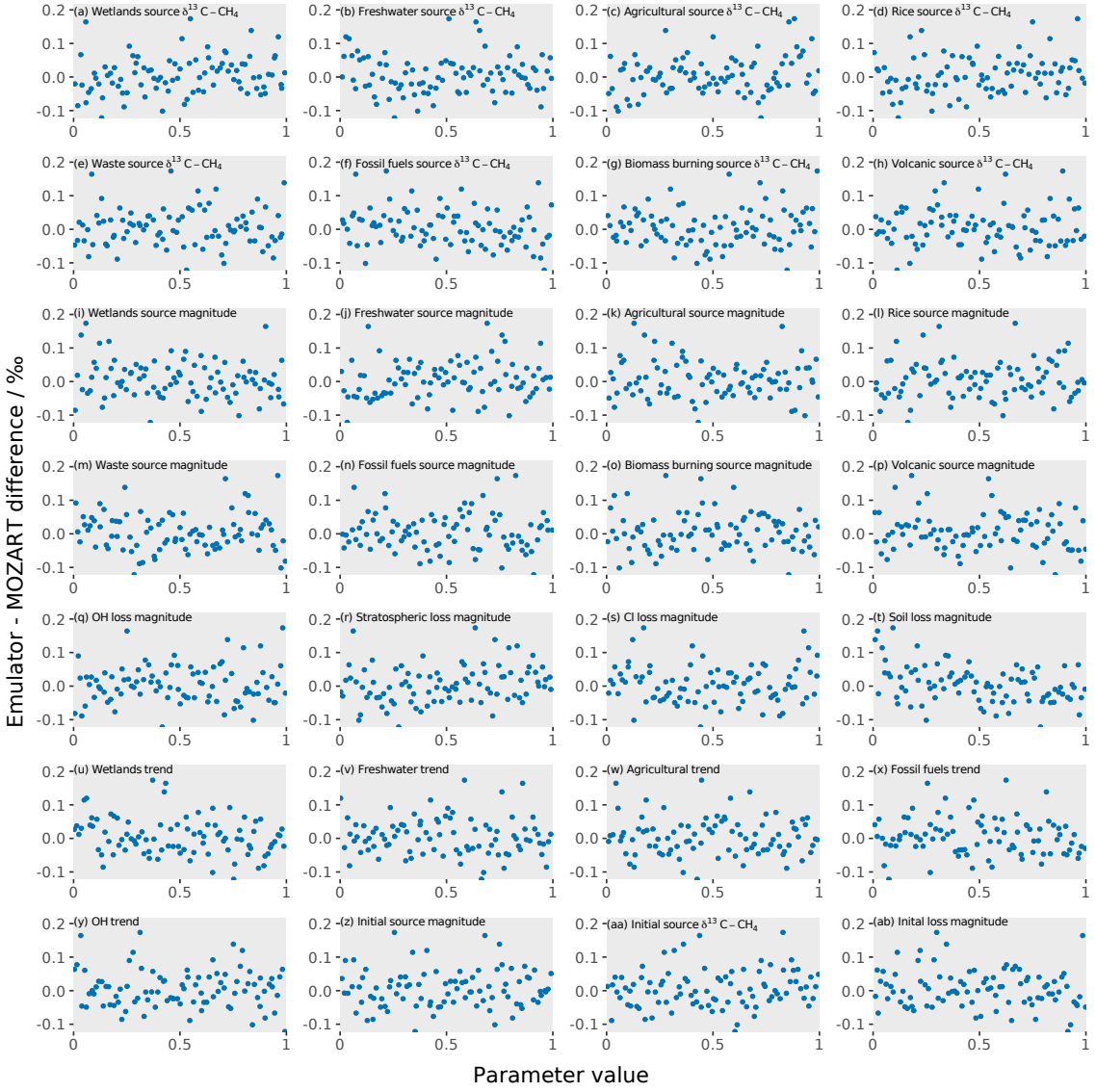

Figure 3.3.3: The difference between the southern hemisphere δ^{13}C-CH_4 emulator and the true value in the MOZART model for each of the 90 validation simulations, averaged over the time series, is plotted against the value of each input parameter in a separate panel.

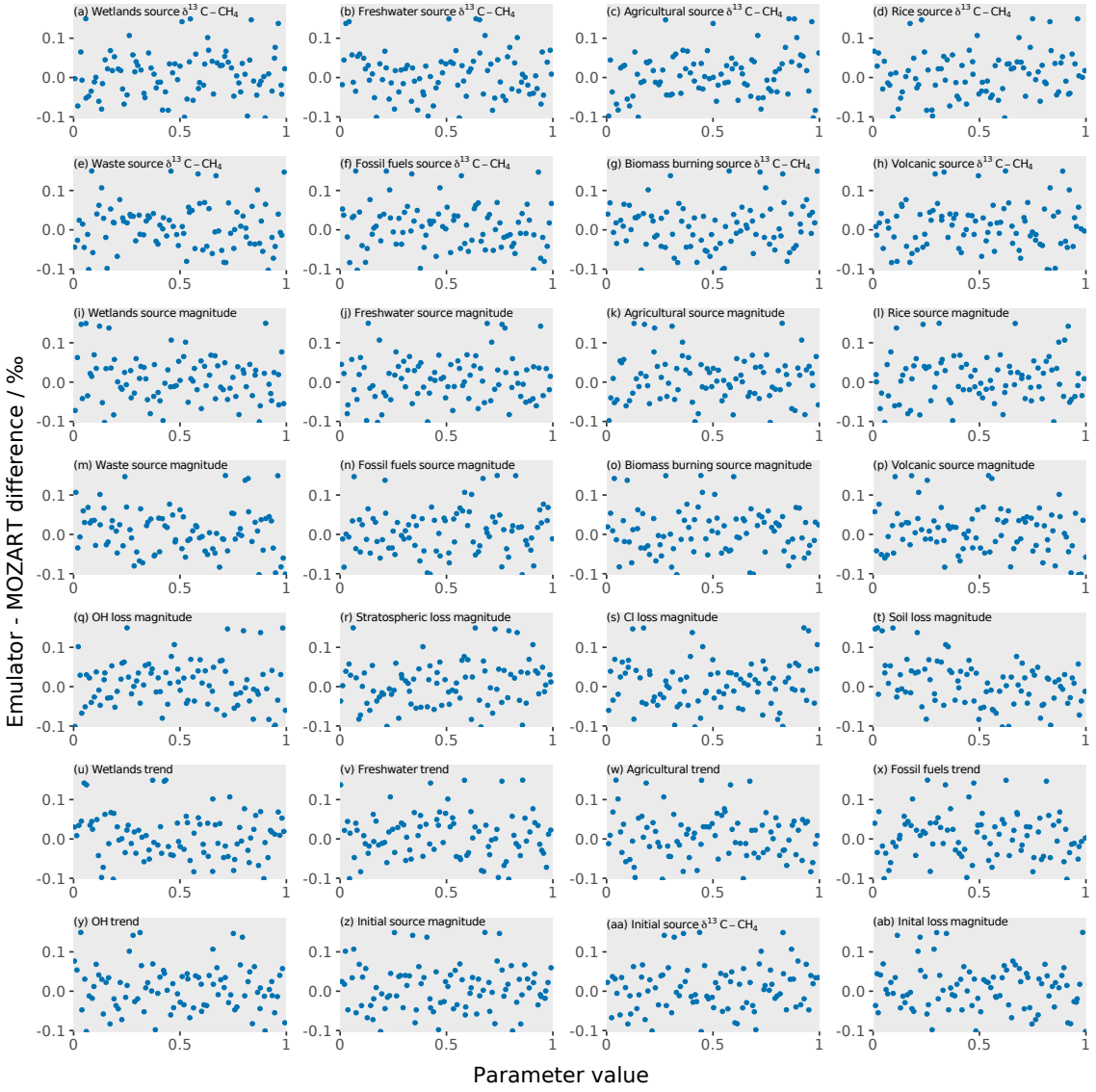

Figure 3.3.4: The difference between the northern hemisphere δ^{13}C-CH_4 emulator and the true value in the MOZART model for each of the 90 validation simulations, averaged over the time series, is plotted against the value of each input parameter in a separate panel.

3.3.2 Relation of emulator errors and outputs

For a Gaussian process, standardised differences between the emulator and the true model run should also be normally distributed. These differences are calculated by

$$\frac{y_{em} - y_{mzt}}{\sigma_{em}}, \tag{3.5}$$

where y_{em} is the emulator prediction for one month, y_{mzt} is the corresponding MOZART output, and σ_{em} is the emulator calculated error for that month. In the quantile-quantile plots of Figure 3.3.5, these differences between the emulator and the true model can be compared to a normal distribution. The black line is for the idealised case where the residuals are perfectly normally distributed. The main discrepancies are for the methane mole fraction emulators in the middle of the time series, where the emulator has over-predicted the error. This is because the emulator-estimated error is time-invariant, but the model output range is smaller in the middle of the time series, which is caused by the trend parameters (Section 2.3). The trend parameters have been designed to conserve the total magnitude of the source or sink over the time series. For example, a trend parameter that reduces a term by 20 % is applied as a 10 % increase in the first year, decreasing to no change in the middle of the time series, and then decreasing to -10 % in the final year. Therefore, all the possible trend values have the same magnitude in the centre of the time series, so there are fewer degrees of freedom here, and hence a smaller output range. This reduced output range is not seen in the δ^{13}C-CH_4 emulators due to the much longer time lag between input changes and δ^{13}C-CH_4 response.

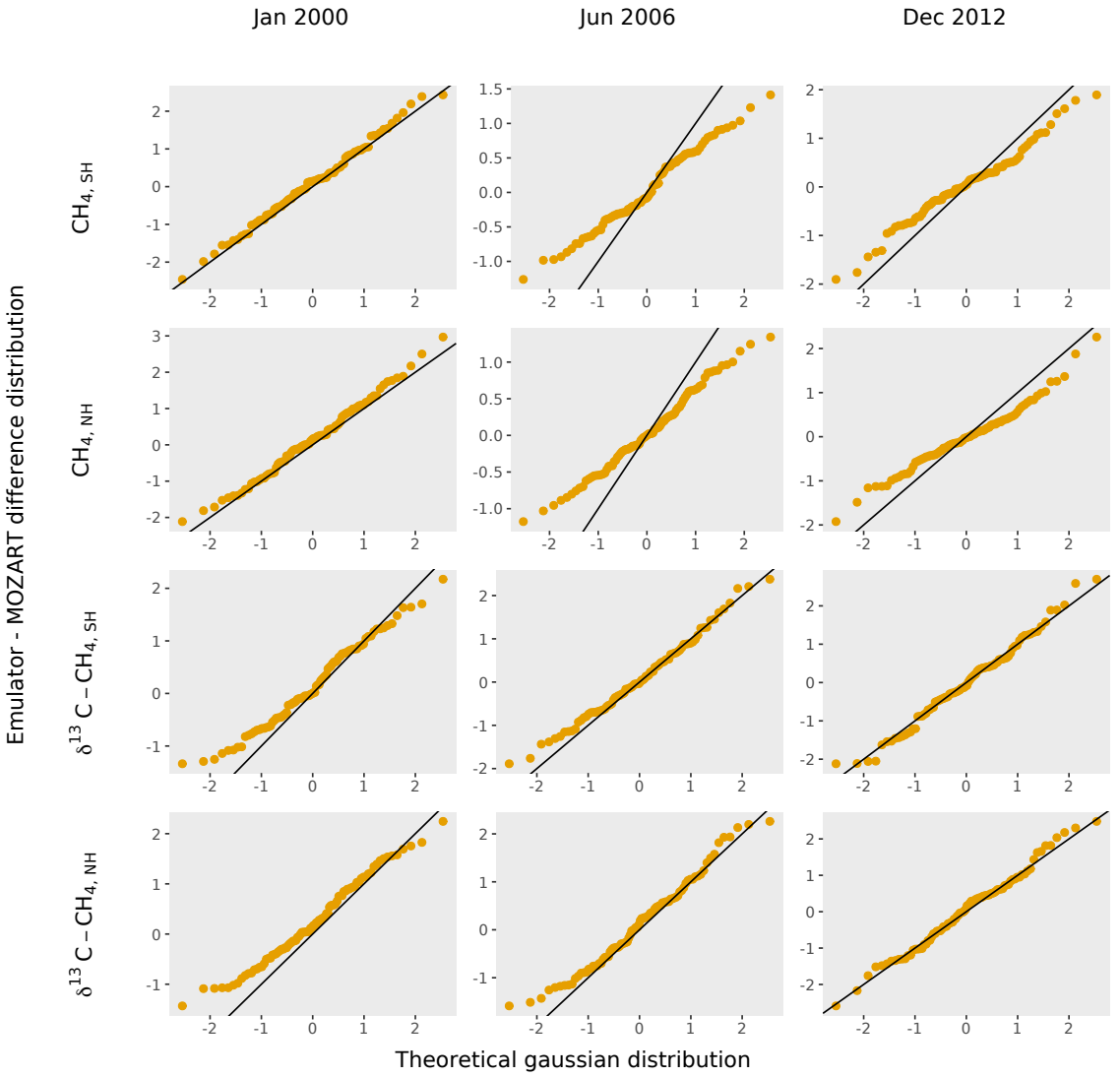

Figure 3.3.5: Quantile-quantile plots of the standardised emulator residuals for each hemispheric emulator (each row) at the beginning, middle, and end of the time series (each column). The black line, y=x, is plotted as a visual guide and represents the ideal case that the distribution of the residuals is perfectly Gaussian.

3.3.3 Auto-correlation functions

Mean auto-correlation functions were calculated for the MOZART simulations and the emulator predictions, which are shown in Figure 3.3.6. The emulators are able to replicate the time correlation structure seen in MOZART very well, and significantly better than either method of time series emulation presented in Conti & O'Hagan (2010). This is potentially because their complex model is less auto-correlated than

MOZART, which can be modelled as an AR(1) process (Equation 3.2). For less auto-correlated models other emulator set-ups, such as those discussed in Conti & O'Hagan (2010), may be more appropriate.

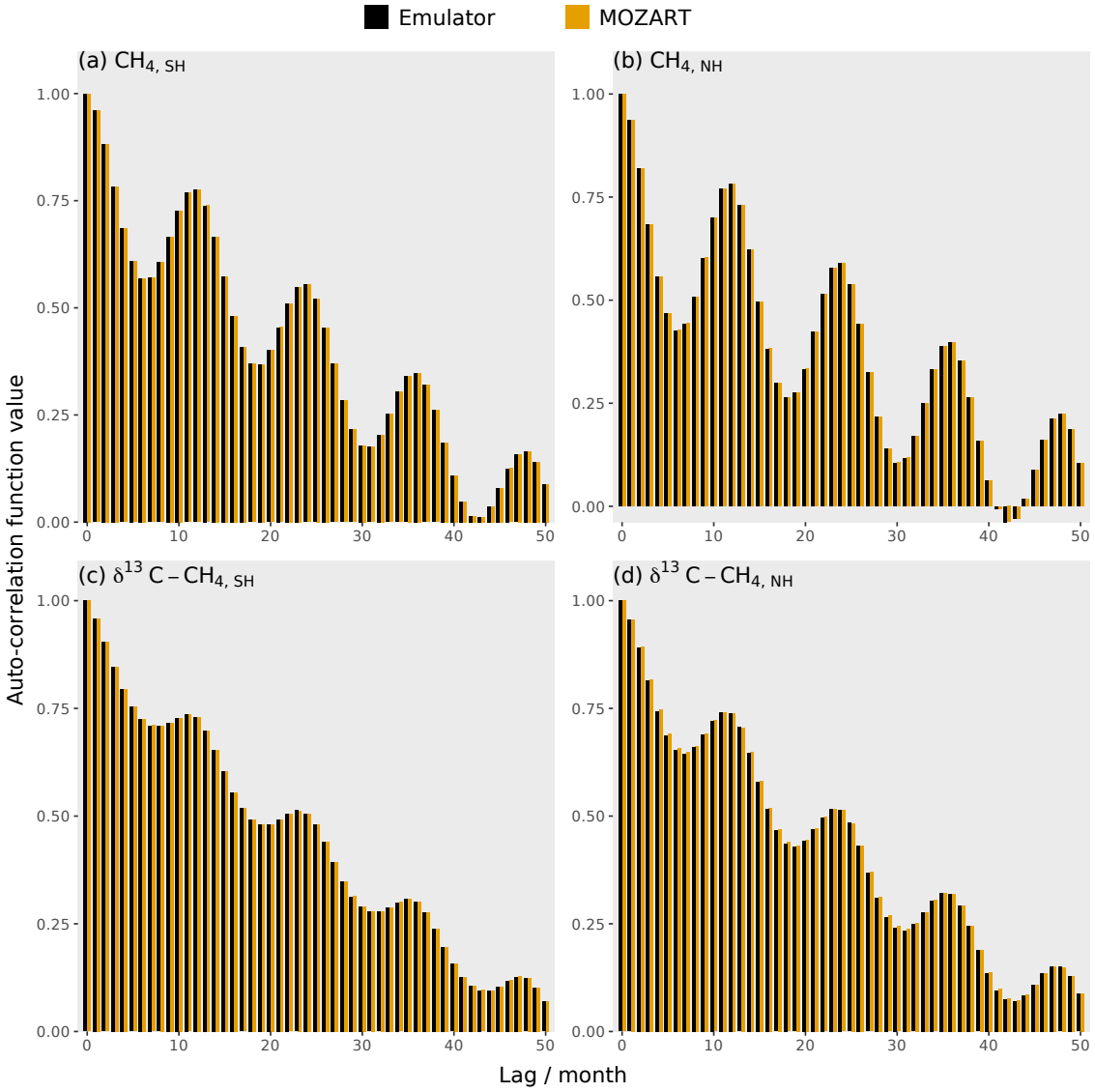

Figure 3.3.6: A comparison of the average auto-correlation function: MOZART is shown as the orange bars, and the emulators are shown as the black bars. Each panel shows a different output: (a) the southern hemisphere methane mole fraction, (b) the northern hemisphere methane mole fraction, (c) the southern hemisphere δ^{13}C-CH_4, and (d) the northern hemisphere δ^{13}C-CH_4.

3.3.4 The size of the emulator error compared to the model invariant parameter error

Using an emulator adds an extra source of uncertainty into our system. For the emulators to be useful, their error needs to be small in comparison to the other sources of error. The emulator error was calculated by predicting the validation dataset and comparing the predictions to the MOZART output, using the root mean squared error:

$$RMSE = \sqrt{\sum_{i=1}^{n} \frac{(y_{em} - y_{mzt})^2}{n}}, \tag{3.6}$$

where y_{em} is the emulator output, y_{mzt} is the MOZART output, and n is the number of simulations being compared. The RMSE was calculated to be about 1.2 ppb and 0.06 ‰ for the hemispheric methane mole fraction and δ^{13}C-CH_4 respectively. This emulator error is compared to the MOZART invariant parameter error in Figure 3.3.7. The MOZART invariant parameter error (Section 2.5.2) is comparatively large: about 10 ppb and 0.1 ‰, and can be considered a lower bound on the total MOZART error. The MOZART invariant parameter error is about three times the size of the emulator error for the methane mole fraction, and twice the size for δ^{13}C-CH_4. These errors are added in quadrature, so the MOZART invariant parameter error dominates.

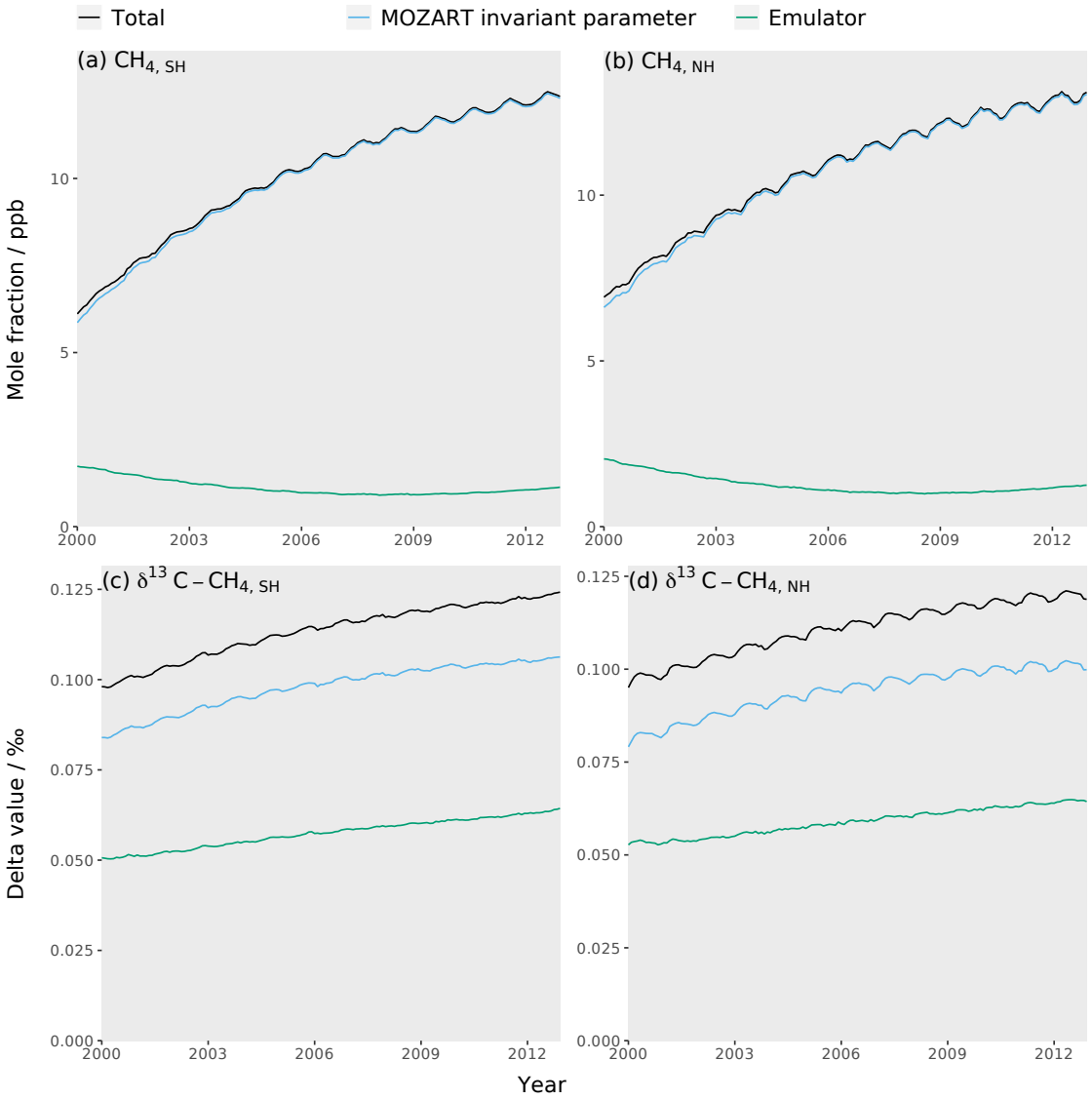

Figure 3.3.7: The MOZART invariant parameter (blue line), emulator (green line), and total (black line) errors for each of the four emulators: (a) the southern hemisphere methane mole fraction, (b) the northern hemisphere methane mole fraction, (c) the southern hemisphere δ^{13}C-CH_4, and (d) the northern hemisphere δ^{13}C-CH_4.

3.4 The number of runs required to build a useful Gaussian process

As the MOZART invariant parameter error is significantly larger than the emulator error (Section 3.3.4), it should be possible to use a less accurate emulator that requires fewer training runs. As making the training dataset is the most computa-

tionally expensive step in the emulation process, this would be beneficial for more time-consuming higher-resolution models.

The accuracy of the emulators trained with different numbers of runs is shown in Figure 3.4.1, which is measured by the temporal average of the root mean squared error (Equation 3.6). The residuals between the emulators and MOZART were calculated using leave one out cross validation (each simulation in the training dataset is removed in turn, and the emulator predicts this removed point). This figure shows that additional runs lead to a diminishing accuracy increase. For many applications, emulators with an error not much smaller than the MOZART invariant parameter error are satisfactory, as the invariant parameter error is an underestimate of the total MOZART error. Therefore, little more than 90 runs are required.

In general, the number of training runs required scales with the number of input parameters. However, if a few parameters dominate the output sensitivity (the problem is of lower dimensionality than it appears) and the parameter space is close to linear (only one more training simulation than the number of parameters would be needed if so) it is possible to train an accurate emulator with fewer runs (O'Hagan 2006). These conditions of lower dimensionality (Chapter 4) and close to linearity are met for the MOZART output, so the model could be run at a higher resolution and emulation would still be feasible if a reduced training datset was used.

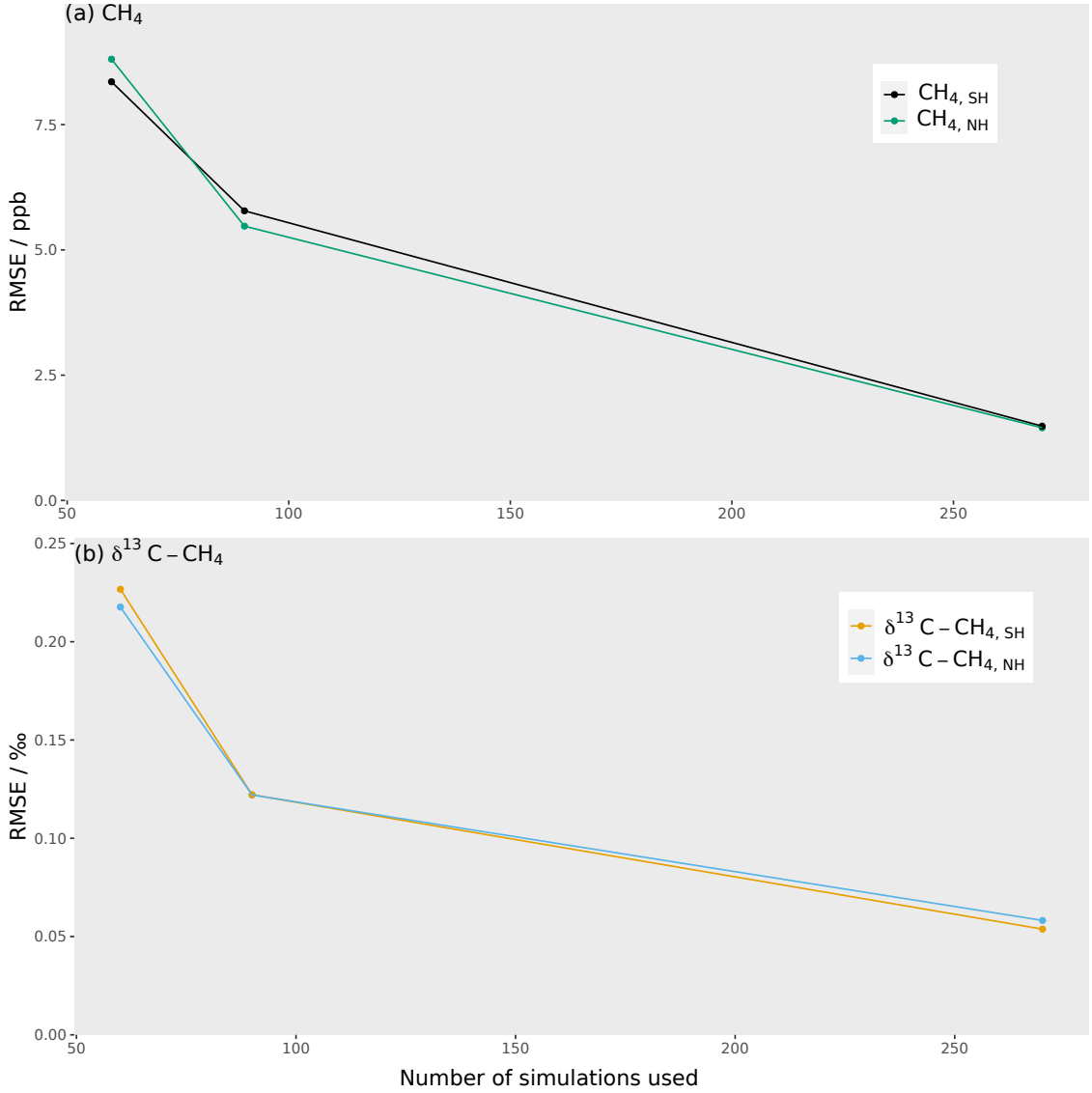

Figure 3.4.1: A plot showing how the root mean squared error (RMSE) between the emulator and MOZART changes for different numbers of training runs in the emulator. Each measurement type is shown in a separate panel: (a) the methane mole fraction, with the southern hemisphere in black and the northern hemisphere in green; and (b) δ^{13}C-CH_4, with the southern hemisphere in orange and the northern hemisphere in blue. There are only three points as each point requires a new Latin hypercube design in order to properly sample the parameter space with a different number of simulations. This means that each point requires a new set of MOZART training simulations, which is computationally expensive to repeat multiple times.

3.5 Comparison of multiple linear regression and the Gaussian process

The mean function of the Gaussian process is a multiple linear regression (Section 3.2). If the relationship between inputs and outputs is either linear or close to linear, with little parameter interaction (Section 4.3.2), then the multiple linear regression alone would be able to emulate MOZART. Multiple linear regression is advantageous as it requires a smaller training dataset (hence fewer MOZART simulations), and is simpler than a Gaussian process. The methane mole fraction input-output relationships have also been assumed to be linear and not interacting for small changes in the sources and sinks in many previous studies (e.g. McNorton et al. (2018)). Therefore, the performance of the two methods are compared in this section.

In Figure 3.5.1, the differences between MOZART and the multiple linear regression are compared to the differences between MOZART and the Gaussian process. The Gaussian process residuals are much smaller, with a root mean squared error of 1.0 ppb and 0.06 ‰, compared to 18 ppb and 0.17 ‰ for the multiple linear regression. This multiple linear regression error is large compared to the MOZART invariant parameter error, unlike the Gaussian process error (Section 3.3.4), so it would be harder to precisely match observations with multiple linear regression.

The methane mole fraction root mean squared error is 18 times larger for the multiple linear regression than for the Gaussian process, compared to three times for δ^{13}C-CH_4. The reason why the multiple linear regression performance is poorer can be examined by plotting the multiple linear regression residuals against the value of each of the input parameters. Any correlation between the size of the residual and the value of a parameter signifies that the output is not linear with respect to that parameter. From examining these correlations, the reason why the multiple linear regression is so much worse at predicting the methane mole fraction is its non-linearity with respect to the OH loss (Section 2.2.2). This non-linearity can be corrected for by using multiple linear regression of the methane mole fraction

with respect to a transformed OH parameter. Several transforms were tested (e.g. 1/[OH] and -ln([OH])), and the log was found to give the best fit, taking the root mean squared error of the multiple linear regression to 11 ppb, (the full residual distribution can be seen and compared in Figure 3.5.1). This uncertainty could, presumably, be decreased further if the training data was sampled with a Latin hypercube over the log-transformed input space. This is still significantly poorer than the Gaussian process, implying that the remaining small non-linearities and parameter interactions are important for predicting the output value.

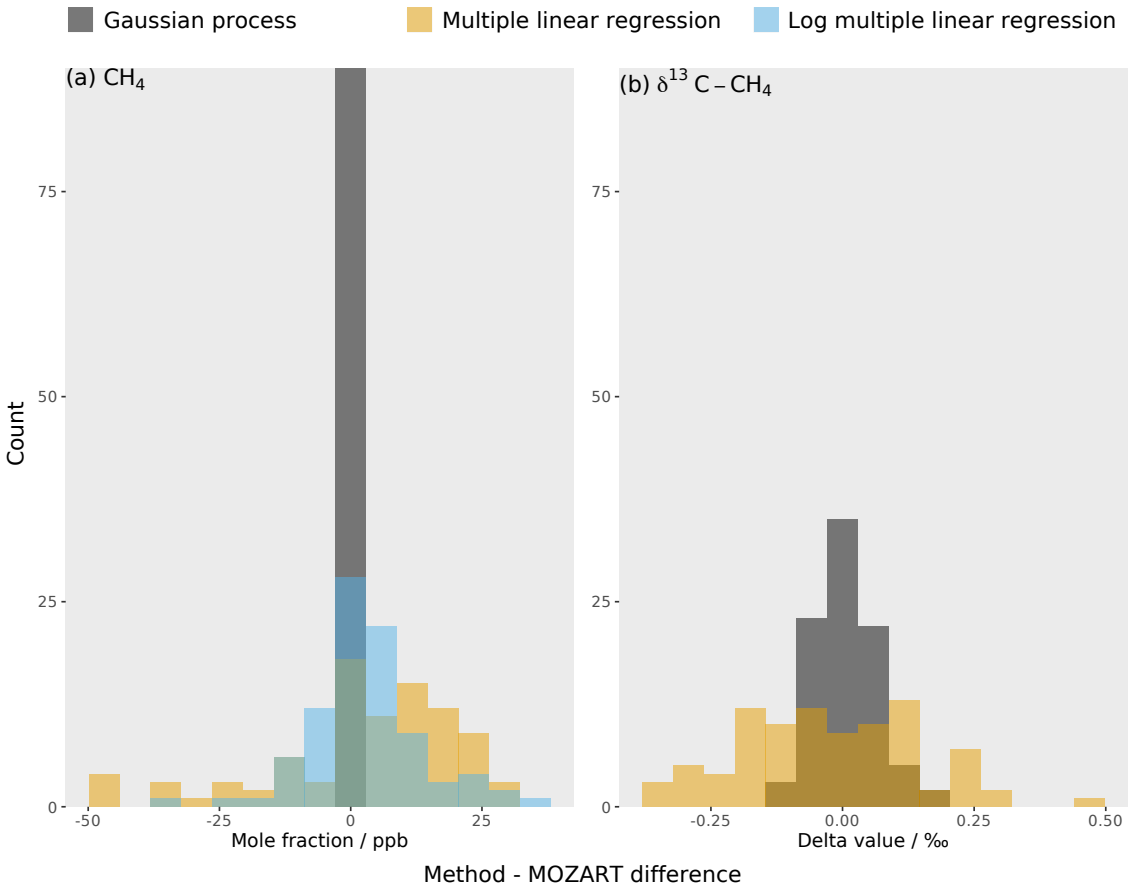

Figure 3.5.1: The residuals between the different methods (in different colours) and the true MOZART output for (a) the global mean methane mole fraction and (b) the global mean δ^{13}C-CH_4. Each emulator is built by a Gaussian process (grey) and a multiple linear regression (orange). The global methane mole fraction has an additional emulator: a multiple linear regression with log transformed OH (blue). The hemispheric emulators are averaged to produce a global mean and the histograms of the residuals are overlaid.

3.6 Summary

Gaussian processes have allowed emulators for a global three-dimensional CTM to be built, producing a fast and accurate approximation of the CTM output. Emulating a three-dimensional CTM allows high spatial resolution in the input fields and accounts for interannual variability in transport, which are generally not present in box models. Gaussian process emulation also accounts for non-linear relationships between inputs and outputs and provides an estimate of the additional uncertainty caused by using emulation.

The Gaussian process outperforms multiple linear regression at emulating atmospheric methane simulations: the Gaussian process root mean squared error is small in comparison to the MOZART invariant parameter error, whereas the multiple linear regression error is larger than the MOZART invariant parameter error. The poor performance of the multiple linear regression is because of the non-linearities and parameter interactions, in particular the non-linearity in the response of the methane mole fraction to the OH sink. However, multiple linear regression does have the advantages of requiring a smaller training dataset and being computationally simpler than a Gaussian process. Though, a balance between computational expense and precision can be achieved for CTMs where even hundreds of training simulations could be prohibitive. In this case little more than 100 simulations of the model are required to build a Gaussian process emulator with a root mean squared error similar to the MOZART invariant parameter error. This could make running MOZART at a higher resolution feasible.

In the following two chapters, the emulators are applied to two analyses that require millions of model simulations. At the computational expense of MOZART, these analyses would have been unfeasible, but become simple with the fast emulators. In Chapter 4 a sensitivity analysis is described, which aims to find the sources and sinks that the methane observations are most affected by. These most important sources and sinks can then be prioritised for further research in order to reduce the uncertainty in the methane budget. In Chapter 5, a parameter optimisation is carried out to test if the emulators can help to restrict the possible values of the

methane sources and sinks.

Chapter 4

The sensitivity of atmospheric methane observations to sources and sinks

4.1 Introduction

This chapter aims to find the methane sources and sinks whose uncertainties have the largest impacts on the modelled methane mole fraction and δ^{13}C-CH_4. This is done with a sensitivity analysis, and as far as we aware, is the first application of this method to methane modelling. The sources and sinks identified as having the largest impacts on the methane mole fraction and δ^{13}C-CH_4 can then be prioritised for further research in order to reduce their uncertainty, and hence the uncertainty in the methane budget.

For complex models, such as MOZART, one-at-a-time sensitivity tests (where only one parameter is perturbed from a baseline case) are often carried out (e.g. Bailis et al. (2005), Campbell et al. (2008), and several others of this type of study are discussed in Saltelli & Annoni (2010)). However, the use of this method for complex models has been rebuked by the statistical community (Saltelli & Annoni 2010) as it has two main disadvantages. The first is that it ignores the interaction of parameters, and the effect of changing parameters together may be greater than changing the

parameters independently. This assumption of non-interacting parameters is only valid for an additive model (Saltelli et al. 2000), which complex models are invariably not. The second issue is the large number of parameters in a complex model. By only perturbing one parameter at once, one-at-a-time tests cover a fraction of the parameter space that tends to zero as the number of parameters increases (Saltelli & Annoni 2010).

There are other sensitivity tests available, but these require many more simulations, which are unfeasible for the time taken to produce simulations from complex models. For example, variance-based sensitivity analysis (Saltelli et al. 2000) often requires millions of simulations. However, this method does allow the calculation of parameter interactions and gives an answer that is representative of a far larger fraction of a high-dimensional parameter space.

The emulators from Chapter 3 can be used for sensitivity analysis instead of running MOZART for each combination of model inputs. By using an emulator, only the $\sim 10^2$ MOZART simulations (Chapter 2) required to train the emulators are needed, along with $\sim 10^6$ emulator simulations for the sensitivity analysis itself. This makes it much faster than running MOZART for each of the $\sim 10^6$ sensitivity test cases. Therefore, use of the fast emulators makes the variance-based sensitivity analysis presented in this chapter feasible. This is advantageous because the interaction of parameters can cause a large fraction of the output variance in a non-additive model (Saltelli et al. 2000), such as MOZART. This means that a parameter that appeared as a minor contributor to the output variance in one-at-a-time tests, can be a major contributor in the variance-based sensitivity analysis. By using a variance-based sensitivity test we ensure that all parameters whose uncertainty strongly affects the methane observations are identified.

4.2 Method

4.2.1 The sensitivity indices

The sensitivity of the MOZART output to its inputs can be quantified using sensitivity indices, which measure the proportion of the output variance explained by an input parameter being varied over its possible range (Saltelli et al. 2000). In this thesis, two sensitivity indices are calculated: the first order and total effect indices. The first order sensitivity index reflects the proportion of the variance in the output that can be attributed to a single parameter. This can be calculated as

$$S_k = \frac{V[E(y|x_k)]}{V(y)}, \tag{4.1}$$

where $V[E(y|x_k)]$ is the variance in the expected value of the emulator output y given the value of parameter x_k, and $V(y)$ is the variance in the emulator output caused by all parameters.

The total effect index is the proportion of the output variance that can be explained by a single parameter and its interactions with all other parameters. This can be calculated as

$$S_{T_k} = 1 - \frac{V[E(y|x_{\sim k})]}{V(y)}, \tag{4.2}$$

where $V[E(y|x_{\sim k})]$ is the variance in the expected value of y caused by all parameters except x_k. A parameter's interactions with other parameters can be calculated by the difference between the total sensitivity index and the first order sensitivity index. These sensitivity indices were calculated using the Monte-Carlo methods (Saltelli et al. 2000) presented in Section 4.2.2.

4.2.2 The Monte-Carlo calculation of the sensitivity indices

A Sobol sequence (Sobol' 1967, Antonov & Saleev 1979) (a quasi-random space filling algorithm) was used to choose parameter combinations and ensure good coverage of

the input parameter space. For example, a one-dimensional Sobol sequence covering a parameter that varies from 0 to 1 will start with x_0, a random number between 0 and 1, and subsequent values (x_1, x_2, x_3, x_4, x_5 etc.) will differ from x_0 by 0.5, 0.75, 0.25, 0.375, 0.875 etc. In higher dimensions, the same numbers appear in the Sobol sequence but in a different order, so that the samples are well distributed in parameter space.

In this work, a (N, $2k$) matrix from a Sobol sequence was generated, where N is the number of model simulations (1 680 000) and k is the number of input parameters (28). This matrix was split into two smaller (N, k) matrices: $\boldsymbol{A}$ and $\boldsymbol{B}$. A third matrix $\boldsymbol{C_i}$, was constructed by replacing the i^{th} column of $\boldsymbol{B}$ with the i^{th} column of $\boldsymbol{A}$. The three matrices are input to the emulators to generate N model outputs each: $\boldsymbol{y}_A$, $\boldsymbol{y}_B$, and $\boldsymbol{y}_{C_i}$. This means that 50.4 million ($N \times (k+2)$) runs of the emulators are required. Using these matrices, the first order sensitivity indices can be calculated by

$$S_i = \frac{\frac{1}{N}\sum_{j=1}^{N} \boldsymbol{y}_A^j \boldsymbol{y}_{C_i}^j - f_0^2}{\frac{1}{N}\sum_{j=1}^{N} (\boldsymbol{y}_A^j, \boldsymbol{y}_B^j)^2 - f_0^2}, \tag{4.3}$$

where $(\boldsymbol{y}_A^j, \boldsymbol{y}_B^j)$ is $\boldsymbol{y}_A^j$ and $\boldsymbol{y}_B^j$ concatenated, and

$$f_0^2 = \left(\frac{1}{N}\sum_{j=1}^{N} (\boldsymbol{y}_A^j, \boldsymbol{y}_B^j)\right)^2. \tag{4.4}$$

This formula can be thought of as working as $\boldsymbol{A}$ and $\boldsymbol{C_i}$ have different parameter values for all parameters except the i^{th} parameter. If the i^{th} parameter has a large effect on the output then the elements of $\boldsymbol{y}_A$ and $\boldsymbol{y}_{C_i}$ will be highly correlated. However, if the i^{th} parameter is unimportant then the elements of $\boldsymbol{y}_A$ and $\boldsymbol{y}_{C_i}$ are randomly distributed. When $\boldsymbol{y}_A$ and $\boldsymbol{y}_{C_i}$ are highly correlated, S_i will be larger as large elements of $\boldsymbol{y}_A$ are multiplied by large values of $\boldsymbol{y}_{C_i}$.

The total effect indices can be calculated by

$$S_{T_i} = 1 - \frac{\frac{1}{N}\sum_{j=1}^{N} \boldsymbol{y}_B^j \boldsymbol{y}_{C_i}^j - f_0^2}{\frac{1}{N}\sum_{j=1}^{N} (\boldsymbol{y}_A^j, \boldsymbol{y}_B^j)^2 - f_0^2}. \tag{4.5}$$

This formula can be thought of as working because $\boldsymbol{B}$ and $\boldsymbol{C_i}$ only have different parameter values for the i^{th} parameter. This means that the fractional part of Equation 4.5 of $\boldsymbol{y}_B$ and $\boldsymbol{y}_{C_i}$ is the first order sensitivity for all parameters but the i^{th} parameter. The remainder of the sensitivity is caused by the i^{th} parameter and its interactions with the other parameters, hence the subtraction from one.

Uncertainty in these indices was calculated using bootstrap resampling, where N samples from $\boldsymbol{y}_A$, $\boldsymbol{y}_B$, and $\boldsymbol{y}_{C_i}$ are drawn with replacement, and the sensitivity indices recalculated. This was repeated 10 000 times, and the standard deviation in the 10 000 indices is taken as an estimate of the uncertainty.

Gaussian process emulation does allow the sensitivity indices to be calculated more computationally efficiently using integration (Oakley & O'Hagan 2004), which has been made widely accessible with the free GEM-SA software (Kennedy 2009, Lee et al. 2011). However, GEM-SA does not allow the inclusion of time correlation used in the emulators constructed in this thesis (Section 3.2.2).

4.3 Results and discussion

The first order sensitivity indices and parameter interactions are presented and discussed in Sections 4.3.1 and 4.3.2, respectively. In this sensitivity analysis, constraint on the parameter ranges from comparing the observations and the MOZART output has not been considered. The parameters that the outputs are most sensitive to are most likely to be constrained by observations (Chapter 5). Therefore, if observational constraint was considered in this sensitivity analysis, the methane mole fraction and δ^{13}C-CH_4 would appear sensitive to more parameters than presented here. However, the full parameter ranges explored here provide a more complete

representation of our understanding of the methane budget, as they include values derived from a multitude of studies, both bottom-up and top-down.

4.3.1 First order sensitivity indices

The sensitivity of the MOZART outputs to the input parameters is examined in Figure 4.3.1. The first order sensitivity indices (Equation 4.1) shown in this plot give the proportion of the output variance due to varying that parameter. In this section, each of the output sensitivity plots is examined.

Figure 4.3.1a shows that the global mean methane mole fraction sensitivity is dominated by the OH loss magnitude (73 %), with contributions from the freshwater (13 %) and wetlands (8 %) source magnitudes. This order predictably follows the absolute size of the uncertainty in the source and loss magnitudes, illustrated in Figure 1.2.1.

The global mean δ^{13}C-CH_4 depends on a different set of parameters, which are shown in Figure 4.3.1b. The three parameters that the global mean δ^{13}C-CH_4 is most sensitive are: the Cl sink magnitude (27 %), the agricultural source δ^{13}C-CH_4 (16 %), and the initial condition source δ^{13}C-CH_4 (16 %), with several other parameters contributing significantly: the freshwater source magnitude, the wetlands source magnitude, and the stratospheric loss magnitude. The fact that methane mole fraction and δ^{13}C-CH_4 are sensitive to different parameters, means that δ^{13}C-CH_4 is a complementary measurement to the methane mole fraction. However, two of the parameters that δ^{13}C-CH_4 is most sensitive to are δ^{13}C-CH_4-specific (the agricultural source δ^{13}C-CH_4 and the initial condition source δ^{13}C-CH_4), and do not on their own, provide new information about the magnitudes of the different sources and sinks in the methane budget. Unlike the global mean methane mole fraction, the ordering of the parameters that the global mean δ^{13}C-CH_4 is most sensitive to does not simply follow the absolute uncertainty sizes. The parameter that δ^{13}C-CH_4 is most sensitive to is the Cl loss magnitude, which has a small uncertainty compared to other terms, but it is highly fractionating. The next parameter is the agricultural

source δ^{13}C-CH_4, which does have a large uncertainty compared to other source δ^{13}C-CH_4 signatures, but also is significantly more negative than the atmospheric δ^{13}C-CH_4 compared to other sources, so that changes in this value have a larger effect on the atmospheric δ^{13}C-CH_4. The high sensitivity to the initial condition source δ^{13}C-CH_4 is due to the long response time of δ^{13}C-CH_4 in the atmosphere compared to the length of time examined here.

The methane mole fraction inter-hemispheric difference (calculated as the temporal mean over the northern hemisphere minus the southern hemisphere as in Section 2.4.3) is most sensitive to the freshwater (66 %), fossil fuel (15 %), and wetlands (8 %) source magnitudes as shown in Figure 4.3.1c. These are parameters with large uncertainties and large differences in emissions between the hemispheres, as shown in Figure 2.2.7. The parameter with the largest uncertainty, the OH loss magnitude, has been assumed in this study to have very little difference in concentration between the two hemispheres (Patra et al. 2014), explaining the low sensitivity for this output. However, had the uncertainty in the hemispheric distribution of OH been included, it would likely be a large proportion of the sensitivity.

The δ^{13}C-CH_4 inter-hemispheric difference (Figure 4.3.1d) has many more parameters that it is sensitive to than the methane mole fraction inter-hemispheric difference. The parameters with the largest first order sensitivity indices are: the initial condition source δ^{13}C-CH_4 (22 %), the Cl sink magnitude (18 %), and the fossil fuel source δ^{13}C-CH_4 (12 %). There are also significant contributions from the stratospheric loss magnitude, the OH loss magnitude, and the wetlands source magnitude. The order of these sensitivities is similar to the δ^{13}C-CH_4 global mean, but terms with a large difference between the hemispheres are more important. Fossil fuel emissions have a large uncertainty and large difference between the hemispheres, so the source magnitude and δ^{13}C-CH_4 signature of this source are more important than the other sources, apart from wetlands and fresh water.

Both methane mole fraction and δ^{13}C-CH_4 trends (calculated as the global mean in December 2012 minus December 2000 as in Section 2.4.3) are primarily sensitive to a single parameter, which is shown in Figures 4.3.1e and 4.3.1f respectively. The

methane mole fraction trend is dominated by the OH loss magnitude (58 %) and the δ^{13}C-CH_4 trend is dominated by the initial condition source δ^{13}C-CH_4 (71 %). The OH loss trend (15 %), freshwater source magnitude (9 %), and wetlands source magnitude (6 %) contribute significantly to the methane mole fraction trend, and the agricultural source δ^{13}C-CH_4 (11 %) to the δ^{13}C-CH_4 trend. The combination of the OH loss magnitude and trend as the most sensitive for the methane mole fraction trend is due to the OH loss term having the largest uncertainty in terms of absolute methane of any parameter (Figure 1.2.1). The initial condition's dominance over the δ^{13}C-CH_4 trend is due to the slow response time in the atmospheric δ^{13}C-CH_4, so that the trend is largely dependent on its starting point. This work does examine a large range of δ^{13}C-CH_4 initial condition values (Table 2.6), but this parameter is important even over small ranges. If the δ^{13}C-CH_4 initial condition is perturbed by 0.1 ‰ (a more typical uncertainty when the initial conditions are constrained by observations) from the initial median parameter values, the output atmospheric δ^{13}C-CH_4 trend changes by 0.04 ‰. This is almost half the δ^{13}C-CH_4 trend in the observations, so represents a serious challenge for using the δ^{13}C-CH_4 measurements to constrain the recent changes in the methane budget.

This sensitivity analysis highlights several challenges that are important to consider in methane inverse modelling studies. Three parameters shown to be important are often ignored: the OH sink is often assumed to be known (e.g. Schaefer et al. (2016), Worden et al. (2017)), as is the Cl sink (e.g. Nisbet et al. (2016), Rigby et al. (2017)) or the Cl sink is left out completely (e.g. Turner et al. (2017)); and this work is the first to include the freshwater source explicitly, not just as part of the total source. δ^{13}C-CH_4 measurements are sometimes not used (e.g. Bousquet et al. (2011)), although due to its sensitivity to many parameters that methane mole fraction is insensitive to, it should provide useful and complementary information. However, its slow response time in the atmosphere means that the model output is highly sensitive to the initial conditions. Therefore, this source of uncertainty is critical in studies of the global methane budget, which use δ^{13}C-CH_4 measurements, over timescales of less than decades.

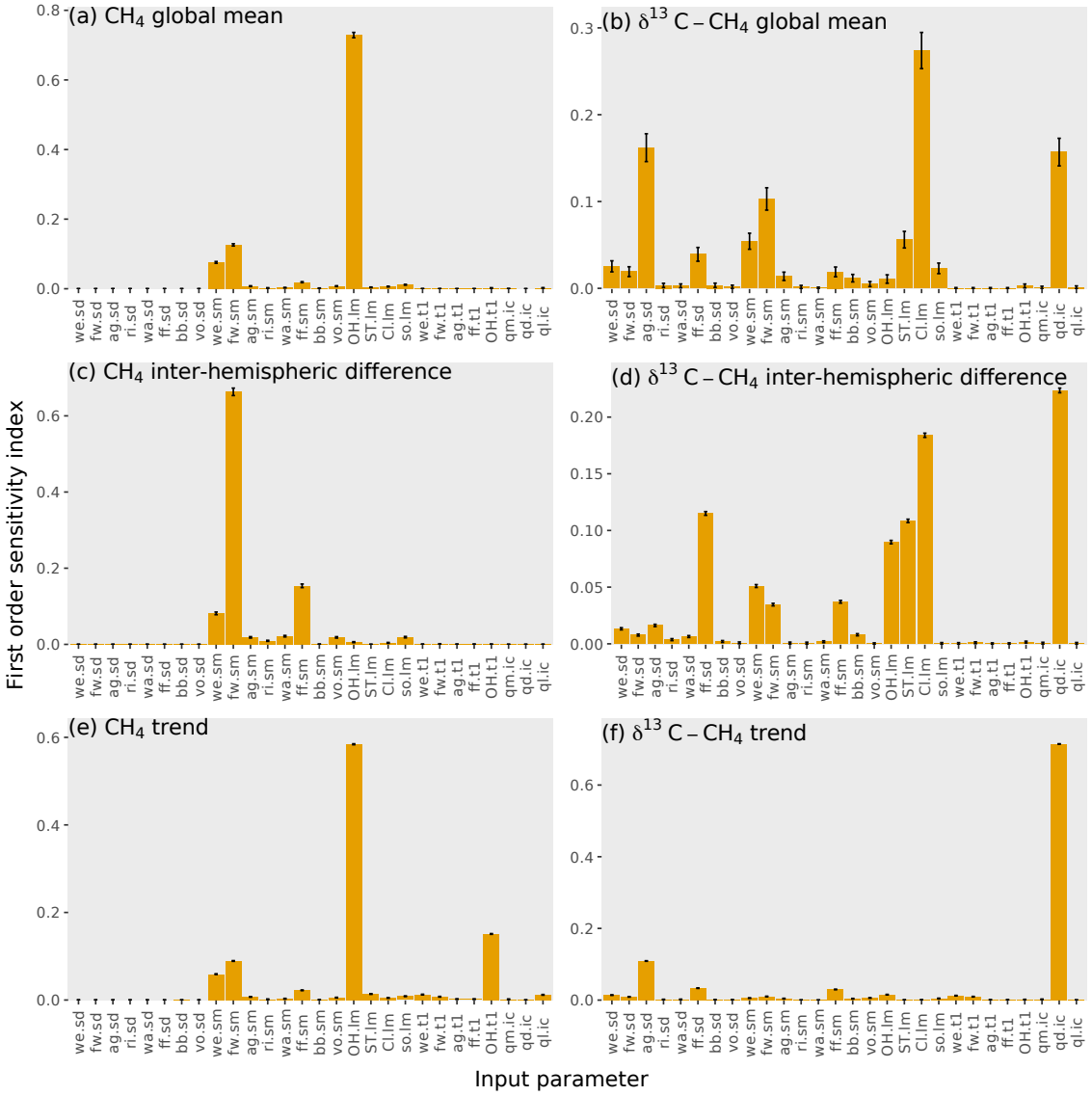

Figure 4.3.1: The first order sensitivity coefficients to the input parameters for six outputs: (a) methane mole fraction global mean, (b) δ^{13}C-CH_4 global mean, (c) methane mole fraction inter-hemispheric difference, (d) δ^{13}C-CH_4 inter-hemispheric difference, (e) methane mole fraction trend, and (f) δ^{13}C-CH_4 trend. The values given here are for the temporal mean of the time series. The input parameter codes are given by a combination of a two character code giving the source or loss, (wetlands (we), fresh water (fw), agriculture (ag), rice (ri), waste (wa), fossil fuels (ff), biomass burning (bb), volcanoes (vo), hydroxyl radical (OH), stratospheric (ST), Cl radical (Cl), soil (so), total source magnitude (qm), total source δ^{13}C-CH_4 (qd), total loss imbalance (ql)) and another code giving the type of parameter, (source δ^{13}C-CH_4 (sd), source magnitude (sm), loss magnitude (lm), temporal trend (t1), initial condition (ic)). The error bars are the uncertainties in the indices, calculated by bootstrap resampling as described in Section 4.2.2.

4.3.2 The interactions of the parameters

The total effect (Equation 4.2) of each parameter was calculated, allowing the interaction between parameters to be calculated by subtracting the first order sensitivity from the total effect. The interaction of a parameter is the proportion of the output variance explained by changing that parameter alongside the other parameters, removing the effect of changing the parameter independently of the other parameters. The interactions are shown in Figure 4.3.2 and were found to be small, 3 % at most. The interactions across all parameters account for 9 % of the output variance in the δ^{13}C-CH_4 inter-hemispheric difference, and at most 1 % for the other five outputs. This means, for the purpose of a sensitivity analysis, that we can essentially consider the effect of each input independently, and in this case, one-at-a-time tests would have produced a similar result.

An example of a parameter that might have been expected to show interaction effects is the OH loss magnitude with source magnitude parameters for the methane mole fraction output: if the OH concentration is low, then a change in emissions would be expected to have a larger effect on the methane mole fraction than if the OH concentration was higher. Consider the extreme case that the OH concentration is zero, then almost all methane emissions would remain in the atmosphere and increase the methane mole fraction greatly. However, as the OH concentration increases, more of the emissions are removed, and emissions of the same magnitude produce a smaller change in the methane mole fraction. For the δ^{13}C-CH_4, source magnitudes and δ^{13}C-CH_4 signatures would be expected to interact. This time, consider a source with zero emissions. Changing this source's δ^{13}C-CH_4 will have no effect on atmospheric δ^{13}C-CH_4. However, as the emissions of this source increase, as will the resulting change in atmospheric δ^{13}C-CH_4. The very small interaction of the parameters in the examples above means that these effects are negligible compared to the effect of just changing the single parameter within its uncertainty range. This is because, in these examples, the interactions are going to be greatest when parameter values are close to zero, which none of the source or loss magnitudes included are, and the parameter ranges are too small for this effect to become significant.

Whilst the interactions are small in terms of a sensitivity analysis, for the purpose of building an accurate emulator, these small interactions are important. For example, the 0.2 % and 0.9 % output variance accounted for by parameter interactions in the global mean mole fraction and global mean δ^{13}C-CH_4, respectively, is equivalent to a standard deviation of 10 ppb and 0.13 ‰ in the output. These standard deviations are large compared to the quantities that the emulator is trying to predict (e.g. inter-hemispheric difference or trends). These values account for most of the difference in performance of the Gaussian process and multiple linear regression, which does not consider parameter interactions, in Section 3.5.

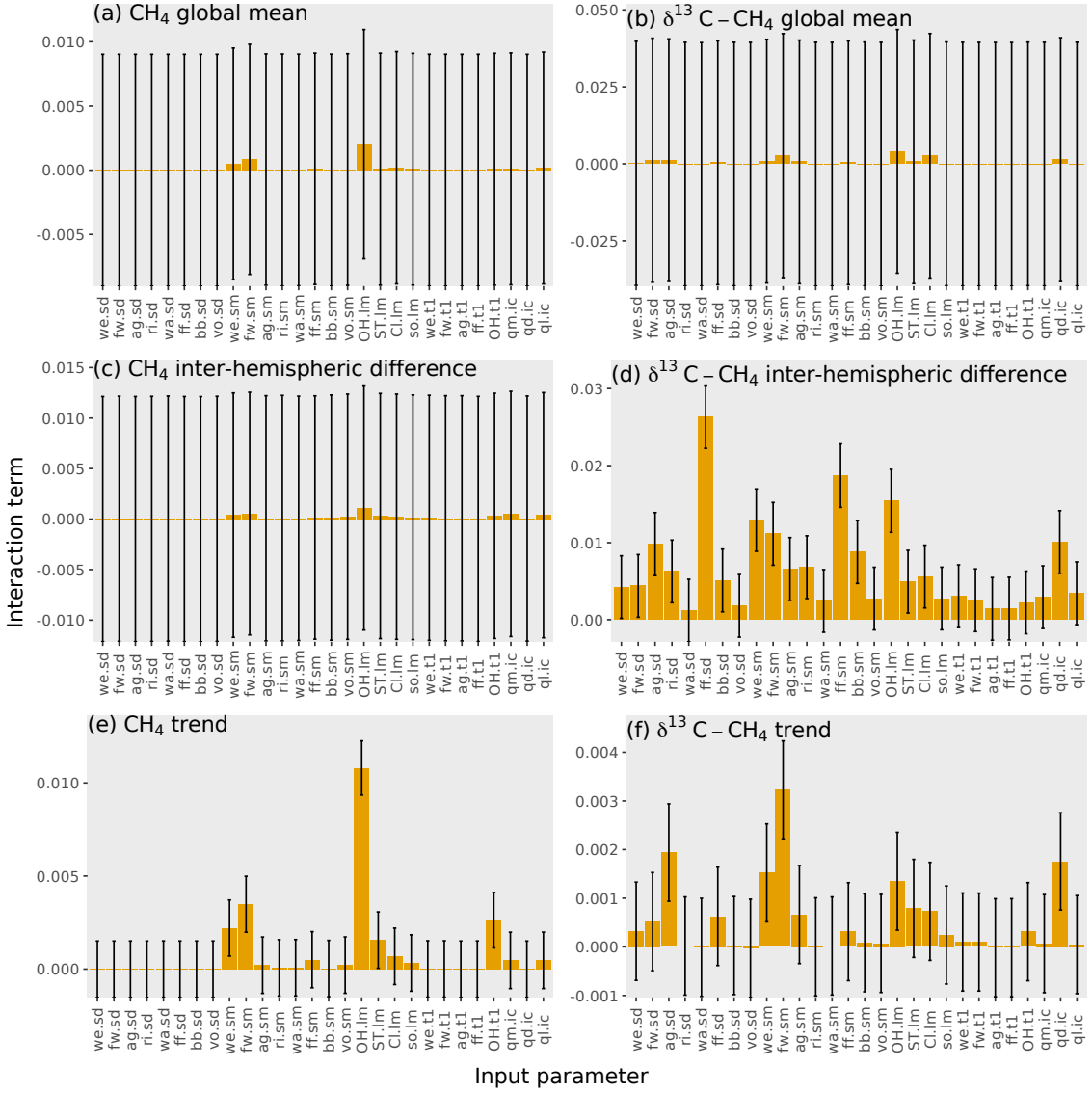

Figure 4.3.2: The interaction terms of the parameters for each of the outputs: (a) methane mole fraction global mean, (b) δ^{13}C-CH_4 global mean, (c) methane mole fraction inter-hemispheric difference, (d) δ^{13}C-CH_4 inter-hemispheric difference, (e) methane mole fraction trend, and (f) δ^{13}C-CH_4 trend. The values given here are for the temporal mean of the time series. The input parameter codes are given by a combination of a two character code giving the source or loss, (wetlands (we), fresh water (fw), agriculture (ag), rice (ri), waste (wa), fossil fuels (ff), biomass burning (bb), volcanoes (vo), hydroxyl radical (OH), stratospheric (ST), Cl radical (Cl), soil (so), total source magnitude (qm), total source δ^{13}C-CH_4 (qd), total loss imbalance (ql)) and another code giving the type of parameter, (source δ^{13}C-CH_4 (sd), source magnitude (sm), loss magnitude (lm), temporal trend (t1), initial condition (ic)). The error bars are the uncertainties in the indices, calculated by bootstrap resampling as described in Section 4.2.2.

4.4 Conclusions

In this chapter, the first comprehensive sensitivity analysis of modelled atmospheric methane mole fraction and δ^{13}C-CH_4 to sources and sinks was presented. The speed of emulation allowed many more MOZART outputs to be generated than would be possible by running MOZART itself, permitting a thorough variance-based sensitivity analysis to be carried out, which required over a million simulations. This analysis identified the sources and sinks whose uncertainty contributes the most to the uncertainty in the modelled methane output. If the uncertainty in these terms could be reduced, there would be the most significant gains in the understanding of the methane budget. Hence, these parameters should be a priority for further research. In order of decreasing importance, we find that these parameters are: the OH loss magnitude and freshwater source magnitude for the methane mole fraction; and Cl loss magnitude for δ^{13}C-CH_4. Additionally, if δ^{13}C-CH_4 is to be fully utilised, measurements and modelling methods must be developed to reduce uncertainty in the δ^{13}C-CH_4 initial conditions and some source signatures (particularly for agriculture).

The sensitivity analysis demonstrated some of the challenges with current methane modelling. In previous studies, the OH sink is often held constant and assumed to be known precisely, similarly, the Cl sink is assumed to be constant or not included at all, and the freshwater source is often omitted (Section 2.2.3). However, methane mole fraction and δ^{13}C-CH_4 magnitudes, trends, and inter-hemispheric differences are highly sensitive to these parameters, so their uncertainty must be considered. Furthermore, as variation within their uncertainties can cause large changes in the modelled methane output, changes in these parameters are candidates for the cause of the recent changes, and so should be included as separate terms to be solved for. The δ^{13}C-CH_4 measurements should be a useful addition to the methane mole fraction in order to constrain the sources and sinks of methane, as they are sensitive to many model parameters to which methane mole fraction observations are insensitive. However, many parameters that the isotopologue measurements are most sensitive to are δ^{13}C-CH_4-specific, and do not, on their own, provide additional information

about the magnitudes of the different sources and sinks needed to constrain the methane budget (e.g. source δ^{13}C-CH_4 signatures). The δ^{13}C-CH_4 measurements (global mean, inter-hemispheric difference, and trend) are also highly sensitive to the initial conditions, and so these must be well constrained in order for δ^{13}C-CH_4 to be useful.

Chapter 5

Using emulators to quantify the global atmospheric methane budget

5.1 Introduction

Chapter 4 identified the methane sources and sinks whose uncertainty contributes the most to the variance in modelled methane mole fraction and δ^{13}C-CH_4. These are the sources and sinks that are most important to reduce uncertainty in order to understand the drivers of change in atmospheric methane observations. The next question is whether the emulators can be used to help with this uncertainty reduction in the most important terms in the methane budget. This can be achieved by examining the probability that the inputs to MOZART (which parameterise the methane sources and sinks) are the true inputs, given a set of observations. Using this probability, input parameter values that are inconsistent with observations can be discarded, reducing the range of possible values for the parameters, and hence for methane sources and sinks. In this way, this chapter uses the emulators to determine the ranges of the methane sources and sinks that are consistent with observations.

The method builds on the work of the previous chapters: the MOZART simulations in Chapter 2 are used to build the emulators described in Chapter 3, which predict

MOZART outputs at untested input parameter values in this chapter. These emulator outputs can be compared to the observations using the method outlined in Section 5.2, which splits the emulator outputs into those that are consistent with observations and those that are not. The emulator outputs that match the observations are examined in Section 5.3, before looking at the input parameters of these simulations in Section 5.4. How much constraint the δ^{13}C-CH_4 provides, compared to the methane mole fraction alone, is explored in Section 5.5. Finally, some of the challenges that arose with the method are discussed in Section 5.6.

5.2 Method

This section presents the method used to compare the emulator outputs and the observations. The emulators are used to predict thousands of untested input parameter combinations, which are chosen using a Sobol sequence (Sobol' 1967, Antonov & Saleev 1979) in order to get good coverage of the input parameter space (Section 4.2.2). Section 5.2.1 details the implausibility function which measures how far these emulator outputs are from the observations, and the covariance matrix used in this calculation is outlined in Section 5.2.2.

5.2.1 The implausibility function

In order to decide which emulator outputs match the observations, given the uncertainties in the system, an implausibility function is used (Craig et al. 1996, 1997). This is a probabilistic measure calculated for each emulator output. If the value is large, this suggests that this emulator output is inconsistent with observations. This implausibility function is composed of

$$I^2(\boldsymbol{x}) = (\boldsymbol{z} - E(F(\boldsymbol{x})))^T \boldsymbol{C}^{-1} (\boldsymbol{z} - E(F(\boldsymbol{x}))), \tag{5.1}$$

where I is the implausibility value, $\boldsymbol{z}$ is the observational time series, $\boldsymbol{C}$ is the error covariance matrix (which will be discussed in Section 5.2.2), and $E(F(\boldsymbol{x}))$ is the emulator output for a set of parameters $\boldsymbol{x}$. The implausibility value can then be

compared to some cut-off. Emulator outputs higher than this value are discarded as they are unlikely to be consistent with the observations, and those that are lower than this value are accepted as plausible. This implausibility function is equivalent to the cost function (Equation 1.13) of previous studies using inverse methods outlined in Section 1.6, with a uniform prior distribution.

A sum of the squares of n independent standard normal random variables, such as $I^2(\boldsymbol{x})$, is distributed as a chi-squared distribution with n degrees of freedom. Therefore, the cut-off value is chosen from the quantile function of a chi-squared distribution with the same number of degrees of freedom as there are observations (Mardia et al. 1979). This value can be chosen accordingly for the aim of the work, and in this work, the most plausible range of input parameters is investigated, so a probability content of 0.683 was chosen. This is the fraction of data points that fall within one standard deviation on a normal distribution. In this work, there are 560 observations and hence degrees of freedom (as months with missing data are excluded), and 0.683 corresponds to a value of 575 (to three significant figures) from the quantile function of a chi-squared distribution with 560 degrees of freedom. This value of 575 will be used as the cut-off value in this work.

5.2.2 The covariance matrix

In order to know if the emulator output and observations match, the uncertainty in the system must be accounted for. This is the role of the covariance matrix $\boldsymbol{C}$, which was built from three parts: the chemical transport model (CTM) invariant parameter error, the emulator error, and the model-measurement discrepancy error, each of which is described below. Since the methane mole fraction and δ^{13}C-CH_4 have very different magnitudes, the errors presented in the figures are normalised to be a fraction of the mean observed value for that observation type and hemisphere, putting the emulators on a similar scale for visualisation. Therefore, the plotted covariance matrices are for illustrative purposes only, and the covariance matrix used in the calculation of the implausibility function contains the unnormalised values.

The MOZART invariant parameter error was calculated as described in Section 2.5.2. The resulting MOZART covariance matrix is shown in Figure 5.2.1, and has several key features. The methane mole fraction quadrant stands out: the fractional error in the methane mole fractions is much larger than that in δ^{13}C-CH_4. This quadrant also shows how hemispheric covariation is very strong, and that the covariance grows with time. This is because the invariant parameters have an effect throughout the time series. For example, if a source's emissions are too high, they are too high for the whole time series, meaning that the methane mole fraction grows throughout the time series. In contrast, the off-diagonal quadrants are approximately zero, showing that there is very little correlation between the invariant parameter uncertainties in methane mole fraction and δ^{13}C-CH_4.

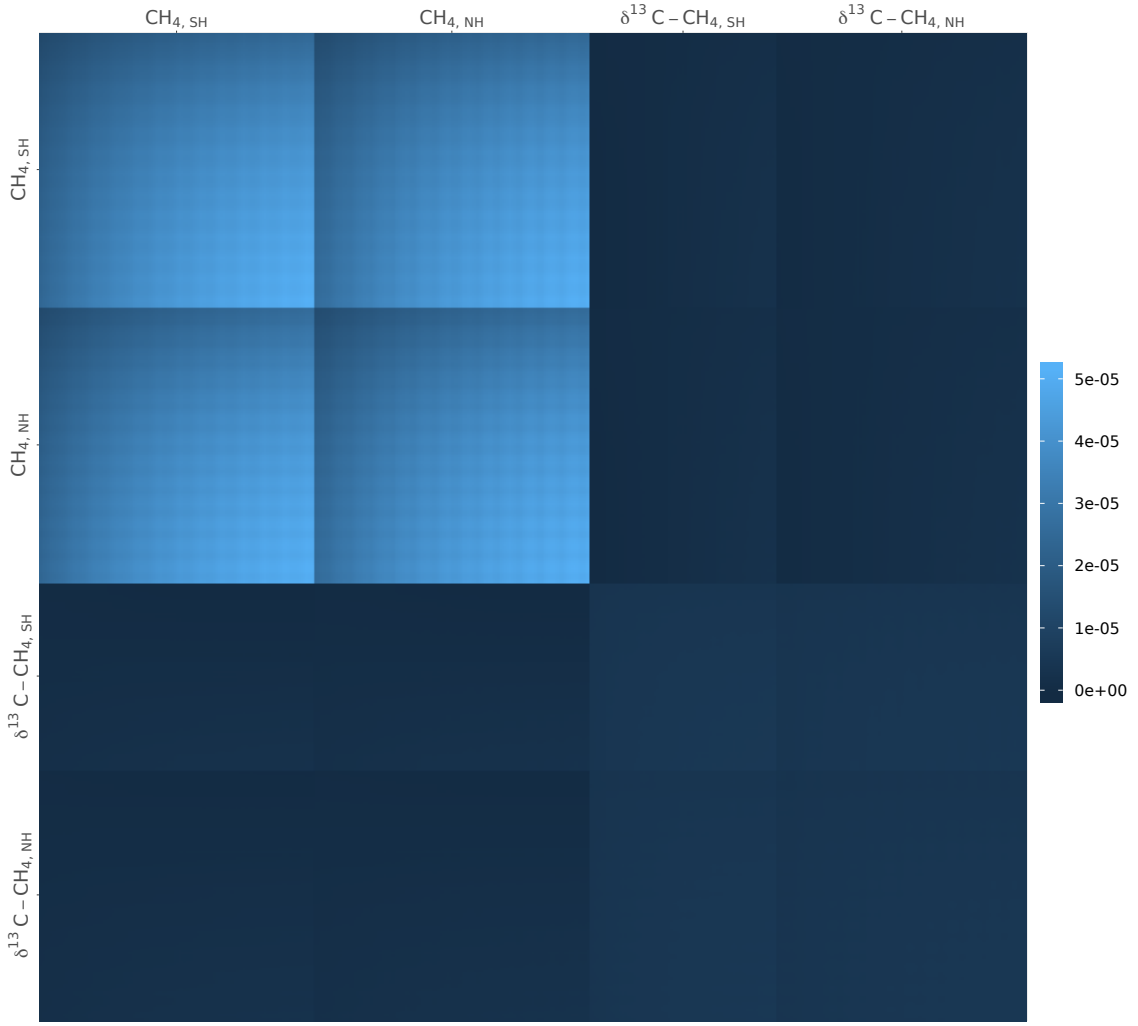

Figure 5.2.1: A visualisation of the covariance matrix of the MOZART invariant parameter error. Each hemispheric methane mole fraction and δ^{13}C-CH_4 square shows the time series with missing observations removed, and the values plotted are a fraction of the mean observed value. The axis labels are limited for clarity, e.g. the y-axis could be further labelled $CH_{4,\,SH}$ month 1 in the top corner, down to δ^{13}C-$CH_{4,\,NH}$ month 156 in the bottom corner.

The emulator error covariance matrix is calculated for each emulator simulation, as in Equation 1.17, because the accuracy of the emulator prediction depends on how close the input parameters are to the input parameters of the training dataset, as demonstrated in Section 1.8.1. This means that the emulator error in each hemisphere is constant throughout the time series, as each time point has the same inputs and so they are the same distance from the training dataset. The emulators were

built independently, so their errors form a block diagonal in the covariance matrix, which is shown in Figure 5.2.2 for the mean covariance matrix of the 90 simulations in the validation dataset. From this figure, the δ^{13}C-CH_4 emulators can be seen to have a larger relative error than the methane mole fraction emulators.

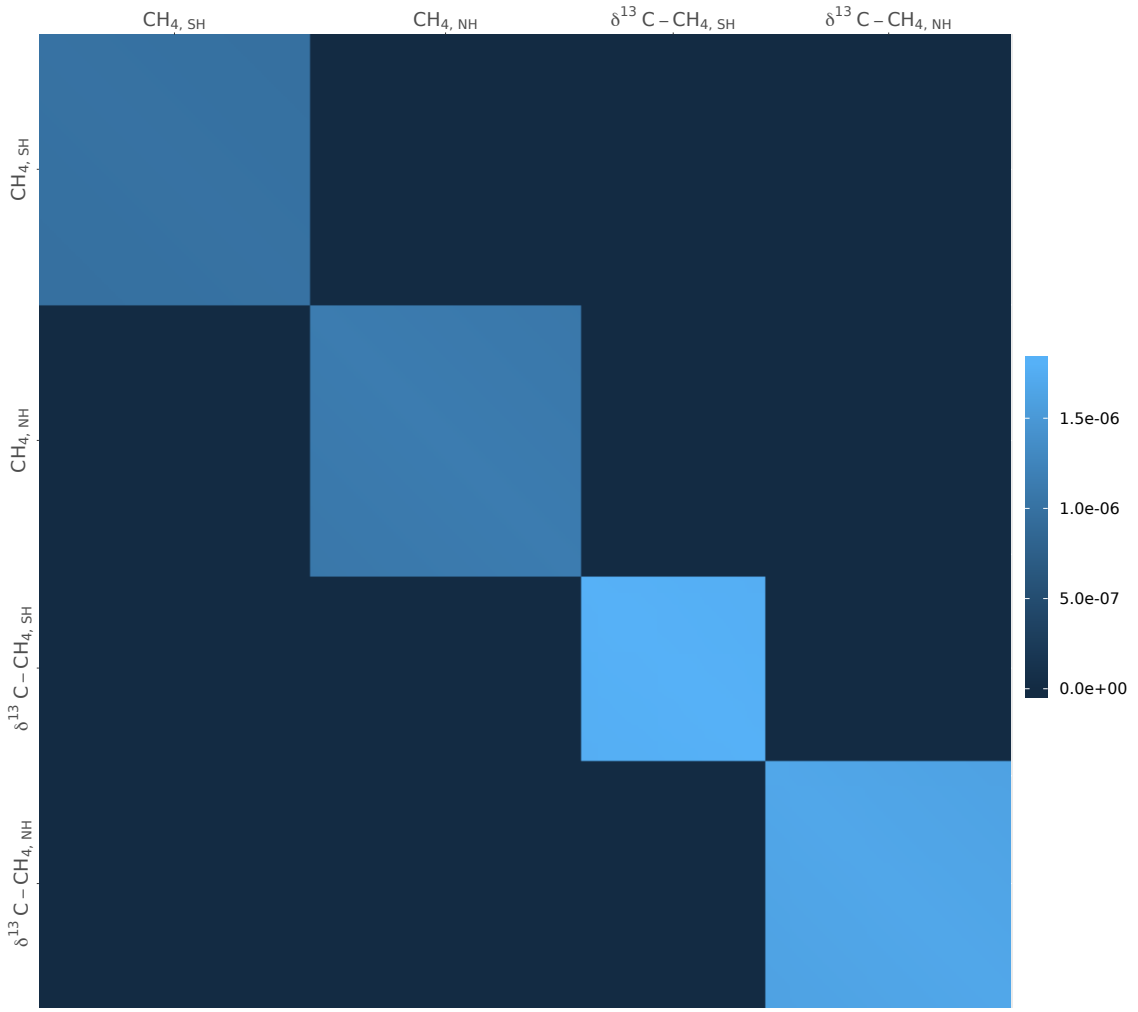

Figure 5.2.2: A visualisation of the mean emulator error covariance matrix for the validation dataset simulations. Each hemispheric methane mole fraction and δ^{13}C-CH_4 square shows the time series with missing observations removed, and the values are presented as a fraction of the mean observed value. The axis labels are limited for clarity, e.g. the y-axis could be further labelled $CH_{4,\,SH}$ month 1 in the top corner, down to δ^{13}C-$CH_{4,\,NH}$ month 156 in the bottom corner.

The model-measurement discrepancy error is calculated as in Section 2.5.2. The

covariance matrix is diagonal, which is shown in Figure 5.2.3. The fractional errors are much larger for the methane mole fraction, in particular for the northern hemisphere with its much higher emissions.

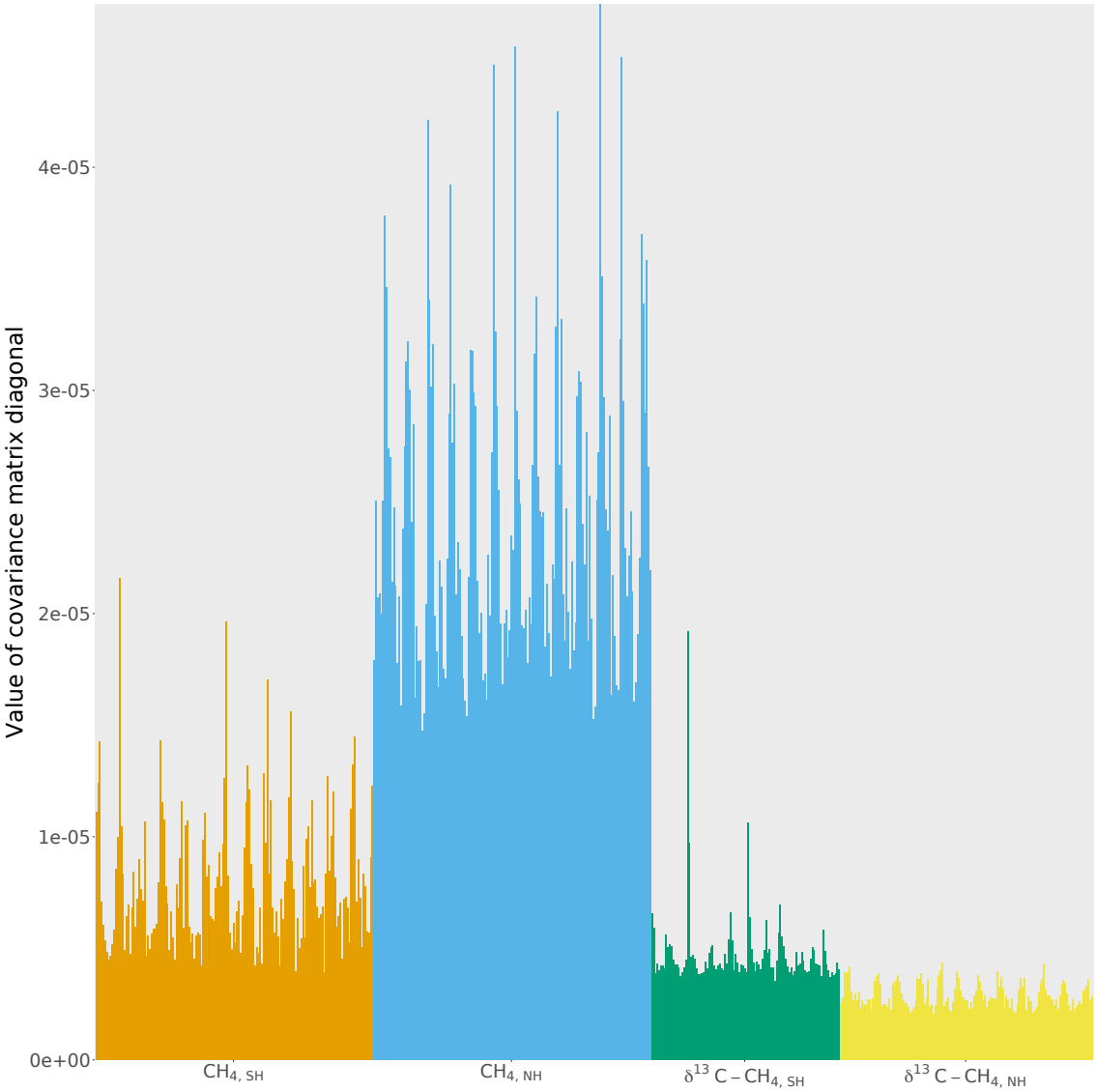

Figure 5.2.3: A visualisation of the diagonal of the model-measurement discrepancy error covariance matrix. The missing observations have been removed, and the values are presented as a fraction of the mean observed value.

The three uncertainty covariance matrices (MOZART invariant parameter ($\boldsymbol{C}_{\text{mzt}}$), emulator ($\boldsymbol{C}_{\text{em}}$), and model-measurement discrepancy ($\boldsymbol{C}_{\text{obs}}$)) are summed to produce the total covariance matrix ($\boldsymbol{C}$):

$$\boldsymbol{C} = \boldsymbol{C}_{\text{mzt}} + \boldsymbol{C}_{\text{em}} + \boldsymbol{C}_{\text{obs}}. \tag{5.2}$$

The total covariance matrix is shown in Figure 5.2.4. On the diagonal, the model-measurement discrepancy error and the MOZART invariant parameter error dominate, with the emulator error making the smallest contribution for both methane mole fraction and δ^{13}C-CH_4. The off-diagonal elements are smaller than the diagonals, and are dominated by the MOZART invariant parameter error.

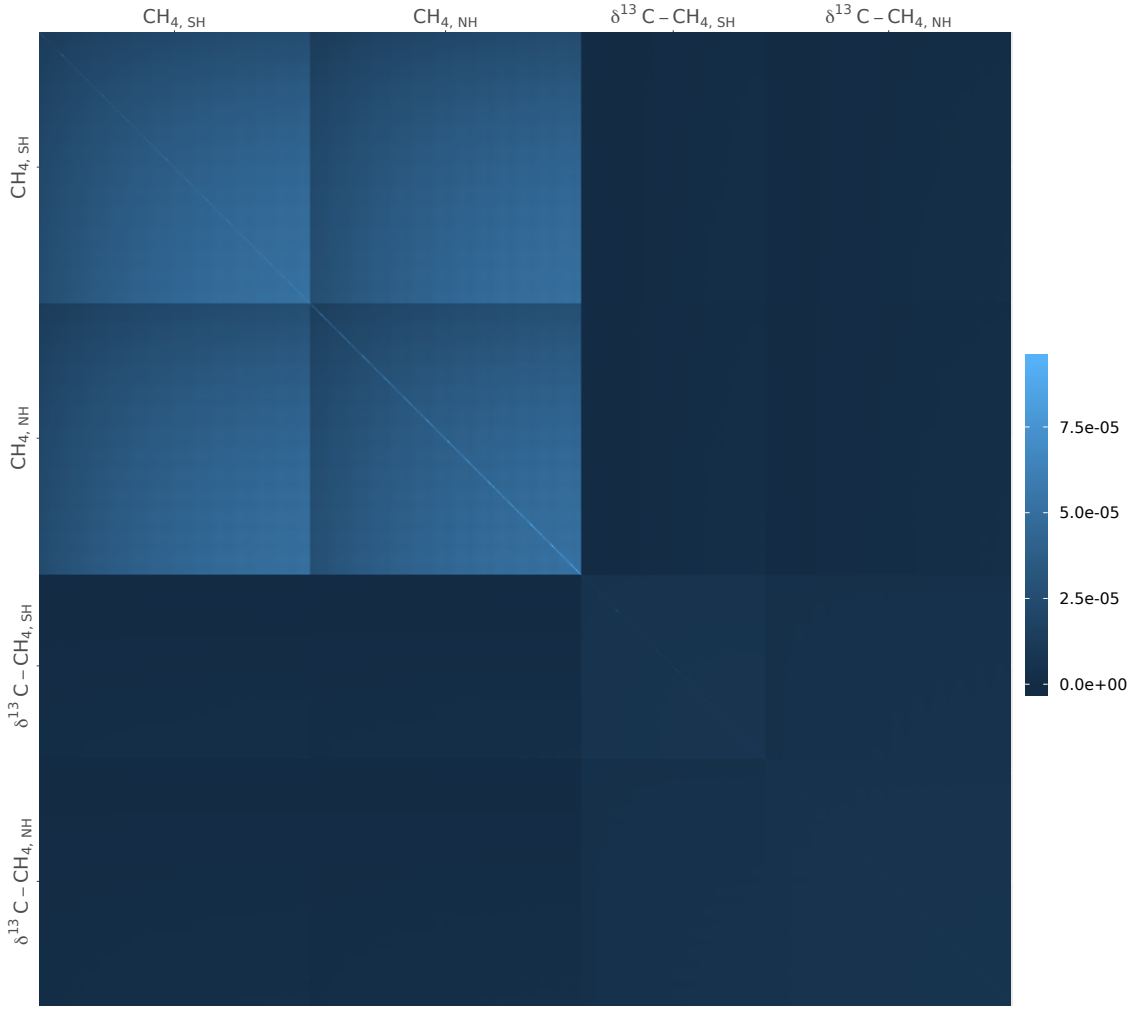

Figure 5.2.4: A visualisation of the total covariance matrix. Each hemispheric methane mole fraction and δ^{13}C-CH_4 square shows the time series with missing observations removed, and the values are presented as a fraction of the mean observed value. The axis labels are limited for clarity, e.g. the y-axis could be further labelled $CH_{4,\ SH}$ month 1 in the top corner, down to δ^{13}C-$CH_{4,\ NH}$ month 156 in the bottom corner.

5.3 The agreement between the emulator outputs and the observations

In this section, the emulators are used to predict the MOZART outputs for many untested input parameter combinations. These emulator outputs are compared to the observations using the implausibility function (Equation 5.1), and either accepted or rejected based on the cut-off value as outlined in Section 5.2.1. Two measures of implausibility are used: only the diagonal of the covariance matrix (univariate) and the full covariance matrix in Section 5.2.2 (multivariate). Two different covariance matrices are tested because of the highly correlated MOZART invariant parameter error included in this study. Previous studies do not consider the invariant parameter error and so their results would be more similar to the univariate comparison, whereas, if this error is included, the multivariate comparison should be more accurate. The range of accepted emulator outputs using these two covariance matrices are examined and compared here.

5.3.1 Univariate comparison

For the univariate measure of implausibility, the covariance matrix used is the diagonal of Figure 5.2.4, so each observation is treated as independent. While this may seem extreme, given the substantial off-diagonal elements presented in Section 5.2.2, this diagonal covariance matrix is inline with previous studies. The covariance matrix used in previous work is often diagonal (e.g McNorton et al. (2018)), and where the off-diagonal elements are non-zero, they are small compared to this work (e.g. Rigby et al. (2017)) as they do not consider the model's highly correlated invariant parameter error. Therefore, previous studies are, in general, more inline with the univariate comparison which only uses the diagonal of the covariance matrix. The comparison of the multivariate and univariate implausibility functions demonstrates the influence of the systematic model uncertainties that have been left out of previous studies.

A Sobol sequence of 2 800 000 parameter combinations was input to the emulators

to generate MOZART outputs to be compared to the observations. From these 2 800 000 simulations, only 171 (0.006 %) had an implausibility value less than the cut-off value and were accepted as consistent with the observations. These accepted simulations are plotted in Figure 5.3.1, and a summary of the accepted univariate values is presented in Figure 5.3.2.

In Figure 5.3.2, the average MOZART model inter-hemispheric difference deviates from the observed value: generally the methane mole fraction in the northern hemisphere is too high, whereas δ^{13}C-CH_4 is too low. As the input parameters were chosen to cover the input parameter space, these distributions are a modified version of the values present in the MOZART training dataset (Figure 2.4.2). The most extreme values have been removed, and the skew on the inter-hemispheric difference remains, as a result of the bias in the MOZART training dataset.

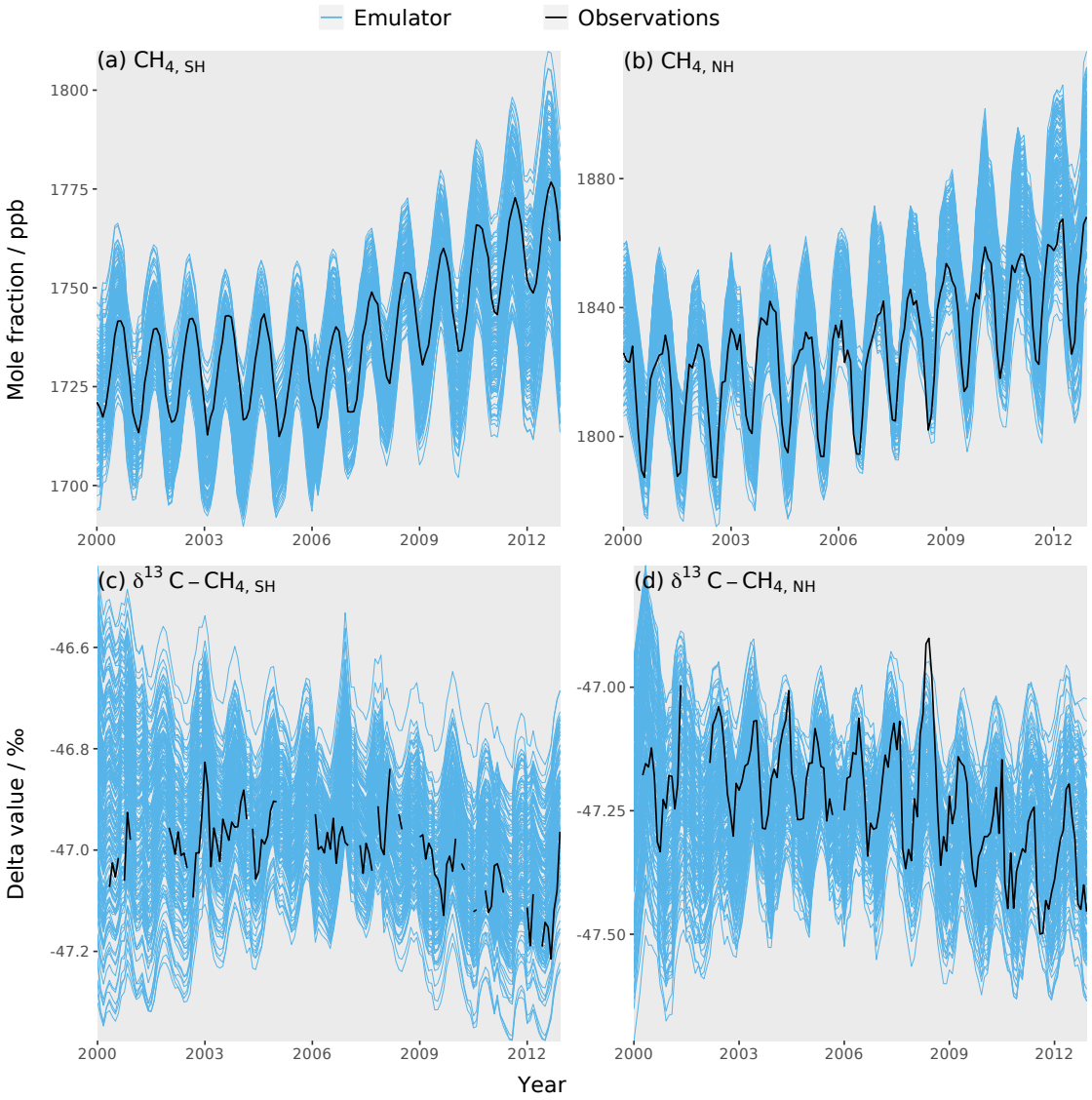

Figure 5.3.1: The accepted emulator outputs using the univariate implausibility value (blue lines) compared to the observations (black line). The panels show the four methane observations: (a) the methane mole fraction in the southern hemisphere, (b) the methane mole fraction in the northern hemisphere, (c) δ^{13}C-CH_4 in the southern hemisphere, and (d) δ^{13}C-CH_4 in the northern hemisphere.

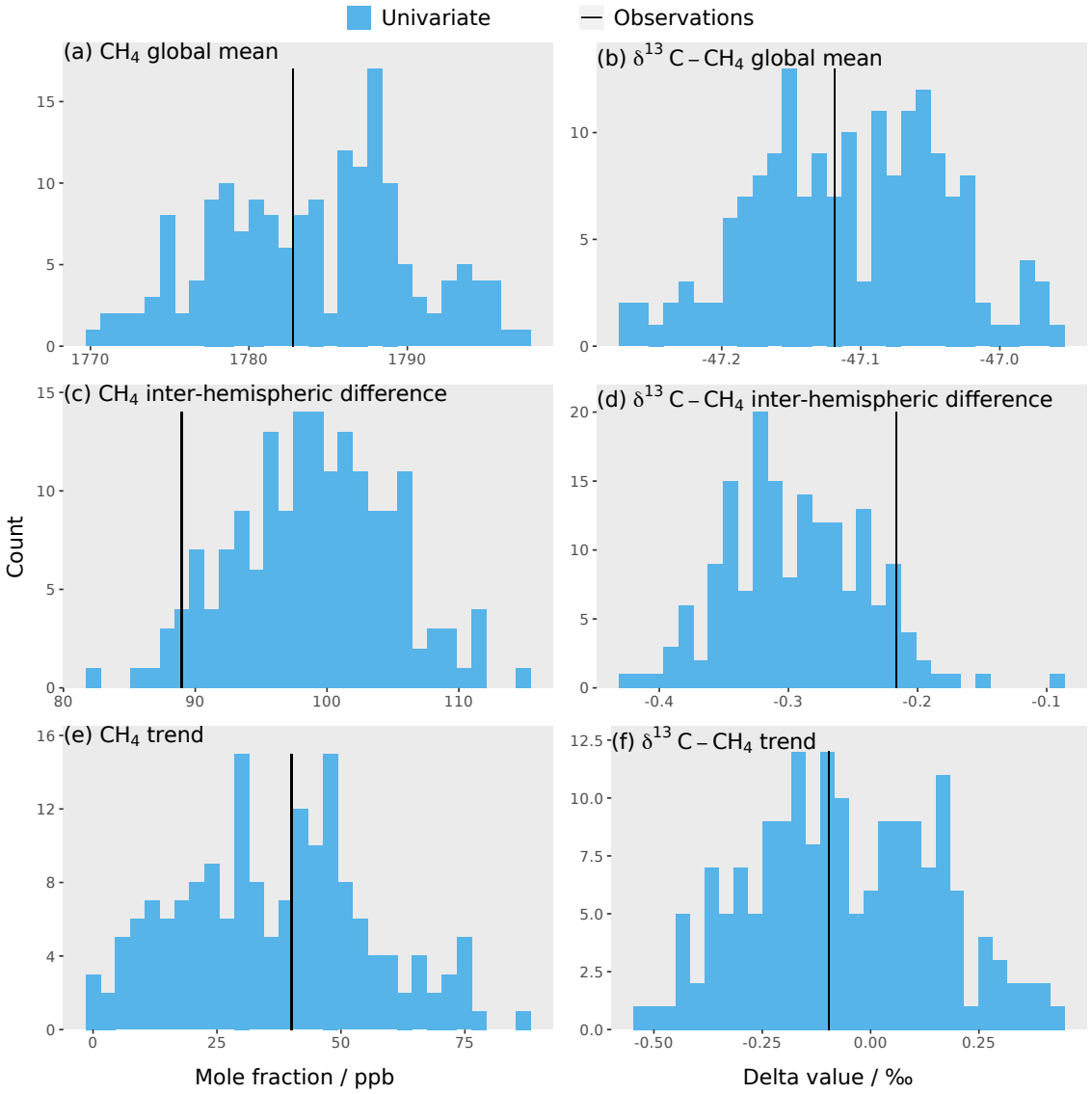

Figure 5.3.2: Histograms of the accepted simulations using the univariate implausibility function for six outputs: (a) methane mole fraction global mean, (b) δ^{13}C-CH_4 global mean, (c) methane mole fraction inter-hemispheric difference, (d) δ^{13}C-CH_4 inter-hemispheric difference, (e) methane mole fraction trend, and (f) δ^{13}C-CH_4 trend. The black line represents the corresponding value for the observations. The calculation of these values is described in Section 2.4.3.

5.3.2 Multivariate comparison

For the multivariate implausibility function, the full covariance matrix is used to match the observations and emulator outputs. However, the acceptance rate of simulations was so low that a history matching approach (Section 1.8.3) was taken. This meant using four stages to compare the emulator outputs and observations.

In the first stage, the emulators predicted the MOZART output of 2 800 000 input parameter combinations, and simulations with an implausibility value less than 738 (five standard deviations in a normal distribution) were accepted. The range of input parameter values of these accepted simulations was used for the next stage. Unlike Vernon et al. (2010), the same emulators were used for each stage because the emulator error is a small contribution to the total error and creating a new training dataset is computationally expensive. The details of the four stages are given in Table 5.1, and the accepted simulations of the final wave are analysed in this thesis. The number of simulations in each wave was chosen so that at least 100 simulations were accepted, so these reduced parameter ranges may not extend to the extremes of their true ranges. However, even with the fast Gaussian process emulators, this number of simulations was computationally expensive. In future, the emulators could be used with an algorithm that can more efficiently sample the parameter space, such as Markov Chain Monte Carlo (e.g. Rigby et al. (2017)). However, this is beyond the scope of this work.

Stage	Number of simulations	Cut-off value	Number of accepted simulations
1	2 800 000	738	143
2	2 800 000	656	139
3	6 160 000	618	104
4	55 832 000	575	114

Table 5.1: Details of the four stages used to zone in on methane simulations that are consistent with the observations. The cut-off values are given to three significant figures.

The 55 832 000 simulations in the fourth stage were compared to observations, and the 114 (0.0002 %) that were accepted are plotted in Figure 5.3.3, alongside those accepted using the univariate implausibility function for comparison. A summary of the global mean, inter-hemispheric difference, and trend compared to observations is presented in Figure 5.3.4. The comparison of accepted outputs for the multivariate and univariate cases in Figure 5.3.3 demonstrates the large difference that the

off-diagonal elements (predominantly from the MOZART invariant parameter error) make. These off-diagonal elements significantly increase the range of the methane outputs that are statistically consistent with the observations. However, they also significantly decrease the percentage of accepted simulations. This decrease is because the differences between the simulations and the observations must be highly correlated in the multivariate case, so a simulation that is consistently 20 ppb higher than observations is more plausible than a simulation that varies from 10 ppb lower than observations to 10 ppb higher. These changes will affect the level of constraint that the observations provide on the methane budget, which is explored in Section 5.4.

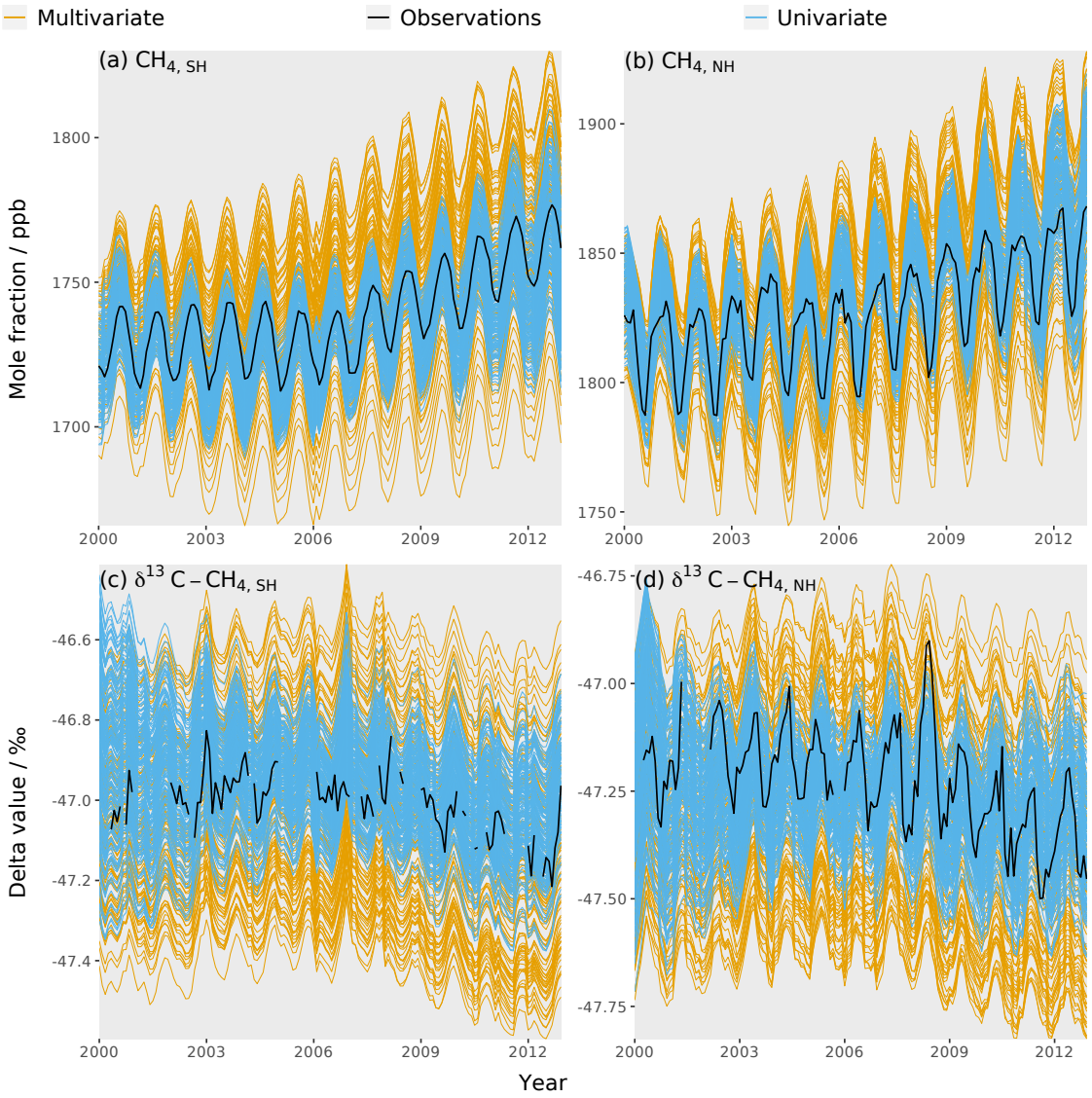

Figure 5.3.3: The accepted hemispheric emulator outputs using the multivariate implausibility value (orange lines) compared to the univariate implausibility value (blue lines), and the the observations (black line). The panels show the four methane observations: (a) the methane mole fraction in the southern hemisphere, (b) the methane mole fraction in the northern hemisphere, (c) δ^{13}C-CH_4 in the southern hemisphere, and (d) δ^{13}C-CH_4 in the northern hemisphere.

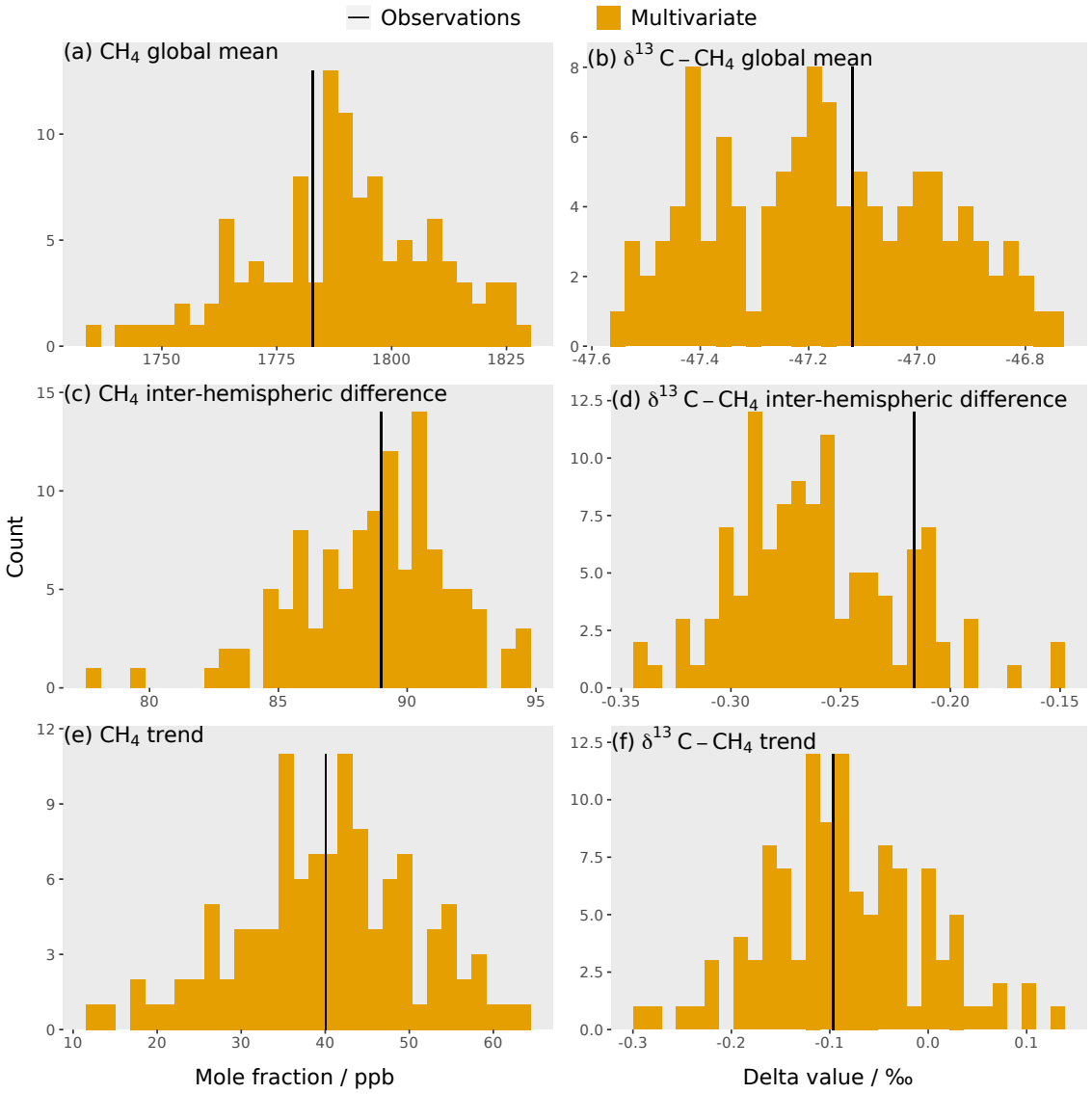

Figure 5.3.4: Histograms of the accepted simulations using the multivariate implausibility function for six outputs: (a) methane mole fraction global mean, (b) δ^{13}C-CH_4 global mean, (c) methane mole fraction inter-hemispheric difference, (d) δ^{13}C-CH_4 inter-hemispheric difference, (e) methane mole fraction trend, and (f) δ^{13}C-CH_4 trend. The black line represents the corresponding value for the observations. The calculation of these values is described in Section 2.4.3.

5.4 Methane sources and sinks consistent with observations

The inputs of the accepted emulator simulations from the previous section are examined here. The aim is to constrain the range of plausible input parameters, which

are the magnitudes, δ^{13}C-CH_4 signatures, and trends of the sources and sinks of methane.

5.4.1 Univariate comparison

Figure 5.4.1 shows the density of the possible values of the parameters for the accepted simulations using the univariate implausibility function. Many parameters in this figure have a close to uniform distribution, meaning that no constraint has been gained by examining only simulations consistent with the observations. However, some parameters have been constrained as they have regions of parameter space that can be considered inconsistent with observations. There is a gain in constraint for the freshwater source magnitude (54 to 173 $Tg\,yr^{-1}$), the OH loss magnitude (417 to 623 $Tg\,yr^{-1}$), the OH loss trend (-12 to +20 %), and the initial δ^{13}C-CH_4 (-57.7 to -52.6 ‰). These ranges correspond to 68.3 % uncertainty intervals as a probability content of 0.683 was used for the cut-off value (Section 5.2). Qualitatively, these results suggest that OH concentrations are unlikely to be substantially higher than the initial mean estimate and that a large negative trend during this period is unlikely, as shown in Figure 5.4.1. Freshwater emissions are more likely to be toward the lower end of the current uncertainty range (Saunois et al. 2016). It is not surprising that these parameters are the most constrained, given the high sensitivity of methane observations to them (Chapter 4). The finding that only three of the key unknowns in the global methane budget were substantially constrained demonstrates our inability to make strong inferences about drivers of change in atmospheric methane, at least when only hemispheric average observations of methane mole fraction and δ^{13}C-CH_4 are used.

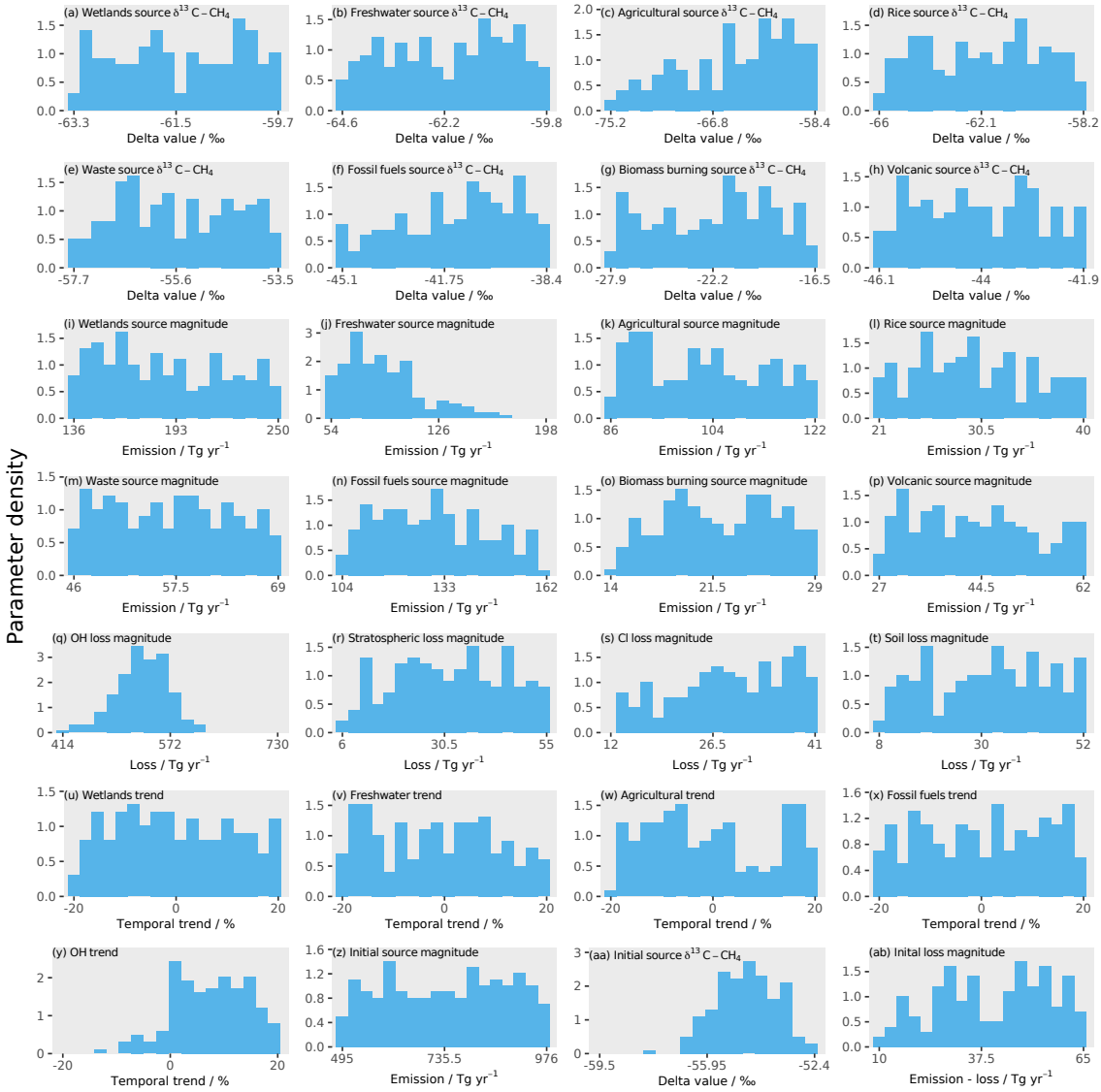

Figure 5.4.1: The density of input parameter values in the accepted emulator simulations using the univariate implausibility value, with each parameter shown in a separate panel.

5.4.2 Multivariate comparison

Figure 5.4.2 shows the density of the possible values of the parameters for the multivariate implausibility function compared to the univariate case. The multivariate implausibility function constrains the sources and sinks of methane further than the univariate implausibility function, as discussed in Section 5.3.2. Three parameters that were constrained by the univariate implausibility function have been significantly further constrained: the freshwater source magnitude (55 to 90 Tg yr^{-1}), the

OH loss magnitude (434 to 528 $Tg\,yr^{-1}$), and the OH loss trend (+0.5 to +16 %). The fourth parameter constrained by the univariate implausibility function, the initial $\delta^{13}C\text{-}CH_4$, is constrained over a similar range to the univariate implausibility function (-56.2 to -53.2 ‰). Several additional parameters have had their ranges constrained: the agricultural source $\delta^{13}C\text{-}CH_4$ (-72.8 to -58.7 ‰), the wetlands source magnitude (139 to 204 $Tg\,yr^{-1}$), the agricultural source magnitude (86 to 115 $Tg\,yr^{-1}$), the fossil fuels source magnitude (104 to 137 $Tg\,yr^{-1}$), the wetlands trend (-11 to 20 %), and the initial loss magnitude (28 to 62 $Tg\,yr^{-1}$). These ranges are still large, demonstrating how poorly constrained the methane budget is, though they are better constrained than when using the univariate implausibility function. Therefore, by ignoring the highly correlated invariant parameter error, previous studies have been missing significant constraint on the methane budget.

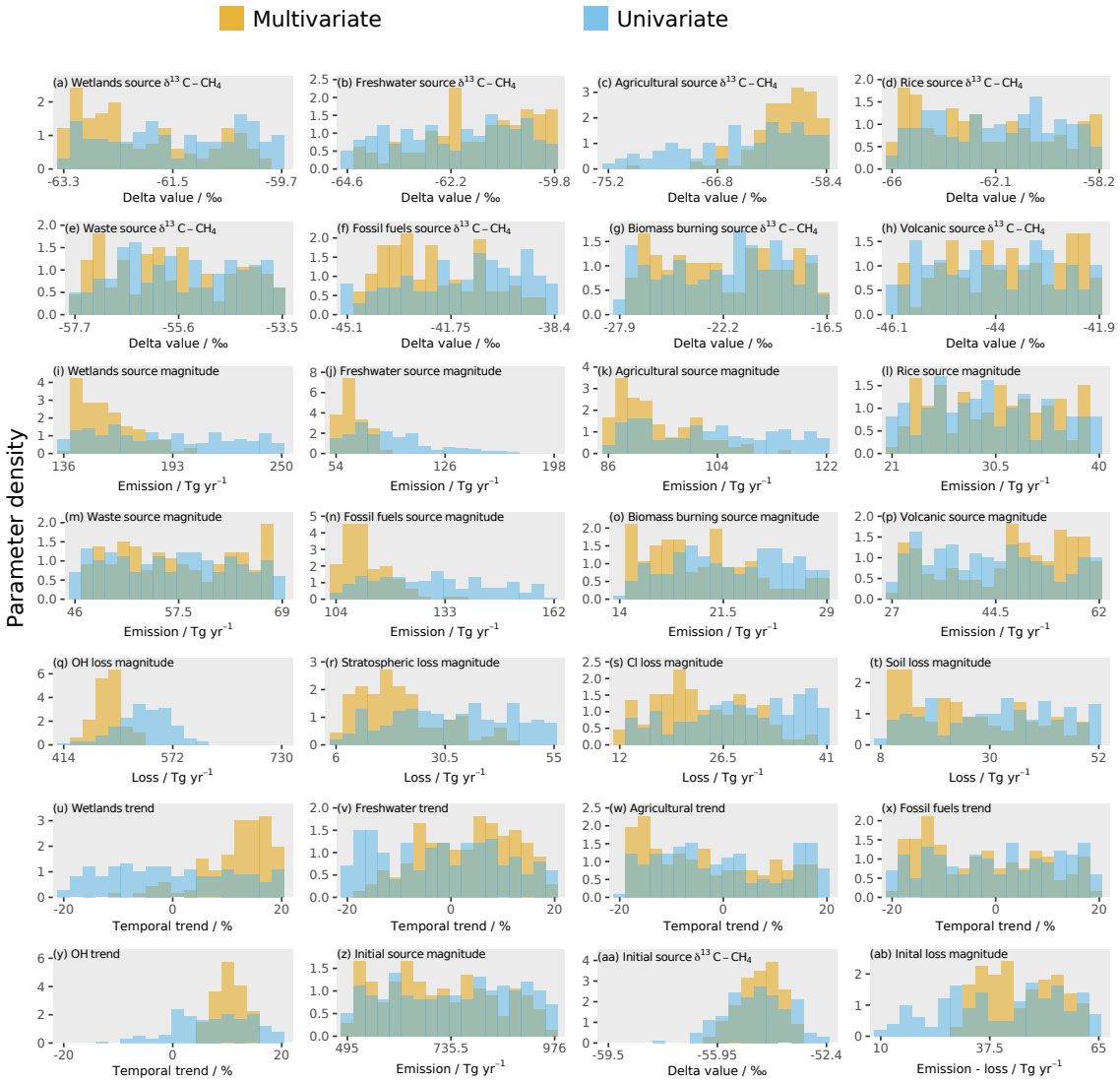

Figure 5.4.2: The density of input parameter values in the accepted emulator simulations using the multivariate implausibility value (orange) compared to the univariate implausibility value (blue), with each parameter shown in a separate panel.

5.4.3 Most probable parameter values

To find an optimal set of parameter values, as in previous studies, a Bayesian inversion should be performed. Whilst this is beyond the scope of this thesis, we can examine the most likely parameter values from the distributions found in this chapter. The median parameter values using the univariate and multivariate implausibility functions are compared to the initial parameter values and shown in Figure 5.4.3. In general, there is little change from the initial value, with little

reduction in its uncertainty range. The parameters that were shown to have been constrained in Section 5.4.2 do show changes in their most likely value. For the multivariate implausibility function, the median value has become -61.2 ‰ for the agricultural source δ^{13}C-CH_4, 154 $Tg\,yr^{-1}$ for the wetlands source magnitude, 63 $Tg\,yr^{-1}$ for the freshwater source magnitude, 92 $Tg\,yr^{-1}$ for the agricultural source magnitude, 110 $Tg\,yr^{-1}$ for the fossil fuels source magnitude, 479 $Tg\,yr^{-1}$ for the OH sink magnitude, +13 % for the wetlands temporal trend, +10 % for the OH temporal trend, -54.5 ‰ for the initial source δ^{13}C-CH_4, and 44 $Tg\,yr^{-1}$ for the initial loss magnitude.

These median parameter values show two significant changes in the parameter trends. The largest constraint is for the OH sink, which increases over the time series and this decreases the methane mole fraction. The second constraint is for the wetlands source, which is likely to have increased over the time series. Therefore, the methane mole fraction rise observed since 2007 for this median solution is explained by the emission inventories' trends (damped by the OH increase) which are shown in Figure 2.2.2, but with a larger contribution from the wetland emissions. This shows that fossil fuels, agriculture, waste, and wetlands all contribute to this positive trend in methane mole fraction. However, the large uncertainties mean that this is just one of many likely possibilities.

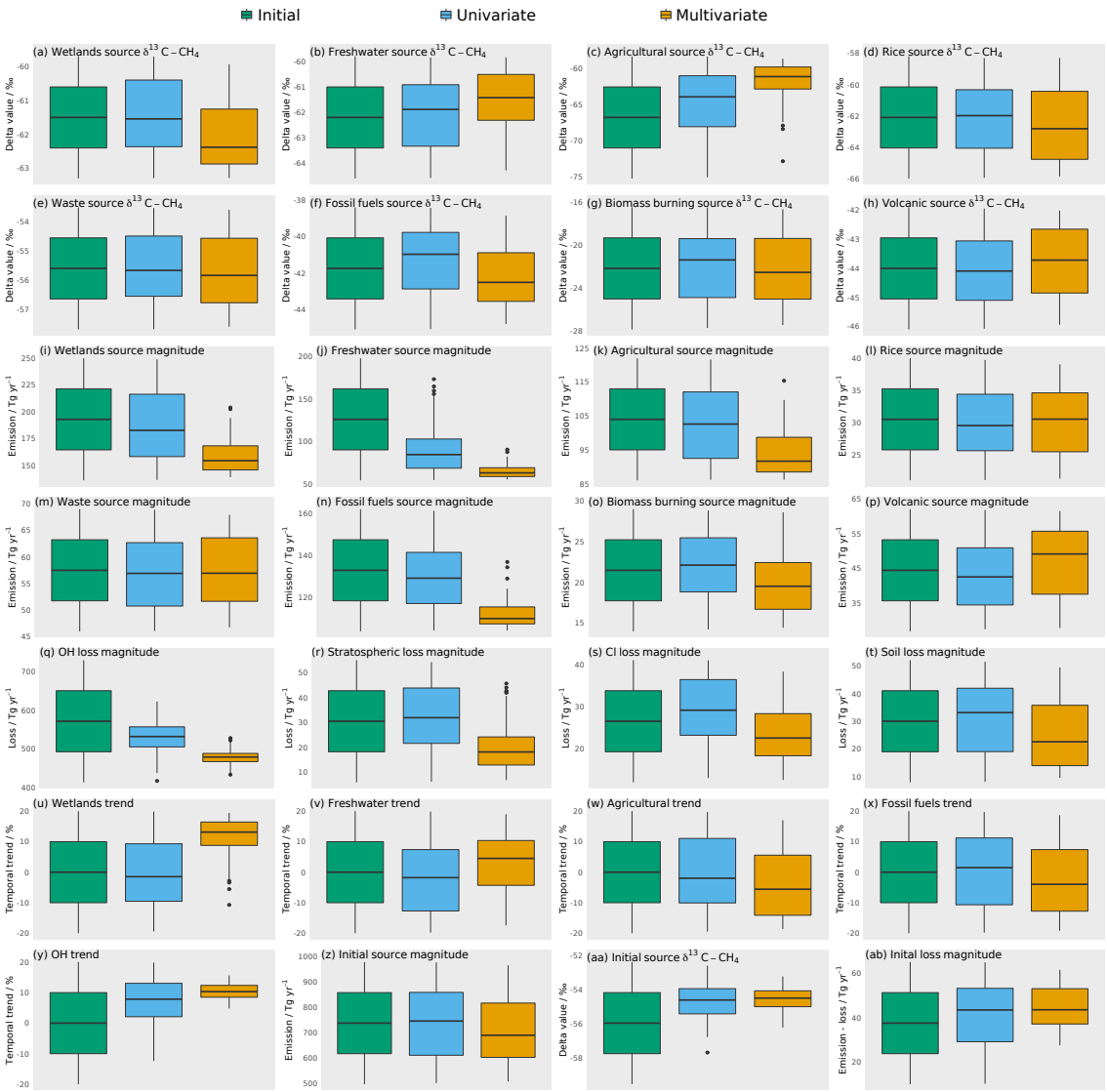

Figure 5.4.3: Boxplots showing the most likely parameter values for each parameter in a separate panel using the univariate implausibility function (blue) and using the multivariate implausibility function (orange) compared to the initial values (green). Black dots represent outliers, though the small number of accepted simulations means these are unlikely to be outliers if more samples were taken. The vertical black line represents the range of the parameter values (excluding outliers), and the horizontal black lines represent the 0.25, 0.50, and 0.75 quantiles.

5.4.4 Parameter correlation

While there are few constraints on the total input parameter space, there are correlations between the possible input parameters, which are shown in Figure 5.4.4. Parameters with the strongest correlations (or anti-correlations) would be useful

to reduce the uncertainty in, because they would also reduce the possible range of their highly correlated (or anti-correlated) parameters. For example, if the OH loss is high, then the sources have to be high in order to match the observed methane mole fraction. This is particularly true for the largest sources: wetlands, fresh water, and fossil fuels. The δ^{13}C-CH_4 initial condition is also correlated with several parameters in order to match the observed δ^{13}C-CH_4: there is a strong anti-correlation with the Cl loss and correlation with the agricultural source δ^{13}C-CH_4. These parameters are also those which were shown to be most important in the sensitivity analysis in Chapter 4.

However, most of the parameters in Figure 5.4.4 are not correlated. This shows how under-constrained the problem is: even if the uncertainty of one parameter is reduced to zero, most of the other parameters would not be further constrained.

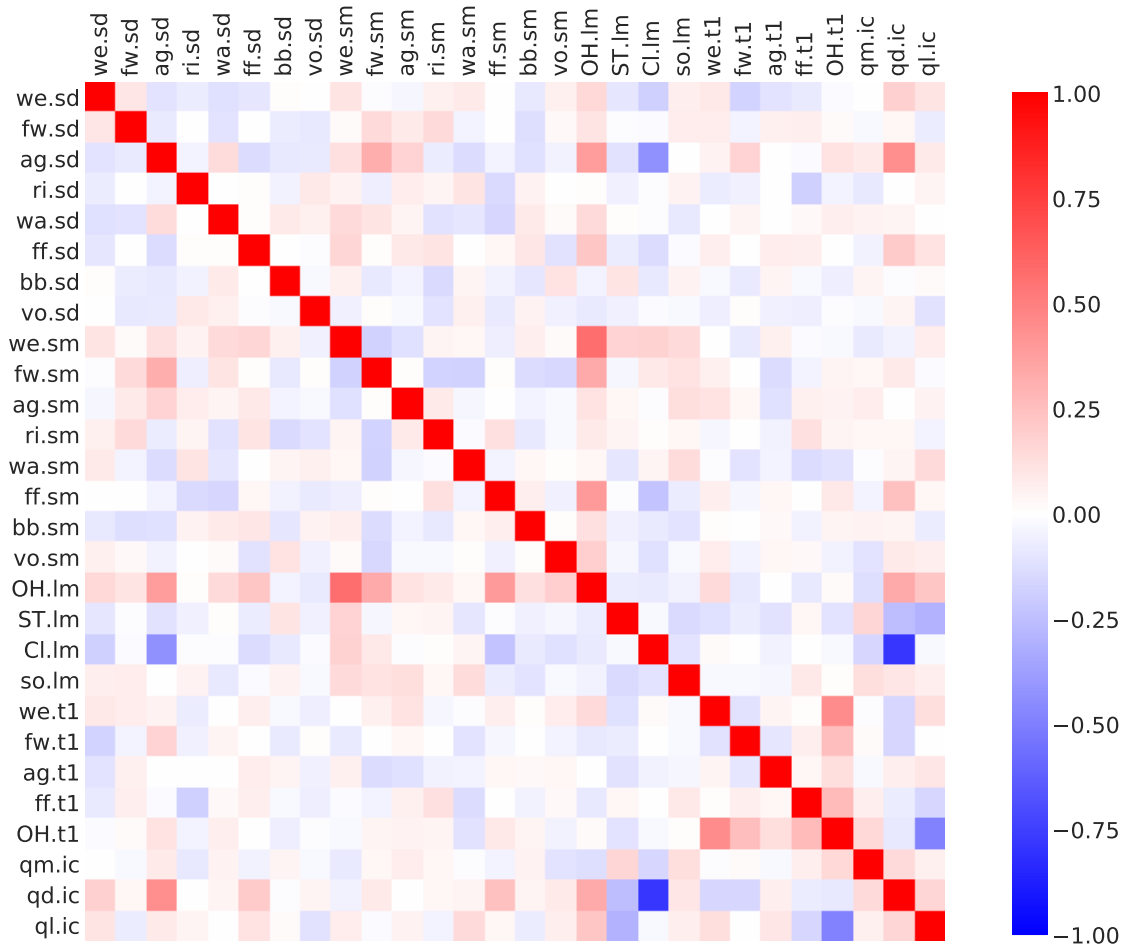

Figure 5.4.4: The correlation between the input parameters for the accepted simulations using the univariate implausibility function. Using the multivariate implausibility function looks similar, but noisier due to the low number of accepted simulations. The input parameter codes are given by a combination of a two character code giving the source or loss, (wetlands (we), fresh water (fw), agriculture (ag), rice (ri), waste (wa), fossil fuels (ff), biomass burning (bb), volcanoes (vo), hydroxyl radical (OH), stratospheric (ST), Cl radical (Cl), soil (so), total source magnitude (qm), total source δ^{13}C-CH_4 (qd), total loss imbalance (ql)) and another code giving the type of parameter, (source δ^{13}C-CH_4 (sd), source magnitude (sm), loss magnitude (lm), temporal trend (t1), initial condition (ic)).

5.5 How much constraint is due to the isotopic data?

δ^{13}C-CH_4 observations are increasingly being incorporated into methane modelling studies, so the information added by this measurement was investigated. When just

the methane mole fraction emulator simulations were compared to observations using the multivariate implausibility function during the fourth stage (Section 5.3.2), 21 352 out of 55 832 000 simulations (0.04 %) were accepted, compared to 234 887 (0.4 %) for the δ^{13}C-CH_4 emulator simulations. The δ^{13}C-CH_4 is less selective than the methane mole fraction because there is a smaller range of possible MOZART δ^{13}C-CH_4 outputs relative to the error used to match to observations. The range of the temporal mean methane mole fraction in the MOZART training data is 1085 and 1132 ppb for the southern and northern hemispheres, respectively. This is 93 and 79 times the median standard deviation in the covariance matrix used in the implausibility function. Whereas, for the δ^{13}C-CH_4, the range of the temporal mean in the MOZART training data is 7.4 and 7.3 ‰ for the southern and northern hemispheres, respectively, which is 48 and 52 times the median standard deviation. Therefore, the δ^{13}C-CH_4 is not necessarily providing less constraint than the methane mole fraction, it just has a smaller range of outputs relative to its error.

It is more informative to look at which inputs have been constrained. Using the fourth stage input parameter ranges (Section 5.3.2), the first 280 000 emulator simulations from the Sobol sequence were matched to just the methane mole fraction observations using the multivariate implausibility function, and the accepted inputs are compared to the results using the combined observations in Figure 5.5.1. The wetlands trend is further constrained using the combined methane mole fraction and δ^{13}C-CH_4 data, along with the δ^{13}C-CH_4 initial condition, and the agricultural source δ^{13}C-CH_4. Although the latter two of these parameters were introduced for the use of δ^{13}C-CH_4, so do not inform us about the methane budget. Therefore, little extra constraint is gained from the δ^{13}C-CH_4 in this study, calling its value into question.

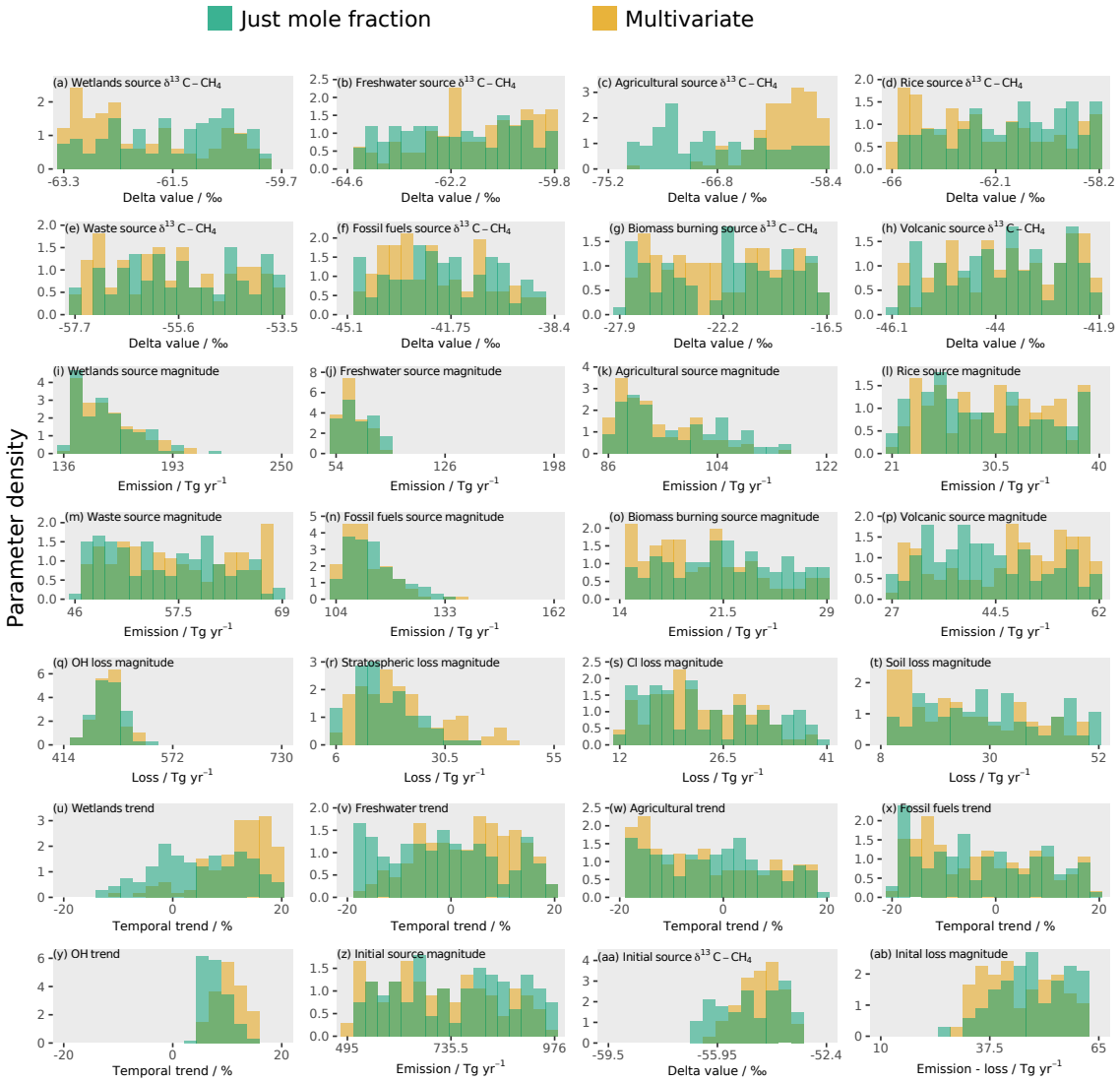

Figure 5.5.1: The density of input parameter values in the accepted emulator simulations with the multivariate implausibility function, using both methane mole fraction and δ^{13}C-CH_4 (orange), and using the methane mole fraction alone (green), with each parameter shown in a separate panel.

5.6 The issues with spatially fixed emissions inventories and loss fields

One of the biggest issues in this work, is that the emissions inventories and loss fields did not have their spatial (and temporal, apart from the five largest terms for which a simple linear trend was investigated) distributions vary from that of the inventory

or model used. The fixed spatial distribution issue became apparent with the bias in the inter-hemispheric difference of the MOZART training dataset (Figure 2.4.2). However, for the larger terms in the methane budget, even a small uncertainty in the spatial distribution could result in a significant change to the methane inter-hemispheric difference. For example, the OH concentration is assumed to be nearly equal between the hemispheres (Spivakovsky et al. 2000), but Patra et al. (2014) suggest a ratio of the northern to southern hemispheres of 0.97 ± 0.12, which would create a substantially larger range of methane inter-hemispheric differences if this range was parameterised.

The fixed temporal trend issue first arose when trying to match the observations with the temporal trends in the emission inventories, but without the temporal trend parameters: it was impossible to match the observations as the temporal trend in MOZART was always too high. By far the largest trend in inventories is the EDGAR fossil fuel emissions inventory (Figure 2.2.2), so this is a likely culprit given that previous authors have also questioned this trend (e.g. Monteil et al. (2011)). Alternatively, Stevenson et al. (2020) suggest that OH has a large positive trend over this period, but an OH climatology was used in this work, so there is no trend in OH without the temporal trend parameter. Temporal trend parameters were added, and the OH loss trend tends to be positive (Section 5.4.2), either to counteract the high emissions trend or because OH concentration is increasing, contrary to some other modelling studies, which used methyl chloroform observations, and suggested a negative (but highly uncertain) trend in OH loss for at least part of the period examined (Rigby et al. 2017, Turner et al. 2017). Rigby et al. (2017) suggested a higher order (non-linear) trend in OH loss, which this study cannot reproduce as only linear trends were considered.

In order to allow the spatial distributions and temporal trends of the sources and losses to vary, more input parameters would have to be used (e.g. controlling the relative northern versus southern emissions magnitude for some source). The more input parameters, the more training data (and hence MOZART simulations) are required. This means the problem would quickly become too time consuming to

generate training data for. This work is already approaching the usual maximum number of parameters for the Gaussian process, and, although other machine learning techniques may overcome this limit, the issue of the time taken to generate the required training data would remain. Therefore, if spatial variation was going to be parameterised, other parameters would have to be removed, for example, the different source types. Ways to minimise the number of parameters are further discussed in Chapter 6. Though perhaps the same setup used in this work with different bottom-up emission and sink estimates could be created, and the different results compared. The better the fit of the emulator outputs to the observations (the higher the acceptance rate) the more consistent that combination of bottom-up emissions is with the observations.

5.7 Conclusions

In this chapter, the comparison of MOZART outputs and observations to find the input parameter values consistent with observations required millions of simulations, which was only made feasible by use of the fast emulators. The results confirm that the methane budget is under-constrained, at least when hemispheric mean methane mole fraction and δ^{13}C-CH_4 observations were used. Only 10 out of 28 parameters had their possible ranges substantially reduced: the freshwater source magnitude, the OH loss magnitude, the OH loss trend, the δ^{13}C-CH_4 source initial condition, the agricultural source δ^{13}C-CH_4, the wetlands source magnitude, the agricultural source magnitude, the fossil fuels source magnitude, the wetlands trend, and the initial loss magnitude. When only the diagonal of the covariance matrix that describes the errors in the measurements, the model, and the emulators was used to match simulations and observations (the univariate implausibility comparison), only the freshwater source magnitude, the OH loss magnitude, the OH loss trend, and the δ^{13}C-CH_4 source initial condition were constrained. This univariate comparison ignores the off-diagonal elements that are dominated by the highly correlated MOZART invariant parameter error, which, as far as we are aware, has not been considered in previous studies. The larger diagonal elements than previous studies

extends the range of acceptable values of the methane mole fraction and δ^{13}C-CH_4, but the far greater increase in the off-diagonal elements reduces the number of accepted values, because the differences between the accepted simulations and the observations must be highly correlated. Therefore, this change in the covariance matrix has the potential to change not just the uncertainty in the results, but also the median result itself. For example, in the univariate comparison, the median accepted wetlands trend parameter is approximately that of the emission inventory, but becomes 13 % higher in the multivariate comparison.

Both the univariate and multivariate comparisons have large ranges of accepted possible parameter values. This large range of acceptable parameters could explain why so many top-down studies have come to different conclusions for the recent methane trends whilst using the same datasets. There are many possible parameter combinations, and the solution depends strongly on each study's assumptions and methods.

To find the optimal parameters, a Bayesian inversion should be conducted. This would be an interesting piece of further work to see how the optimal solution (and its uncertainty) differs from previous studies. In this work, the median values of the constrained parameter ranges were examined, in order to investigate the most likely cause of the recent observed increase in methane mole fraction. The wetlands trend was the only source trend to differ significantly from the initial values, and so the methane mole fraction increase comes from the initial emission inventory trends of fossil fuels, agriculture, and waste, with a larger increase in wetlands than in the bottom-up model. The effect of these increasing sources is damped by increasing OH loss. Previous studies that include OH variation tend to find OH has decreased or changed non-linearly over this period (Rigby et al. 2017, Turner et al. 2017, McNorton et al. 2018). These differences could be explained by this work including the trends in the emissions inventories, so that the mean parameters produce a stronger methane mole fraction trend than the observations. Therefore, the increasing OH may be because the emission inventory trends are too strong. Alternatively, the positive OH trend could be correct. For example, the OH trend

derived in this work is similar to Stevenson et al. (2020).

The use of δ^{13}C-CH_4 observations, in addition to the methane mole fraction, was demonstrated to be limited for this work. When only the methane mole fraction simulations were compared to observations, only three parameters were less constrained than when both the methane mole fraction and δ^{13}C-CH_4 was used. Two of these parameters were the agricultural source δ^{13}C-CH_4 and the initial source δ^{13}C-CH_4, which are only included to use the δ^{13}C-CH_4 observations. Only the third constrained parameter, the wetlands trend, informs us about the terms in the methane budget.

This system is not without flaws. The fixed emissions and loss fields (spatially and temporally) mean that any errors in these fields are carried forward into all the emulator outputs. However, including these spatial distributions as parameters in the system would require other parameters (e.g. the different source types) to be dropped. This is because there is a limit on the number of MOZART training simulations that can be carried out in a reasonable timescale, and the more parameters, the more training simulations are required. Though perhaps the same setup in this work with different emission inventories could be used, and the accuracy of different emissions inventories compared.

Chapter 6

Conclusions

This thesis presents the first application of Gaussian process emulation to greenhouse gas modelling. This technique can approximate the relationship between inputs and outputs of a three-dimensional chemical transport model (CTM) but with the computational efficiency (once training simulations have been run) of a two-dimensional box model. Previous studies that have used three-dimensional CTM output, have tended to use input-output sensitivities, rather than repeatedly running the model. This can be done with an adjoint model, which is difficult to code and is only applicable to one model version, so is not widely available. Alternatively, linear sensitivities have also been calculated using finite difference approaches for basis function decompositions of the source or loss fields. These methods also require simplifying assumptions, such as finding a local minimum rather than a full exploration of parameter space, Gaussian probability density functions, and only basic uncertainty calculations are viable. Alternatively, a two-dimensional box model can be used to more fully explore non-linearities or non-Gaussian uncertainties, but these models generally lack interannual variability in transport and have a high transport uncertainty, due to their coarse resolution. The Gaussian process emulation used in this work allows the more accurate three-dimensional CTM output to be used rather than linear approximations of input-output sensitivities, or a two-dimensional box model, overcoming the issues outlined above.

Using a training dataset of around 100 model simulations or more, the extra error

due to using an emulator instead of the three-dimensional CTM was found to be smaller than the CTM invariant parameter error, so using the emulator adds little uncertainty to the total error. However, there are limitations to Gaussian process emulation. It is only possible to explore about 30 model input parameters (whereas adjoint models can estimate thousands of parameters), so some parameters have to be fixed and their uncertainty remains unexplored.

In this thesis, Gaussian process emulation was used to investigate several aspects of the methane budget: the conclusions from the sensitivity analysis are presented in Section 6.1, the constraint of the methane budget in Section 6.2, and the uncertainty in the methane budget in Section 6.3. Opportunities for further work are discussed in Section 6.4, before the implications of this thesis in Section 6.5.

6.1 Sensitivity analysis

The emulators were used for two analyses that required millions of simulations, which would have been unfeasible using a three-dimensional CTM. The first was the sensitivity analysis outlined in Chapter 4, which aimed to find the sources and sinks whose uncertainties have the largest impacts on the modelled methane observations. These are the terms that should be prioritised in future research because a reduction in their uncertainty would lead to the largest reduction in the uncertainty in the modelled methane observable outputs. The most important terms were found to be the OH loss and freshwater emissions for the methane mole fraction, and Cl loss for δ^{13}C-CH_4.

These three important parameters have often been poorly represented in previous studies. The OH and Cl losses are often held constant, and this study is the first in methane modelling, as far as we are aware, to include a map of freshwater methane emissions independent of other sources. Without considering the range of possible values of these terms, it is likely that previous studies underestimate their uncertainties. The initial conditions are set up differently in every study, but the high sensitivity of the modelled δ^{13}C-CH_4 to the initial conditions in this work repre-

sents a large problem for constraining the methane budget. This work does examine a large range of δ^{13}C-CH_4 initial condition values, but the importance of this parameter holds even for small ranges. If the δ^{13}C-CH_4 initial condition is changed by 0.1 ‰ from the initial median parameter values, the output atmospheric δ^{13}C-CH_4 trend changes by 0.04 ‰, which is almost half the δ^{13}C-CH_4 trend in the observations. The long lag time between the cause of changes in δ^{13}C-CH_4 and the observed change creates this effect, and means that a long time series of δ^{13}C-CH_4 observations are required. There is limited δ^{13}C-CH_4 data before the 1990s, with INSTAAR only beginning to take measurements in the 1990s, although other studies have constructed longer time series using ice cores (Schaefer et al. 2016, Rice et al. 2016). Longer model runs would also be needed for modelling studies, increasing the computational burden. However, this work demonstrated the limited use of the δ^{13}C-CH_4 observations (due to the long lag time) when used over a short time period to constrain the methane budget in Chapter 5, where the methane mole fraction provided the majority of the constraint.

The sensitivity analysis in Chapter 4 also examined the interactions of the parameters. This was found to be small for all the outputs. Despite these small interactions, non-linearities in the methane budget mean that multiple linear regression was substantially worse than a Gaussian process at predicting the three-dimensional CTM output in Chapter 3. This means that these non-linearities are important when trying to estimate the methane mole fraction and δ^{13}C-CH_4 accurately, and should be considered (linearity has often been assumed in previous studies, e.g. McNorton et al. (2018)).

6.2 Constraint of the methane budget

The second analysis in this thesis aimed to constrain the uncertainty ranges of the sources and sinks of methane by comparing the emulator outputs to the observations. Only 10 out of 28 parameters had their possible ranges substantially reduced: the freshwater source magnitude, the OH loss magnitude, the OH loss trend, the δ^{13}C-

CH_4 source initial condition, the agricultural source δ^{13}C-CH_4, the wetlands source magnitude, the agricultural source magnitude, the fossil fuels source magnitude, the wetlands trend, and the initial loss magnitude. Those parameters that were constrained still have large ranges of plausible values, and so this work confirms that the methane budget is poorly constrained by hemispheric observations of the methane mole fraction and δ^{13}C-CH_4.

The median values of the constrained parameter ranges were examined to investigate the most likely cause of the recent increase in methane mole fraction. However, there are many different plausible explanations for the observed methane mole fraction increase since 2007, and these median parameters do not necessarily represent the optimal parameter values. The median value for the wetland emissions was the only source to differ substantially from the initial inventory trends. Therefore, according to our simulations, the methane mole fraction increase in 2007 is consistent with growing emission trends, predicted by bottom-up models of fossil fuels, agriculture, and waste, but with a larger than predicted growth in emissions from wetlands. The OH loss was also found to exhibit a positive trend, so the effect of these increasing sources is damped by increasing OH loss.

6.3 Uncertainty quantification

A primary aim of this thesis was to explore the uncertainty in the methane budget. This was achieved by several routes, the first being the inclusion of the uncertainty of highly uncertain terms that have been frequently left out of methane modelling studies: OH loss, Cl loss, and freshwater emissions, briefly discussed in Section 6.1. Additionally, in this work, the model invariant parameter error was quantified: the parameters that were fixed to simplify the analysis were varied to quantify their contribution to the uncertainty. This was found to be about 10 ppb and 0.1 ‰ for the monthly mean methane mole fraction and δ^{13}C-CH_4, respectively, which is large compared to the trends of 40 ppb and -0.1 ‰ over the time period in this work. This component of model error is often ignored or it is based on expert judgement in

previous studies. This error is a similar size to the model-measurement discrepancy error, so makes a significant contribution to the total error. Additionally, this error is highly correlated in time, meaning that a simulation that is consistently 20 ppb higher than observations can be considered more plausible than a simulation that varies from 10 ppb lower than observations to 10 ppb higher. This correlation has a large impact on the constraint of the methane budget, as seen in Chapter 5; when this correlation was not considered, only four, instead of ten, parameters were substantially constrained. This error changes not just the uncertainty, but also the median accepted parameters due to its highly correlated nature. For example, in the univariate comparison, the median accepted wetlands trend parameter is approximately that of the bottom-up model, but is 13 % higher in the multivariate comparison. Therefore, inclusion of this invariant parameter error has the potential to affect the conclusions of previous studies.

6.4 Further work

This study used Gaussian process emulation to produce hemispheric MOZART outputs, however, it should be trivial to extend this work to emulate individual MOZART grid cells. This could be done with the existing training dataset, and the MOZART grid cell output could be compared to the measurements taken at individual measurement stations rather than the hemispheric average. This would be beneficial as it would provide more degrees of freedom (e.g. sub-hemispheric latitudinal gradients) with which to constrain the methane budget.

In order to accurately represent the observations at measurement stations, the spatial resolution of the MOZART training simulations should be increased. This also allows more measurement stations to be included as the model will be able to resolve smaller scale effects. This higher resolution would be much more computationally expensive, but is possible as this thesis showed that about 100 simulations, rather than the 270 used, produced emulators with an emulator error less than the CTM invariant parameter error.

One of the largest drawbacks of Gaussian process emulation is the limited number of parameters that can be explored. This means that the spatial distributions, and many temporal trends, were held constant in this thesis. In order to further develop this work, the spatial and temporal distributions should be solved for, which may require the amalgamation of different source types into far fewer parameters. How to use the limited number of parameters efficiently should be further investigated. For example, perhaps coupling of emission process models and the atmospheric model would allow a parameter such as temperature to control the emissions from several sources, such as wetlands, fresh water, rice, and soil loss.

In order to get more constraint on the methane budget, other observations could be added to this work, for example, methyl chloroform to constrain the OH loss, or tracer gases such as ethane. Ethane's much shorter atmospheric lifetime than methane should mean a shorter time lag in the ratio of ethane to methane than δ^{13}C-CH_4. As a result, the ethane to methane ratio should be less sensitive to initial conditions than δ^{13}C-CH_4. Modelling these observations would potentially require additional parameters such as methyl chloroform and ethane emissions, which would have to be balanced with the limited parameter numbers of the Gaussian processes. Another way to increase the number of observations without increasing the number of parameters, would be to emulate satellite data rather than the surface data. This could be done with the existing training dataset (although all model levels would have to be used to calculate the column methane) as the size of the training dataset required depends on the number of inputs not outputs.

6.5 Implications of this thesis

The large range of possible parameter values in this thesis could explain why so many top-down studies reach different conclusions from the same datasets. The solution will depend on each study's assumptions and methods. For example, if studies start with different initial parameter magnitudes, they could find different local minima in the cost function, and hence different parameter combinations, that

reproduce the observations equally well. Therefore, studies that find an analytical solution or use techniques such as gradient descent to minimise the cost function are likely to underestimate the uncertainty in their solution, and potentially reach a solution that is not optimal. A full exploration of the parameter space is necessary to produce a reliable solution.

This work demonstrated how the off-diagonal elements of the covariance matrix, not considered in previous work, can change not only the uncertainties in the solution, but also the median solution. Therefore, a proper consideration of the uncertainties should be an integral part of any methane modelling study.

This work also demonstrated that the constraint from δ^{13}C-CH_4 observations should be treated with caution: the methane mole fraction provided most of the constraint in this work. This is because both the model invariant parameter error and the model-measurement discrepancy error are as large as the trend in the δ^{13}C-CH_4 observations, and the sensitivity to the initial conditions is large. Therefore, methane modelling studies should consider the best way to set up models to use this data. For example, the sensitivity to the initial conditions could be reduced by using a longer time series, and the invariant parameter error could be reduced by reducing the number of invariant parameters. However, both of these solutions will make methane modelling studies more computationally expensive.

This thesis investigated the methane budget, and its recent changes, using a new method. This has highlighted some of the key challenges in methane modelling, perhaps most importantly how under-determined the methane budget is, and hence how it is possible for different top-down studies to come to different conclusions using the same datasets. Without further constraint, the cause of the renewed methane growth in 2007 will remain unknown, with potentially serious consequences for the 2 °C target of the Paris Agreement.

References

Alexander, B. & Mickley, L. J. (2015), 'Paleo-Perspectives on Potential Future Changes in the Oxidative Capacity of the Atmosphere Due to Climate Change and Anthropogenic Emissions', *Current Pollution Reports* **1**(2), 57–69.

Allan, W., Struthers, H. & Lowe, D. C. (2007), 'Methane carbon isotope effects caused by atomic chlorine in the marine boundary layer: Global model results compared with Southern Hemisphere measurements', *Journal of Geophysical Research* **112**(D4), D04306.

Allen, D. T., Torres, V. M., Thomas, J., Sullivan, D. W., Harrison, M., Hendler, A., Herndon, S. C., Kolb, C. E., Fraser, M. P., Hill, A. D., Lamb, B. K., Miskimins, J., Sawyer, R. F. & Seinfeld, J. H. (2013), 'Measurements of methane emissions at natural gas production sites in the United States', *Proceedings of the National Academy of Sciences* **110**(44), 17768–17773.

AMAP (2015), AMAP assessment 2015: Methane as an Arctic climate forcer, Technical report, Arctic Monitoring and Assessment Programme (AMAP), Oslo, Normway.

Antonov, I. & Saleev, V. (1979), 'An economic method of computing LPτ-sequences', *USSR Computational Mathematics and Mathematical Physics* **19**(1), 243–245.

Archer, D. & Brovkin, V. (2008), 'The millennial atmospheric lifetime of anthropogenic CO2', *Climatic Change* **90**(3), 283–297.

Arndt, C., Leytem, A. B., Hristov, A. N., Zavala-Araiza, D., Cativiela, J. P., Conley, S., Daube, C., Faloona, I. & Herndon, S. C. (2018), 'Short-term methane emissions from 2 dairy farms in California estimated by different measurement techniques and US Environmental Protection Agency inventory methodology: A case study', *Journal of Dairy Science* **101**(12), 11461–11479.

Avis, C. A., Weaver, A. J. & Meissner, K. J. (2011), 'Reduction in areal extent of high-latitude wetlands in response to permafrost thaw', *Nature Geoscience* **4**(7), 444–448.

Bailis, R., Ezzati, M. & Kammen, D. M. (2005), 'Mortality and greenhouse gas impacts of biomass and petroleum energy futures in Africa', *Science* **308**(5718), 98–103.

Bastos, L. S. & O'Hagan, A. (2009), 'Diagnostics for gaussian process emulators', *Technometrics* **51**(4), 425–438.

Bastviken, D., Cole, J., Pace, M. & Tranvik, L. (2004), 'Methane emissions from lakes: Dependence of lake characteristics, two regional assessments, and a global estimate', *Global Biogeochemical Cycles* **18**(4), GB4009.

Bastviken, D., Santoro, A. L., Marotta, H., Pinho, L. Q., Calheiros, D. F., Crill, P. & Enrich-Prast, A. (2010), 'Methane emissions from pantanal, South America, during the low water season: Toward more comprehensive sampling', *Environmental Science and Technology* **44**(14), 5450–5455.

Bastviken, D., Tranvik, L. J., Downing, J. A., Crill, P. M. & Enrich-Prast, A. (2011), 'Freshwater methane emissions offset the continental carbon sink', *Science* **331**(6013), 50.

Bender, M., Sowers, T. & Brook, E. (1997), 'Gases in ice cores', *Proceedings of the National Academy of Sciences of the United States of America* **94**(16), 8343–8349.

Bergamaschi, P., Brenninkmeijer, C. A. M., Hahn, M., Röckmann, T., Scharffe, D. H., Crutzen, P. J., Elansky, N. F., Belikov, I. B., Trivett, N. B. A. & Worthy, D. E. J. (1998), 'Isotope analysis based source identification for atmospheric CH4 and CO sampled across Russia using the Trans-Siberian railroad', *Journal of Geophysical Research: Atmospheres* **103**(D7), 8227–8235.

Bergamaschi, P., Houweling, S., Segers, A., Krol, M., Frankenberg, C., Scheepmaker, R. A., Dlugokencky, E., Wofsy, S. C., Kort, E. A., Sweeney, C., Schuck, T., Brenninkmeijer, C., Chen, H., Beck, V. & Gerbig, C. (2013), 'Atmospheric CH4 in the first decade of the 21st century: Inverse modeling analysis using SCIAMACHY satellite retrievals and NOAA surface measurements', *Journal of Geophysical Research Atmospheres* **118**(13), 7350–7369.

Bloom, A. A., Bowman, W. K., Lee, M., Turner, J. A., Schroeder, R., Worden, R. J., Weidner, R., McDonald, C. K. & Jacob, J. D. (2017), 'A global wetland methane emissions and uncertainty dataset for atmospheric chemical transport models (WetCHARTs version 1.0)', *Geoscientific Model Development* **10**(6), 2141–2156.

Boerboom, R., Vatamanu, M. & Zegers, D. (2010), 'Dramatic reduction in emissions of methane from landfills in the Netherlands: Additional measures considered', *Journal of Integrative Environmental Sciences* **7**(S1), 167–174.

Bogner, J., Spokas, K., Burton, E., Sweeney, R. & Corona, V. (1995), 'Landfills as atmospheric methane sources and sinks', *Chemosphere* **31**(9), 4119–4130.

Borges, A. V., Darchambeau, F., Teodoru, C. R., Marwick, T. R., Tamooh, F., Geeraert, N., Omengo, F. O., Guérin, F., Lambert, T., Morana, C., Okuku, E. & Bouillon, S. (2015), 'Globally significant greenhouse-gas emissions from African inland waters', *Nature Geoscience* **8**(8), 637–642.

Bouchard, F., Francus, P., Pienitz, R., Laurion, I. & Feyte, S. (2014), 'Subarctic thermokarst ponds: Investigating recent landscape evolution and sediment dynamics in thawed permafrost of Northern Québec (Canada)', *Arctic, Antarctic, and Alpine Research* **46**(1), 251–271.

Bousquet, P., Ringeval, B., Pison, I., Dlugokencky, E. J., Brunke, E. G., Carouge, C., Chevallier, F., Fortems-Cheiney, A., Frankenberg, C., Hauglustaine, D. A., Krummel, P. B., Langenfelds, R. L., Ramonet, M., Schmidt, M., Steele, L. P., Szopa, S., Yver, C., Viovy, N. & Ciais, P. (2011), 'Source attribution of the changes in atmospheric methane for 2006-2008', *Atmospheric Chemistry and Physics* **11**(8), 3689–3700.

Bridgham, S. D., Cadillo-Quiroz, H., Keller, J. K. & Zhuang, Q. (2013), 'Methane emissions from wetlands: Biogeochemical, microbial, and modeling perspectives from local to global scales', *Global Change Biology* **19**(5), 1325–1346.

Brook, E. J., Sowers, T. & Orchardo, J. (1996), 'Rapid variations in atmospheric methane concentration during the past 110,000 years', *Science* **273**(5278), 1087–1091.

Bruhwiler, L. M., Michalak, A. M., Peters, W., Baker, D. F. & Tans, P. (2005), 'An improved Kalman smoother for atmospheric inversions', *Atmospheric Chemistry and Physics* **5**(10), 2691–2702.

Burkholder, J. B., Sander, S. P., Abbatt, J., Barker, J. R., Huie, R. E., Kolb, C. E., Kurylo, M. J., Orkin, V. L., Wilmouth, D. M. & Wine, P. H. (2015), Chemical Kinetics and Photochemical Data for Use in Atmospheric Studies, Evaluation Number 18, Technical Report 10, Jet Propulsion Laboratory, Pasadena.

Campbell, J. E., Carmichael, G. R., Chai, T., Mena-Carrasco, M., Tang, Y., Blake, D. R., Blake, N. J., Vay, S. A., Collatz, G. J., Baker, I., Berry, J. A., Montzka, S. A., Sweeney, C., Schnoor, J. L. & Stanier, C. O. (2008), 'Photosynthetic Control of Atmospheric Carbonyl Sulfide During the Growing Season', *Science* **322**(5904), 1085–1088.

Cantrell, C. A., Shetter, R. E., McDaniel, A. H., Calvert, J. G., Davidson, J. A., Lowe, D. C., Tyler, S. C., Cicerone, R. J. & Greenberg, J. P. (1990), 'Carbon kinetic isotope effect in the oxidation of methane by the hydroxyl radical', *Journal of Geophysical Research* **95**(D13), 22455–22462.

Chang, W., Applegate, P. J., Haran, M. & Keller, K. (2014), 'Probabilistic calibration of a Greenland ice sheet model using spatially resolved synthetic observations: Toward projections of ice mass loss with uncertainties', *Geoscientific Model Development* **7**(5), 1933–1943.

Chappellaz, J., Barnola, J. M., Raynaud, D., Korotkevich, Y. S. & Lorius, C. (1990), 'Ice-core record of atmospheric methane over the past 160,000 years', *Nature* **345**(6271), 127–131.

Chappellaz, J., Bluniert, T., Raynaud, D., Barnola, J. M., Schwander, J. & Stauffert, B. (1993), 'Synchronous changes in atmospheric CH4 and Greenland climate between 40 and 8 kyr BP', *Nature* **366**(6454), 443–445.

Chowdhury, T. R. & Dick, R. P. (2013), 'Ecology of aerobic methanotrophs in controlling methane fluxes from wetlands', *Applied Soil Ecology* **65**, 8–22.

Collins, M., Knutti, R., Arblaster, J., Dufresne, J.-L., Fichefet, T., Friedlingstein, P., Gao, X., Gutowski, W., Johns, T., Krinner, G., Shongwe, M., Tebaldi, C., Weaver, A. & Wehner, M. (2013), Long-term climate change: Projections, commitments and irreversibility, *in* T. Stocker, D. Qin, G.-K. Plattner, M. Tignor, S. Allen, J. Boschung, A. Nauels, Y. Xia, V. Bex & P. Midgley, eds, 'Climate Change 2013 the Physical Science Basis: Working Group I Contribution to the Fifth Assessment Report of the Intergovernmental Panel on Climate Change', Cambridge University Press, Cambridge, United Kingdom and New York, NY, USA.

Conrad, R., Klose, M. & Claus, P. (2000), 'Phosphate inhibits acetotrophic methanogenesis on rice roots', *Applied and Environmental Microbiology* **66**(2), 828–831.

Conti, S. & O'Hagan, A. (2010), 'Bayesian emulation of complex multi-output and dynamic computer models', *Journal of Statistical Planning and Inference* **140**(3), 640–651.

Coplen, T. B. (2011), 'Guidelines and recommended terms for expression of stable-isotope-ratio and gas-ratio measurement results', *Rapid Communications in Mass Spectrometry* **25**(17), 2538–2560.

Craig, P. S., Goldstein, M., Seheult, A. H. & Smith, J. A. (1996), 'Bayes linear strategies for matching hydrocarbon reservoir history', *Bayesian Statistics* **5**, 69–95.

Craig, P. S., Goldstein, M., Seheult, A. H. & Smith, J. A. (1997), Pressure Matching for Hydrocarbon Reservoirs: A Case Study in the Use of Bayes Linear Strategies for Large Computer Experiments, *in* 'Case Studies in Bayesian Statistics. Lecture Notes in Statistics, vol 121', Springer, New York, pp. 37–93.

Crippa, M., Guizzardi, D., Muntean, M., Schaaf, E., Dentener, F., van Aardenne, J. A., Monni, S., Doering, U., Olivier, J. G. J., Pagliari, V. & Janssens-Maenhout, G. (2018), 'Gridded emissions of air pollutants for the period 1970–2012 within EDGAR v4.3.2', *Earth System Science Data* **10**(4), 1987–2013.

Crowley, J., Saueressig, G., Bergamaschi, P., Fischer, H. & Harris, G. (1999), 'Carbon kinetic isotope effect in the reaction CH4+Cl: a relative rate study using FTIR spectroscopy', *Chemical Physics Letters* **303**(3-4), 268–274.

Crutzen, P. J., Aselmann, I. & Seiler, W. (1986), 'Methane production by domestic animals, wild ruminants, other herbivorous fauna, and humans', *Tellus B: Chemical and Physical Meteorology* **38**(3-4), 271–284.

Curry, C. L. (2007), 'Modeling the soil consumption of atmospheric methane at the global scale', *Global Biogeochemical Cycles* **21**(4), GB4012.

Czepiel, P. M., Crill, P. M. & Harriss, R. C. (1995), 'Environmental factors influencing the variability of methane oxidation in temperate zone soils', *Journal of Geophysical Research* **100**(D5), 9359–9364.

Daelman, M. R., van Voorthuizen, E. M., van Dongen, U. G., Volcke, E. I. & van Loosdrecht, M. C. (2012), 'Methane emission during municipal wastewater treatment', *Water Research* **46**(11), 3657–3670.

Davidson, J. A., Cantrell, C. A., Tyler, S. C., Shetter, R. E., Cicerone, R. J. & Calvert, J. G. (1987), 'Carbon kinetic isotope effect in the reaction of CH4 with HO', *Journal of Geophysical Research* **92**(D2), 2195.

Davidson, T. A., Audet, J., Jeppesen, E., Landkildehus, F., Lauridsen, T. L., Søndergaard, M. & Syväranta, J. (2018), 'Synergy between nutrients and warming enhances methane ebullition from experimental lakes', *Nature Climate Change* **8**(2), 156–160.

de Mes, T., Stams, A., Reith, J. & Zeeman, G. (2003), Methane production by anaerobic digestion of wastewater and solid wastes, *in* 'Biomethane and biohydrogen', Dutch Biological Hydrogen Foundation.

Dlugokencky, E. J. (2003), 'Atmospheric methane levels off: Temporary pause or a new steady-state?', *Geophysical Research Letters* **30**(19), 1992.

Dlugokencky, E. J. (2020), 'NOAA/ ESRL Trends in Atmospheric Methane'.
URL: *https://www.esrl.noaa.gov/gmd/ccgg/trends_ch4/*

Dlugokencky, E. J., Bruhwiler, L., White, J. W. C., Emmons, L. K., Novelli, P. C., Montzka, S. A., Masarie, K. A., Lang, P. M., Crotwell, A. M., Miller, J. B. & Gatti, L. V. (2009), 'Observational constraints on recent increases in the atmospheric CH4 burden', *Geophysical Research Letters* **36**(18), L18803.

Dlugokencky, E. J., Steele, L. P., Lang, P. M. & Masarie, K. A. (1994), 'The growth rate and distribution of atmospheric methane', *Journal of Geophysical Research* **99**(D8), 17021–17043.

Dlugokencky, E. J. & Tans, P. (2020), 'NOAA/ESRL Trends in Atmospheric Carbon Dioxide'.
URL: *www.esrl.noaa.gov/gmd/ccgg/trends/*

Dlugokencky, E., Lang, P., Crotwell, A., Mund, J., Crotwell, M. & Thoning, K. (2017), 'Atmospheric Methane Dry Air Mole Fractions from the NOAA ESRL Carbon Cycle Cooperative Global Air Sampling Network, 1983-2016, Version: 2017-07-28'.
URL: *ftp://aftp.cmdl.noaa.gov/data/trace_gases/ch4/flask/surface/*

Dutaur, L. & Verchot, L. V. (2007), 'A global inventory of the soil CH 4 sink', *Global Biogeochemical Cycles* **21**(4), GB4013.

Ebden, M. (2015), 'Gaussian Processes: A Quick Introduction', *arXiv:1505.02965v2 [math.ST]* .

Ehhalt, D. H. (1974), 'The atmospheric cycle of methane', *Tellus* **26**(1-2), 58–70.

Ehhalt, D. H. & Heidt, L. E. (1973), 'Vertical profiles of CH4 in the troposphere and stratosphere', *Journal of Geophysical Research* **78**(24), 5265–5271.

Elshorbany, Y. F., Kurtenbach, R., Wiesen, P., Lissi, E., Rubio, M., Villena, G., Gramsch, E., Rickard, A. R., Pilling, M. J. & Kleffmann, J. (2009), 'Oxidation capacity of the city air of Santiago, Chile', *Atmospheric Chemistry and Physics* **9**(6), 2257–2273.

Emkes, H., Coulon, F. & Wagland, S. (2015), 'A decision support tool for landfill methane generation and gas collection', *Waste Management* **43**, 307–318.

Emmons, L. K., Walters, S., Hess, P. G., Lamarque, J.-F., Pfister, G. G., Fillmore, D., Granier, C., Guenther, A., Kinnison, D., Laepple, T., Orlando, J., Tie, X., Tyndall, G., Wiedinmyer, C., Baughcum, S. L. & Kloster, S. (2010), 'Description and evaluation of the Model for Ozone and Related chemical Tracers, version 4 (MOZART-4)', *Geoscientific Model Development Discussions* **3**(2), 43–67.

Etheridge, D. M., Steele, L. P., Francey, R. J. & Langenfelds, R. L. (1998), 'Atmospheric methane between 1000 A.D. and present: Evidence of anthropogenic emissions and climatic variability', *Journal of Geophysical Research: Atmospheres* **103**(D13), 15979–15993.

Etiope, G. & Klusman, R. W. (2002), 'Geologic emissions of methane to the atmosphere', *Chemosphere* **49**(8), 777–789.

Etiope, G. & Milkov, A. V. (2004), 'A new estimate of global methane flux from onshore and shallow submarine mud volcanoes to the atmosphere', *Environmental Geology* **46**(8), 997–1002.

Etminan, M., Myhre, G., Highwood, E. J. & Shine, K. P. (2016), 'Radiative forcing of carbon dioxide, methane, and nitrous oxide: A significant revision of the methane radiative forcing', *Geophysical Research Letters* **43**(24), 12614–12623.

FAO (2020), 'FAO live animal data'.
URL: *http://faostat3.fao.org*

Farah, M., Birrell, P., Conti, S. & Angelis, D. D. (2014), 'Bayesian Emulation and Calibration of a Dynamic Epidemic Model for A/H1N1 Influenza', *Journal of the American Statistical Association* **109**(508), 1398–1411.

Fearnside, P. M. (2005), 'Deforestation in Brazilian Amazonia: History, rates, and consequences', *Conservation Biology* **19**(3), 680–688.

Fung, I., John, J., Lerner, J., Matthews, E., Prather, M., Steele, L. P. & Fraser, P. J. (1991), 'Three-dimensional model synthesis of the global methane cycle', *Journal of Geophysical Research* **96**(D7), 13033–13065.

Ganesan, A. L., Schwietzke, S., Poulter, B., Arnold, T., Lan, X., Rigby, M., Vogel, F. R., van der Werf, G. R., Janssens-Maenhout, G., Boesch, H., Pandey, S., Manning, A. J., Jackson, R. B., Nisbet, E. G. & Manning, M. R. (2019), 'Advancing

Scientific Understanding of the Global Methane Budget in Support of the Paris Agreement', *Global Biogeochemical Cycles* **33**(12), 1475–1512.

Ganesan, A. L., Stell, A. C., Gedney, N., Comyn-Platt, E., Hayman, G., Rigby, M., Poulter, B. & Hornibrook, E. (2018), 'Spatially Resolved Isotopic Source Signatures of Wetland Methane Emissions', *Geophysical Research Letters* **45**(8), 3737–3745.

Gay, D. M. (1990), Usage Summary for Selected Optimization Routines (PORT Mathematical Subroutine Library, Optimization chapter), Technical Report 153, AT&T Bell Laboratories, Murray Hill, NJ 07974.

Gillett, R. W., Van Ommen, T. D., Jackson, A. V. & Ayers, G. P. (2000), 'Formaldehyde and peroxide concentrations in Law Dome (Antarctica) firn and ice cores', *Journal of Glaciology* **46**(152), 15–19.

Gligorovski, S., Strekowski, R., Barbati, S. & Vione, D. (2015), 'Environmental Implications of Hydroxyl Radicals (• OH)', *Chemical Reviews* **115**(24), 13051–13092.

Guérin, F., Abril, G., Richard, S., Burban, B., Reynouard, C., Seyler, P. & Delmas, R. (2006), 'Methane and carbon dioxide emissions from tropical reservoirs: Significance of downstream rivers', *Geophysical Research Letters* **33**(21), L21407.

Gupta, M. L., Mcgrath, M. P., Cicerone, R. J., Rowland, F. S. & Wolfsberg, M. (1997), '12C/13C kinetic isotope effects in the reactions of CH4 with OH and CI', *Geophysical Research Letters* **24**(22), 2761–2764.

Gutenberg, L., Krauss, K. W., Qu, J. J., Ahn, C., Hogan, D., Zhu, Z. & Xu, C. (2019), 'Carbon Dioxide Emissions and Methane Flux from Forested Wetland Soils of the Great Dismal Swamp, USA', *Environmental Management* **64**(2), 190–200.

Hausmann, P., Sussmann, R. & Smale, D. (2016), 'Contribution of oil and natural gas production to renewed increase in atmospheric methane (2007-2014): Top-down estimate from ethane and methane column observations', *Atmospheric Chemistry and Physics* **16**(5), 3227–3244.

Heard, D. E. (2006), 'Atmospheric field measurements of the hydroxyl radical using laser-induced fluorescence spectroscopy', *Annual Review of Physical Chemistry* **57**, 191–216.

Heard, D. E. & Pilling, M. J. (2003), 'Measurement of OH and HO2 in the Troposphere', *Chemical Reviews* **103**(12), 5163–5198.

Herring, S. C., Christidis, N., Hoell, A., Hoerling, M. P. & Stott, P. A. (2020), 'Explaining Extreme Events of 2018 from a Climate Perspective', *Bulletin of the American Meteorological Society* **101**(1), S1–S134.

Hmiel, B., Petrenko, V. V., Dyonisius, M. N., Buizert, C., Smith, A. M., Place, P. F., Harth, C., Beaudette, R., Hua, Q., Yang, B., Vimont, I., Michel, S. E.,

Severinghaus, J. P., Etheridge, D., Bromley, T., Schmitt, J., Faïn, X., Weiss, R. F. & Dlugokencky, E. (2020), 'Preindustrial 14CH4 indicates greater anthropogenic fossil CH4 emissions', *Nature* **578**(7795), 409–412.

Holgerson, M. A. & Raymond, P. A. (2016), 'Large contribution to inland water CO2 and CH4 emissions from very small ponds', *Nature Geoscience* **9**(3), 222–226.

Hopcroft, P. O., Valdes, P. J., O'Connor, F. M., Kaplan, J. O. & Beerling, D. J. (2017), 'Understanding the glacial methane cycle', *Nature Communications* **8**(1), 14383.

Houweling, S., Kaminski, T., Dentener, F., Lelieveld, J. & Heimann, M. (1999), 'Inverse modeling of methane sources and sinks using the adjoint of a global transport model', *Journal of Geophysical Research: Atmospheres* **104**(D21), 26137–26160.

Hristov, A. N., Kebreab, E., Niu, M., Oh, J., Bannink, A., Bayat, A. R., Boland, T. M., Brito, A. F., Casper, D. P., Crompton, L. A., Dijkstra, J., Eugène, M., Garnsworthy, P. C., Haque, N., Hellwing, A. L., Huhtanen, P., Kreuzer, M., Kuhla, B., Lund, P., Madsen, J., Martin, C., Moate, P. J., Muetzel, S., Muñoz, C., Peiren, N., Powell, J. M., Reynolds, C. K., Schwarm, A., Shingfield, K. J., Storlien, T. M., Weisbjerg, M. R., Yáñez-Ruiz, D. R. & Yu, Z. (2018), 'Symposium review: Uncertainties in enteric methane inventories, measurement techniques, and prediction models', *Journal of Dairy Science* **101**(7), 6655–6674.

Hu, H., Landgraf, J., Detmers, R., Borsdorff, T., Aan de Brugh, J., Aben, I., Butz, A. & Hasekamp, O. (2018), 'Toward Global Mapping of Methane With TROPOMI: First Results and Intersatellite Comparison to GOSAT', *Geophysical Research Letters* **45**(8), 3682–3689.

IPCC (2006), *2006 IPCC Guidelines for National Greenhouse Gas Inventories, Prepared by the National Greenhouse Gas Inventories Programme*, IGES, Hayama, Japan.

IPCC (2014), *Climate Change 2014 Part A: Global and Sectoral Aspects*, Cambridge University Press, Cambridge, United Kingdom and New York, NY, USA.

IPCC (2018), An IPCC Special Report on the impacts of global warming of 1.5°C above pre-industrial levels and related global greenhouse gas emission pathways, in the context of strengthening the global response to the threat of climate change, sustainable development, *in* 'Global Warming of 1.5°C', World Meteorological Organization, Geneva, Switzerland.

Jacob, D. J., Turner, A. J., Maasakkers, J. D., Sheng, J., Sun, K., Liu, X., Chance, K., Aben, I., McKeever, J. & Frankenberg, C. (2016), 'Satellite observations of atmospheric methane and their value for quantifying methane emissions', *Atmospheric Chemistry and Physics* **16**(22), 14371–14396.

John, J. G., Fiore, A. M., Naik, V., Horowitz, L. W. & Dunne, J. P. (2012), 'Climate versus emission drivers of methane lifetime against loss by tropospheric OH from 1860-2100', *Atmospheric Chemistry and Physics* **12**(24), 12021–12036.

Karacan, C. Ö., Ruiz, F. A., Cotè, M. & Phipps, S. (2011), 'Coal mine methane: A review of capture and utilization practices with benefits to mining safety and to greenhouse gas reduction', *International Journal of Coal Geology* **86**(2-3), 121–156.

Kasischke, E. S., Christensen, N. J. & Stocks, B. J. (1995), 'Fire , Global Warming, and the Carbon Balance of Boreal Forests', *Ecological Applications* **5**(2), 437–451.

Kennedy, M. (2009), 'The GEM software'.
URL: *http://www.tonyohagan.co.uk/academic/GEM/*

Kennedy, M., Anderson, C., O'Hagan, A., Lomas, M., Woodward, I. & Gosling, J. P. (2008), 'Quantifying uncertainty in the biospheric carbon flux for England and Wales', *Journal of the Royal Statistical Society: Series A* **171**(Part 1), 109–135.

King, S. L., Quay, P. D. & Lansdown, J. M. (1989), 'The 13C/ 12C kinetic isotope effect for soil oxidation of methane at ambient atmospheric concentrations', *Journal of Geophysical Research* **94**(D15), 18273–18277.

Kinley, R. D., Martinez-Fernandez, G., Matthews, M. K., de Nys, R., Magnusson, M. & Tomkins, N. W. (2020), 'Mitigating the carbon footprint and improving productivity of ruminant livestock agriculture using a red seaweed', *Journal of Cleaner Production* **259**, 120836.

Kirschke, S., Bousquet, P., Ciais, P., Saunois, M., Canadell, J. G., Dlugokencky, E. J., Bergamaschi, P., Bergmann, D., Blake, D. R., Bruhwiler, L., Cameron-Smith, P., Castaldi, S., Chevallier, F., Feng, L., Fraser, A., Heimann, M., Hodson, E. L., Houweling, S., Josse, B., Fraser, P. J., Krummel, P. B., Lamarque, J.-F., Langenfelds, R. L., Le Quéré, C., Naik, V., O'Doherty, S., Palmer, P. I., Pison, I., Plummer, D., Poulter, B., Prinn, R. G., Rigby, M., Ringeval, B., Santini, M., Schmidt, M., Shindell, D. T., Simpson, I. J., Spahni, R., Steele, L. P., Strode, S. A., Sudo, K., Szopa, S., van der Werf, G. R., Voulgarakis, A., van Weele, M., Weiss, R. F., Williams, J. E. & Zeng, G. (2013), 'Three decades of global methane sources and sinks', *Nature Geoscience* **6**(10), 813–823.

Kourzeneva, E., Asensio, H., Martin, E. & Faroux, S. (2012), 'Global gridded dataset of lake coverage and lake depth for use in numerical weather prediction and climate modelling', *Tellus, Series A: Dynamic Meteorology and Oceanography* **64**(1), 15640.

Krol, M. & Lelieveld, J. (2003), 'Can the variability in tropospheric OH be deduced from measurements of 1,1,1-trichloroethane (methyl chloroform)?', *Journal of Geophysical Research: Atmospheres* **108**(D3), 4125.

Kron, W., Löw, P. & Kundzewicz, Z. W. (2019), 'Changes in risk of extreme weather events in Europe', *Environmental Science & Policy* **100**, 74–83.

Kulp, S. A. & Strauss, B. H. (2019), 'New elevation data triple estimates of global vulnerability to sea-level rise and coastal flooding', *Nature Communications* **10**(1), 4844.

Kupper, T., Häni, C., Neftel, A., Kincaid, C., Bühler, M., Amon, B. & VanderZaag, A. (2020), 'Ammonia and greenhouse gas emissions from slurry storage - A review', *Agriculture, Ecosystems & Environment* **300**, 106963.

Lamb, B. K., Edburg, S. L., Ferrara, T. W., Howard, T., Harrison, M. R., Kolb, C. E., Townsend-Small, A., Dyck, W., Possolo, A. & Whetstone, J. R. (2015), 'Direct measurements show decreasing methane emissions from natural gas local distribution systems in the United States', *Environmental Science and Technology* **49**(8), 5161–5169.

Lambert, G. & Schmidt, S. (1993), 'Reevaluation of the oceanic flux of methane: Uncertainties and long term variations', *Chemosphere* **26**(1-4), 579–589.

Lasaga, A. C. & Gibbs, G. V. (1991), 'Ab initio studies of the kinetic isotope effect of the CH4 + OH• atmospheric reaction', *Geophysical Research Letters* **18**(7), 1217–1220.

Lassey, K. R., Etheridge, D. M., Lowe, D. C., Smith, A. M. & Ferretti, D. F. (2007), 'Centennial evolution of the atmospheric methane budget: What do the carbon isotopes tell us?', *Atmospheric Chemistry and Physics* **7**(8), 2119–2139.

Leach, N. J., Li, S., Sparrow, S., Van Oldenborgh, G. J., Lott, F. C., Weisheimer, A. & Allen, M. R. (2020), 'Anthropogenic influence on the 2018 summer warm spell in Europe: the impact of different spatio-temporal scales [in "Explaining extreme events of 2018 from a climate perspective"]', *Bulletin of the American Meteorological Society* **101**(1), S41–S46.

Lee, L. A., Carslaw, K. S., Pringle, K. J. & Mann, G. W. (2012), 'Mapping the uncertainty in global CCN using emulation', *Atmospheric Chemistry and Physics* **12**(20), 9739–9751.

Lee, L. A., Carslaw, K. S., Pringle, K. J., Mann, G. W. & Spracklen, D. V. (2011), 'Emulation of a complex global aerosol model to quantify sensitivity to uncertain parameters', *Atmospheric Chemistry and Physics* **11**(23), 12253–12273.

Lehner, B. & Döll, P. (2004), 'Development and validation of a global database of lakes, reservoirs and wetlands', *Journal of Hydrology* **296**(1-4), 1–22.

Levy, H. (1971), 'Normal atmosphere: Large radical and formaldehyde concentrations predicted', *Science* **173**(3992), 141–143.

Liu, Y. & Boone, D. R. (1991), 'Effects of salinity on methanogenic decomposition', *Bioresource Technology* **35**(3), 271–273.

Lobell, D. B., Burke, M. B., Tebaldi, C., Mastrandrea, M. D., Falcon, W. P. & Naylor, R. L. (2008), 'Prioritizing Climate Change Adaptation Needs for Food Security in 2030', *Science* **319**(5863), 607–610.

Lovelock, J. E. (1977), 'Methyl chloroform in the troposphere as an indicator of OH radical abundance', *Nature* **267**(5606), 32.

Lyon, D. R., Alvarez, R. A., Zavala-Araiza, D., Brandt, A. R., Jackson, R. B. & Hamburg, S. P. (2016), 'Aerial Surveys of Elevated Hydrocarbon Emissions from Oil and Gas Production Sites', *Environmental Science and Technology* **50**(9), 4877–4886.

Ma, K., Conrad, R. & Lu, Y. (2012), 'Responses of methanogen mcrA genes and their transcripts to an alternate dry/wet cycle of paddy field soil', *Applied and Environmental Microbiology* **78**(2), 445–454.

Mardia, K., Kent, J. & Bibby J.M. (1979), *Multivariate Analysis*, Academic Press Limited, London, United Kingdom.

Martinez, M., Harder, H., Kubistin, D., Rudolf, M., Eerdekens, G., Fischer, H., Klüpfel, T., Gurk, C., Königstedt, R., Parchatka, U., Schiller, C. L., Stickler, A., Williams, J. & Lelieveld, J. (2010), 'Hydroxyl radicals in the tropical troposphere over the Suriname rainforest: Airborne measurements', *Atmospheric Chemistry and Physics* **10**(8), 3759–3773.

McCarthy, M. C., Boering, K. A., Rice, A. L., Tyler, S. C., Connell, P. & Atlas, E. (2003), 'Carbon and hydrogen isotopic compositions of stratospheric methane: 2. Two-dimensional model results and implications for kinetic isotope effects', *Journal of Geophysical Research: Atmospheres* **108**(D15), 4461.

McCulloch, A. & Midgley, P. M. (2001), 'The history of methyl chloroform emissions: 1951-2000', *Atmospheric Environment* **35**(31), 5311–5319.

McGrath, W. & Norrish, R. (1960), 'Studies of the reactions of excited oxygen atoms and molecules produced in the flash photolysis of ozone', *Proceedings of the Royal Society of London. Series A. Mathematical and Physical Sciences* **254**(1278), 317–326.

McKay, M. D., Beckman, R. J. & Conover, W. J. (1979), 'A Comparison of Three Methods for Selecting Values of Input Variables in the Analysis of Output From a Computer Code', *Technometrics* **21**(2), 239–245.

McNorton, J., Wilson, C., Gloor, M., Parker, R. J., Boesch, H., Feng, W., Hossaini, R. & Chipperfield, M. P. (2018), 'Attribution of recent increases in atmospheric methane through 3-D inverse modelling', *Atmospheric Chemistry and Physics* **18**(24), 18149–18168.

Meinshausen, M., Nicholls, Z. R. J., Lewis, J., Gidden, M. J., Vogel, E., Freund, M., Beyerle, U., Gessner, C., Nauels, A., Bauer, N., Canadell, J. G., Daniel, J. S., John, A., Krummel, P. B., Luderer, G., Meinshausen, N., Montzka, S. A., Rayner, P. J., Reimann, S., Smith, S. J., van den Berg, M., Velders, G. J. M., Vollmer, M. K. & Wang, R. H. J. (2020), 'The shared socio-economic pathway (SSP) greenhouse gas concentrations and their extensions to 2500', *Geoscientific Model Development* **13**(8), 3571–3605.

Meinshausen, M., Smith, S. J., Calvin, K., Daniel, J. S., Kainuma, M. L., Lamarque, J., Matsumoto, K., Montzka, S. A., Raper, S. C., Riahi, K., Thomson, A., Velders, G. J. & van Vuuren, D. P. (2011), 'The RCP greenhouse gas concentrations and their extensions from 1765 to 2300', *Climatic Change* **109**(1), 213–241.

Melissas, V. S. & Truhlar, D. G. (1993), 'Interpolated variational transition state theory and tunneling calculations of the rate constant of the reaction OH+CH4 at 223-2400 K', *The Journal of Chemical Physics* **99**(2), 1013–1027.

Melton, J. R., Wania, R., Hodson, E. L., Poulter, B., Ringeval, B., Spahni, R., Bohn, T., Avis, C. A., Beerling, D. J., Chen, G., Eliseev, A. V., Denisov, S. N., Hopcroft, P. O., Lettenmaier, D. P., Riley, W. J., Singarayer, J. S., Subin, Z. M., Tian, H., Zürcher, S., Brovkin, V., Van Bodegom, P. M., Kleinen, T., Yu, Z. C. & Kaplan, J. O. (2013), 'Present state of global wetland extent and wetland methane modelling: Conclusions from a model inter-comparison project (WETCHIMP)', *Biogeosciences* **10**(2), 753–788.

Mengel, M., Levermann, A., Frieler, K., Robinson, A., Marzeion, B. & Winkelmann, R. (2016), 'Future sea level rise constrained by observations and long-term commitment', *Proceedings of the National Academy of Sciences of the United States of America* **113**(10), 2597–2602.

Menne, M. J., Williams, C. N., Gleason, B. E., Jared Rennie, J. & Lawrimore, J. H. (2018), 'The Global Historical Climatology Network Monthly Temperature Dataset, Version 4', *Journal of Climate* **31**(24), 9835–9854.

Midgley, P. M. & McCulloch, A. (1995), 'The production and global distribution of emissions to the atmosphere of 1,1,1-trichloroethane (methyl chloroform)', *Atmospheric Environment* **29**(14), 1601–1608.

Miller, J. B., Mack, K. A., Dissly, R., White, J. W., Dlugokencky, E. J. & Tans, P. P. (2002), 'Development of analytical methods and measurements of 13C/12C in atmospheric CH4 from the NOAA Climate Monitoring and Diagnostics Laboratory Global Air Sampling Network', *Journal of Geophysical Research Atmospheres* **107**(D13), 4178.

Mollicone, D., Eva, H. D. & Achard, F. (2006), 'Human role in Russian wild fires', *Nature* **440**(7083), 436–437.

Monteil, G., Houweling, S., Dlugockenky, E. J., Maenhout, G., Vaughn, B. H., White, J. W. & Rockmann, T. (2011), 'Interpreting methane variations in the past two decades using measurements of CH4 mixing ratio and isotopic composition', *Atmospheric Chemistry and Physics* **11**(17), 9141–9153.

Morris, M. D. & Mitchell, T. J. (1995), 'Exploratory designs for computational experiments', *Journal of Statistical Planning and Inference* **43**(3), 381–402.

Mount, G. H. & Williams, E. J. (1997), 'An overview of the Tropospheric OH Photochemistry Experiment, Fritz Peak/Idaho Hill, Colorado, fall 1993', *Journal of Geophysical Research Atmospheres* **102**(D5), 6171–6186.

Murguia-Flores, F., Arndt, S., Ganesan, A. L., Murray-Tortarolo, G. & Hornibrook, E. R. (2018), 'Soil Methanotrophy Model (MeMo v1.0): A process-based model to quantify global uptake of atmospheric methane by soil', *Geoscientific Model Development* **11**(6), 2009–2032.

Myhre, G., Shindell, D., Bréon, F.-M., Collins, W., Fuglestvedt, J., Huang, J., Koch, D., Lamarque, J.-F., Lee, D., Mendoza, B., Nakajima, T., Robock, A., Stephens, G., Takemura, T. & Zhang, H. (2013), Anthropogenic and Natural Radiative Forcing, *in* T. Stocker, D. Qin, G.-K. Plattner, M. Tignor, S. Allen, J. Boschung, A. Nauels, Y. Xia, V. Bex & P. Midgley, eds, 'Climate Change 2013: The Physical Science Basis. Contribution of Working Group I to the Fifth Assessment Report of the Intergovernmental Panel on Climate Change', Cambridge University Press, Cambridge, United Kingdom and New York, NY, USA, pp. 659–740.

Natchimuthu, S., Sundgren, I., Gålfalk, M., Klemedtsson, L., Crill, P., Danielsson, Å. & Bastviken, D. (2016), 'Spatio-temporal variability of lake CH 4 fluxes and its influence on annual whole lake emission estimates', *Limnology and Oceanography* **61**(S1), S13–S26.

Naus, S., Montzka, S. A., Pandey, S., Basu, S., Dlugokencky, E. J. & Krol, M. (2019), 'Constraints and biases in a tropospheric two-box model of OH', *Atmospheric Chemistry and Physics* **19**(1), 407–424.

Nguyen, N. H., Turner, A. J., Yin, Y., Prather, M. J. & Frankenberg, C. (2020), 'Effects of Chemical Feedbacks on Decadal Methane Emissions Estimates', *Geophysical Research Letters* **47**(3), 1–13.

Nicely, J. M., Canty, T. P., Manyin, M., Oman, L. D., Salawitch, R. J., Steenrod, S. D., Strahan, S. E. & Strode, S. A. (2018), 'Changes in Global Tropospheric OH Expected as a Result of Climate Change Over the Last Several Decades', *Journal of Geophysical Research: Atmospheres* **123**(18), 10,774–10,795.

Nisbet, E. G., Dlugokencky, E. J., Manning, M. R., Lowry, D., Fisher, R. E., France, J. L., Michel, S. E., Miller, J. B., White, J. W., Vaughn, B., Bousquet, P., Pyle, J. A., Warwick, N. J., Cain, M., Brownlow, R., Zazzeri, G., Lanoisellé, M., Manning, A. C., Gloor, E., Worthy, D. E., Brunke, E. G., Labuschagne, C., Wolff, E. W. & Ganesan, A. L. (2016), 'Rising atmospheric methane: 2007–2014 growth and isotopic shift', *Global Biogeochemical Cycles* **30**(9), 1356–1370.

Nisbet, E. G., Manning, M. R., Dlugokencky, E. J., Fisher, R. E., Lowry, D., Michel, S. E., Myhre, C. L., Platt, S. M., Allen, G., Bousquet, P., Brownlow, R., Cain, M., France, J. L., Hermansen, O., Hossaini, R., Jones, A. E., Levin, I., Manning, A. C., Myhre, G., Pyle, J. A., Vaughn, B. H., Warwick, N. J. & White, J. W. (2019), 'Very Strong Atmospheric Methane Growth in the 4 Years 2014–2017: Implications for the Paris Agreement', *Global Biogeochemical Cycles* **33**(3), 318–342.

NOAA (2020), 'What is the Global Greenhouse Gas Reference Network?'.
URL: *https://www.esrl.noaa.gov/gmd/ccgg/about.html*

Oakley, J. E. & O'Hagan, A. (2004), 'Probabilistic sensitivity analysis of complex models: A Bayesian approach', *Journal of the Royal Statistical Society. Series B: Statistical Methodology* **66**(3), 751–769.

O'Hagan, A. (2006), 'Bayesian analysis of computer code outputs: A tutorial', *Reliability Engineering and System Safety* **91**(10-11), 1290–1300.

Olson, R., Ruckert, K. L., Chang, W., Keller, K., Haran, M. & An, S. I. (2018), 'Stilt: Easy emulation of time series AR(1) computer model output in multidimensional parameter space', *The R Journal* **10**(2), 209–225.

Ozgen, S. & Caserini, S. (2018), 'Methane emissions from small residential wood combustion appliances: Experimental emission factors and warming potential', *Atmospheric Environment* **189**, 164–173.

Pandow, M., Mackay, C. & Wolfgang, R. (1960), 'The reaction of atomic carbon with oxygen: significance for the natural radio-carbon cycle', *Journal of Inorganic and Nuclear Chemistry* **14**(3-4), 153–158.

Patra, P. K., Houweling, S., Krol, M., Bousquet, P., Belikov, D., Bergmann, D., Bian, H., Cameron-Smith, P., Chipperfield, M. P., Corbin, K., Fortems-Cheiney, A., Fraser, A., Gloor, E., Hess, P., Ito, A., Kawa, S. R., Law, R. M., Loh, Z., Maksyutov, S., Meng, L., Palmer, P. I., Prinn, R. G., Rigby, M., Saito, R. & Wilson, C. (2011), 'TransCom model simulations of CH4 and related species: linking transport, surface flux and chemical loss with CH4 variability in the troposphere and lower stratosphere', *Atmospheric Chemistry and Physics* **11**(24), 12813–12837.

Patra, P. K., Krol, M. C., Montzka, S. A., Arnold, T., Atlas, E. L., Lintner, B. R., Stephens, B. B., Xiang, B., Elkins, J. W., Fraser, P. J., Ghosh, A., Hintsa, E. J., Hurst, D. F., Ishijima, K., Krummel, P. B., Miller, B. R., Miyazaki, K., Moore, F. L., Mühle, J., O'Doherty, S., Prinn, R. G., Steele, L. P., Takigawa, M., Wang, H. J., Weiss, R. F., Wofsy, S. C. & Young, D. (2014), 'Observational evidence for interhemispheric hydroxyl-radical parity', *Nature* **513**(7517), 219–223.

Pattnaik, P., Mishra, S. R., Bharati, K., Mohanty, S. R., Sethunathan, N. & Adhya, T. K. (2000), 'Influence of salinity on methanogenesis and associated microflora in tropical rice soils', *Microbiological Research* **155**(3), 215–220.

Petit, J. R., Jouzel, J., Raynaud, D., Barnola, J. M., Basile, I., Bender, M., Chappellaz, J., Davis, M., Delaygue, G., Delmotte, M., Kotlyakov, V. M., Legrand, M., Lipenkov, V. Y., Loriu, C., Pepin, L., Ritz, C., Saltzman, E. & Stievenard, M. (1999), 'Climate and atmospheric history of the past 420,000 years from the Vostok ice core, Antarctica', *Nature* **399**(6735), 429–436.

Plant, G., Kort, E. A., Floerchinger, C., Gvakharia, A., Vimont, I. & Sweeney, C. (2019), 'Large Fugitive Methane Emissions From Urban Centers Along the U.S. East Coast', *Geophysical Research Letters* **46**(14), 8500–8507.

Poppe, D., Zimmermann, J., Bauer, R., Brauers, T., Brüning, D., Callies, J., Dorn, H.-P., Hofzumahaus, A., Johnen, F.-J., Khedim, A., Koch, H., Koppmann, R., London, H., Müller, K.-P., Neuroth, R., Plass-Dülmer, C., Platt, U., Rohrer, F., Röth, E.-P., Rudolph, J., Schmidt, U., Wallasch, M. & Ehhalt, D. H. (1994), 'Comparison of measured OH concentrations with model calculations', *Journal of Geophysical Research* **99**(D8), 16633–16642.

Prather, M. J. (1996), 'Time scales in atmospheric chemistry: Theory, GWPs for CH4 and CO, and runaway growth', *Geophysical Research Letters* **23**(19), 2597–2600.

Prinn, R. G., Huang, J., Weiss, R. F., Cunnold, D. M., Fraser, P. J., Simmonds, P. G., McCulloch, A., Harth, C., Salameh, P., O'Doherty, S., Wang, R. H., Porter, L. & Miller, B. R. (2001), 'Evidence for substantial variations of atmospheric hydroxyl radicals in the past two decades', *Science* **292**(5523), 1882–1888.

Prinn, R. G., Weiss, R. F., Arduini, J., Arnold, T., Langley Dewitt, H., Fraser, P. J., Ganesan, A. L., Gasore, J., Harth, C. M., Hermansen, O., Kim, J., Krummel, P. B., Li, S., Loh, Z. M., Lunder, C. R., Maione, M., Manning, A. J., Miller, B. R., Mitrevski, B., Mühle, J., O'Doherty, S., Park, S., Reimann, S., Rigby, M., Saito, T., Salameh, P. K., Schmidt, R., Simmonds, P. G., Paul Steele, L., Vollmer, M. K., Wang, R. H., Yao, B., Yokouchi, Y., Young, D. & Zhou, L. (2018), 'History of chemically and radiatively important atmospheric gases from the Advanced Global Atmospheric Gases Experiment (AGAGE)', *Earth System Science Data* **10**(2), 985–1018.

Quay, P., King, S., White, D., Brockington, M., Plotkin, B., Gammon, R., Gerst, S. & Stutsman, J. (2000), 'Atmospheric 14CO : A tracer of OH concentration and mixing rates', *Journal of Geophysical Research* **105**(D12), 15147–15166.

Quay, P., Stutsman, J., Wilbur, D., Snover, A., Dlugokencky, E. & Brown, T. (1999), 'The isotopic composition of atmospheric methane', *Global Biogeochemical Cycles* **13**(2), 445–461.

Rasmussen, C. & Williams, K. (2006), *Gaussian Processes for Machine Learning*, The MIT Press, Cambridge, Massachusetts.

Reeburgh, W. S., Hirsch, A. I., Sansone, F. J., Popp, B. N. & Rust, T. M. (1997), 'Carbon kinetic isotope effect accompanying microbial oxidation of methane in boreal forest soils', *Geochimica et Cosmochimica Acta* **61**(22), 4761–4767.

Regayre, L. A., Johnson, J. S., Yoshioka, M., Pringle, K. J., Sexton, D. M. H., Booth, B. B. B., Lee, L. A., Bellouin, N. & Carslaw, K. S. (2018), 'Aerosol and physical atmosphere model parameters are both important sources of uncertainty in aerosol ERF', *Atmospheric Chemistry and Physics* **18**(13), 9975–10006.

Ren, X., Brune, W. H., Mao, J., Mitchell, M. J., Lesher, R. L., Simpas, J. B., Metcalf, A. R., Schwab, J. J., Cai, C., Li, Y., Demerjian, K. L., Felton, H. D.,

Boynton, G., Adams, A., Perry, J., He, Y., Zhou, X. & Hou, J. (2006), 'Behavior of OH and HO2 in the winter atmosphere in New York City', *Atmospheric Environment* **40**(SUPPL. 2), 252–263.

Rice, A. L., Butenhoff, C. L., Teama, D. G., Röger, F. H., Khalil, M. A. K. & Rasmussen, R. A. (2016), 'Atmospheric methane isotopic record favors fossil sources flat in 1980s and 1990s with recent increase', *Proceedings of the National Academy of Sciences of the United States of America* **113**(39), 10791–10796.

Rienecker, M. M., Suarez, M. J., Gelaro, R., Todling, R., Bacmeister, J., Liu, E., Bosilovich, M. G., Schubert, S. D., Takacs, L., Kim, G.-K., Bloom, S., Chen, J., Collins, D., Conaty, A., da Silva, A., Gu, W., Joiner, J., Koster, R. D., Lucchesi, R., Molod, A., Owens, T., Pawson, S., Pegion, P., Redder, C. R., Reichle, R., Robertson, F. R., Ruddick, A. G., Sienkiewicz, M. & Woollen, J. (2011), 'MERRA : NASA's Modern-Era Retrospective Analysis for Research and Applications', *Journal of Climate* **24**(14), 3624–3648.

Rigby, M., Montzka, S. A., Prinn, R. G., White, J. W. C., Young, D., O'Doherty, S., Lunt, M. F., Ganesan, A. L., Manning, A. J., Simmonds, P. G., Salameh, P. K., Harth, C. M., Mühle, J., Weiss, R. F., Fraser, P. J., Steele, L. P., Krummel, P. B., McCulloch, A. & Park, S. (2017), 'Role of atmospheric oxidation in recent methane growth', *Proceedings of the National Academy of Sciences* **114**(21), 5373–5377.

Rigby, M., Park, S., Saito, T., Western, L. M., Redington, A. L., Fang, X., Henne, S., Manning, A. J., Prinn, R. G., Dutton, G. S., Fraser, P. J., Ganesan, A. L., Hall, B. D., Harth, C. M., Kim, J., Kim, K. R., Krummel, P. B., Lee, T., Li, S., Liang, Q., Lunt, M. F., Montzka, S. A., Mühle, J., O'Doherty, S., Park, M. K., Reimann, S., Salameh, P. K., Simmonds, P., Tunnicliffe, R. L., Weiss, R. F., Yokouchi, Y. & Young, D. (2019), 'Increase in CFC-11 emissions from eastern China based on atmospheric observations', *Nature* **569**(7757), 546–550.

Rigby, M., Prinn, R. G., Fraser, P. J., Simmonds, P. G., Langenfelds, R. L., Huang, J., Cunnold, D. M., Steele, L. P., Krummel, P. B., Weiss, R. F., O'Doherty, S., Salameh, P. K., Wang, H. J., Harth, C. M., Mühle, J. & Porter, L. W. (2008), 'Renewed growth of atmospheric methane', *Geophysical Research Letters* **35**(22), L22805.

Roberto-Neto, O., Coitiño, E. L. & Truhlar, D. G. (1998), 'Dual-level direct dynamics calculations of deuterium and carbon-13 kinetic isotope effects for the reaction Cl + CH4', *Journal of Physical Chemistry A* **102**(24), 4568–4578.

Röckmann, T., Grooß, J.-U. & Müller, R. (2004), 'The impact of anthropogenic chlorine, stratospheric ozone change and chemical feedbacks on stratospheric water', *Atmospheric Chemistry and Physics Discussions* **4**(1), 693–699.

Román-Palacios, C. & Wiens, J. J. (2020), 'Recent responses to climate change reveal the drivers of species extinction and survival', *Proceedings of the National Academy of Sciences* **117**(8), 4211–4217.

Rudolph, J. (1995), 'The tropospheric distribution and budget of ethane', *Journal of Geophysical Research* **100**(D6), 11369–11381.

Rust, F. & Stevens, C. M. (1980), 'Carbon kinetic isotope effect in the oxidation of methane by hydroxyl', *International Journal of Chemical Kinetics* **12**(6), 371–377.

Saltelli, A. & Annoni, P. (2010), 'How to avoid a perfunctory sensitivity analysis', *Environmental Modelling and Software* **25**(12), 1508–1517.

Saltelli, A., Ratto, M., Andres, T., Campolongo, F., Cariboni, J., Gatelli, D., Saisana, M. & Tarantola, S. (2000), *Global Sensitivity Analysis: The Primer*, Wiley, Chichester, United Kingdom.

Saueressig, G., Bergamaschi, P., Crowley, J. N., Fischer, H. & Harris, G. W. (1995), 'Carbon kinetic isotope effect in the reaction of CH4 with Cl atoms', *Geophysical Research Letters* **22**(10), 1225–1228.

Saueressig, G., Crowley, J. N., Bergamaschi, P., Brühl, C., Brenninkmeijer, C. A. M. & Fischer, H. (2001), 'Carbon 13 and D kinetic isotope effects in the reactions of CH 4 with O(1 D) and OH: New laboratory measurements and their implications for the isotopic composition of stratospheric methane', *Journal of Geophysical Research: Atmospheres* **106**(D19), 23127–23138.

Saunois, M., Bousquet, P., Poulter, B., Peregon, A., Ciais, P., Canadell, J. G., Dlugokencky, E. J., Etiope, G., Bastviken, D., Houweling, S., Janssens-Maenhout, G., Tubiello, F. N., Castaldi, S., Jackson, R. B., Alexe, M., Arora, V. K., Beerling, D. J., Bergamaschi, P., Blake, D. R., Brailsford, G., Brovkin, V., Bruhwiler, L., Crevoisier, C., Crill, P., Covey, K., Curry, C., Frankenberg, C., Gedney, N., Höglund-Isaksson, L., Ishizawa, M., Ito, A., Joos, F., Kim, H. S., Kleinen, T., Krummel, P., Lamarque, J. F., Langenfelds, R., Locatelli, R., Machida, T., Maksyutov, S., McDonald, K. C., Marshall, J., Melton, J. R., Morino, I., Naik, V., O'Doherty, S., Parmentier, F. J. W., Patra, P. K., Peng, C., Peng, S., Peters, G. P., Pison, I., Prigent, C., Prinn, R., Ramonet, M., Riley, W. J., Saito, M., Santini, M., Schroeder, R., Simpson, I. J., Spahni, R., Steele, P., Takizawa, A., Thornton, B. F., Tian, H., Tohjima, Y., Viovy, N., Voulgarakis, A., Van Weele, M., Van Der Werf, G. R., Weiss, R., Wiedinmyer, C., Wilton, D. J., Wiltshire, A., Worthy, D., Wunch, D., Xu, X., Yoshida, Y., Zhang, B., Zhang, Z. & Zhu, Q. (2016), 'The global methane budget 2000-2012', *Earth System Science Data* **8**(2), 697–751.

Schaefer, H., Fletcher, S. E. M., Veidt, C., Lassey, K. R., Brailsford, G. W., Bromley, T. M., Dlugokencky, E. J., Michel, S. E., Miller, J. B., Levin, I., Lowe, D. C., Martin, R. J., Vaughn, B. H. & White, J. W. C. (2016), 'A 21st-century shift from fossil-fuel to biogenic methane emissions indicated by 13CH4', *Science* **352**(6281), 80–84.

Schuur, E. A. G., McGuire, A. D., Schädel, C., Grosse, G., Harden, J. W., Hayes, D. J., Hugelius, G., Koven, C. D., Kuhry, P., Lawrence, D. M., Natali, S. M., Olefeldt, D., Romanovsky, V. E., Schaefer, K., Turetsky, M. R., Treat, C. C. &

Vonk, J. E. (2015), 'Climate change and the permafrost carbon feedback', *Nature* **520**(7546), 171–179.

Schwietzke, S., Sherwood, O. A., Bruhwiler, L. M. P., Miller, J. B., Etiope, G., Dlugokencky, E. J., White, J. W. C., Pieter, P. T., Michel, S. E., Arling, V. A., Vaughn, B. H. & James, W. (2016), 'Upward revision of global fossil fuel methane emissions based on isotope database', *Nature* **538**(7623), 88–91.

Serreze, M. C. & Barry, R. G. (2011), 'Processes and impacts of Arctic amplification: A research synthesis', *Global and Planetary Change* **77**(1-2), 85–96.

Sherwen, T., Schmidt, J. A., Evans, M. J., Carpenter, L. J., Großmann, K., Eastham, S. D., Jacob, D. J., Dix, B., Koenig, T. K., Sinreich, R., Ortega, I., Volkamer, R., Saiz-Lopez, A., Prados-Roman, C., Mahajan, A. S. & Ordóñez, C. (2016), 'Global impacts of tropospheric halogens (Cl, Br, I) on oxidants and composition in GEOS-Chem', *Atmospheric Chemistry and Physics* **16**(18), 12239–12271.

Shindell, D. T., Walter, B. P. & Faluvegi, G. (2004), 'Impacts of climate change on methane emissions from wetlands', *Geophysical Research Letters* **31**(21), L21202.

Shorter, J. H., McManus, J. B., Kolb, C. E., Allwine, E. J., Lamb, B. K., Mosher, B. W., Harriss, R. C., Partchatka, U., Fischer, H., Harris, G. W., Crutzen, P. J. & Karbach, H. J. (1996), 'Methane emission measurements in urban areas in Eastern Germany', *Journal of Atmospheric Chemistry* **24**(2), 121–140.

Simpson, I. J., Rowland, F. S., Meinardi, S. & Blake, D. R. (2006), 'Influence of biomass burning during recent fluctuations in the slow growth of global tropospheric methane', *Geophysical Research Letters* **33**(22), L22808.

Snover, A. K. & Quay, P. D. (2000), 'Hydrogen and carbon kinetic isotope effects during soil uptake of atmospheric methane', *Global Biogeochemical Cycles* **14**(1), 25–39.

Sobol', I. (1967), 'On the distribution of points in a cube and the approximate evaluation of integrals', *USSR Computational Mathematics and Mathematical Physics* **7**(4), 86–112.

Spivakovsky, C. M., Logan, J. A., Montzka, S. A., Balkanski, Y. J., Foreman-Fowler, M., Jones, D. B. A., Horowitz, L. W., Fusco, A. C., Brenninkmeijer, C. A. M., Prather, M. J., Wofsy, S. C. & McElroy, M. B. (2000), 'Three-dimensional climatological distribution of tropospheric OH: Update and evaluation', *Journal of Geophysical Research: Atmospheres* **105**(D7), 8931–8980.

Staffelbach, T., Neftel, A., Stauffer, B. & Jacob, D. (1991), 'A record of the atmospheric methane sink from formaldehyde in polar ice cores', *Nature* **349**(6310), 603–605.
URL: *https://doi.org/10.1038/349603a0*

Stanley, E. H., Casson, N. J., Christel, S. T., Crawford, J. T., Loken, L. C. & Oliver, S. K. (2016), 'The ecology of methane in streams and rivers: Patterns, controls, and global significance', *Ecological Monographs* **86**(2), 146–171.

Stevenson, D., Zhao, A., Naik, V., O'Connor, F., Tilmes, S., Zeng, G., Murray, L., Collins, W., Griffiths, P., Shim, S., Horowitz, L., Sentman, L. & Emmons, L. (2020), 'Trends in global tropospheric hydroxyl radical and methane lifetime since 1850 from AerChemMIP', *Atmospheric Chemistry and Physics Discussions (in review)* .

Tanaka, N., Xiao, Y., Hatakeyama, S. & Ueda, S. (1997), Determination of carbon KIE of CH4 + CI reaction: Large reaction chamber experiment and its implications to atmospheric methane chemistry, *in* 'EOS Trans. Amer. Geophys. Union, 78, Sprint Meeting Suppl., S75'.

Tang, A. C., Stoy, P. C., Hirata, R., Musin, K. K., Aeries, E. B., Wenceslaus, J. & Melling, L. (2018), 'Eddy Covariance Measurements of Methane Flux at a Tropical Peat Forest in Sarawak, Malaysian Borneo', *Geophysical Research Letters* **45**(9), 4390–4399.

Tans, P. P. (1997), 'A note on isotopic ratios and the global atmospheric methane budget', *Global Biogeochemical Cycles* **11**(1), 77–81.

Tarantola, A. (2005), *Inverse Problem Theory and Methods for Model Parameter Estiamtion*, Society for Industrial and Applied Mathematics, Philadelphia, USA.

Thanwerdas, J., Saunois, M., Berchet, A., Pison, I., Hauglustaine, D., Ramonet, M., Crevoisier, C., Baier, B., Sweeney, C. & Bousquet, P. (2019), 'Impact of atomic chlorine on the modelling of total methane and its 13C : 12C isotopic ratio at global scale', *Atmospheric Chemistry and Physics Discussions (in review)* .

Thompson, L. G., Davis, M. E., Mosley-Thompson, E., Sowers, T. A., Henderson, K. A., Zagorodnov, V. S., Lin, P. N., Mikhalenko, V. N., Campen, R. K., Bolzan, J. F., Cole-Dai, J. & Francou, B. (1998), 'A 25,000-year tropical climate history from Bolivian ice cores', *Science* **282**(5395), 1858–1864.

Thornton, B. F., Wik, M. & Crill, P. M. (2016), 'Double-counting challenges the accuracy of high-latitude methane inventories', *Geophysical Research Letters* **43**(24), 12569–12577.

Thornton, J. A., Kercher, J. P., Riedel, T. P., Wagner, N. L., Cozic, J., Holloway, J. S., Dubé, W. P., Wolfe, G. M., Quinn, P. K., Middlebrook, A. M., Alexander, B. & Brown, S. S. (2010), 'A large atomic chlorine source inferred from mid-continental reactive nitrogen chemistry', *Nature* **464**(7286), 271–274.

Turner, A. J., Frankenberg, C., Wennberg, P. O. & Jacob, D. J. (2017), 'Ambiguity in the causes for decadal trends in atmospheric methane and hydroxyl', *Proceedings of the National Academy of Sciences* **114**(21), 5367–5372.

Tyler, S. C., Ajie, H. O., Rice, A. L. & Cicerone, R. J. (2000), 'Experimentally determined kinetic isotope effects in the reaction of CH4 with Cl: Implications for atmospheric CH4', *Geophysical Research Letters* **27**(12), 1715–1718.

Tyler, S. C., Crill, P. M. & Brailsford, G. W. (1994), '13C/12C Fractionation of methane during oxidation in a temperate forested soil', *Geochimica et Cosmochimica Acta* **58**(6), 1625–1633.

Valentine, D. W., Holland, E. A. & Schimel, D. S. (1994), 'Ecosystem and physiological controls over methane production in northern wetlands', *Journal of Geophysical Research* **99**(D1), 1563–1571.

van der Werf, G. R., Peters, W., van Leeuwen, T. T. & Giglio, L. (2013), 'What could have caused pre-industrial biomass burning emissions to exceed current rates?', *Climate of the Past* **9**(1), 289–306.

van der Werf, G. R., Randerson, J. T., Giglio, L., Collatz, G. J., Mu, M., Kasibhatla, P. S., Morton, D. C., Defries, R. S., Jin, Y. & Van Leeuwen, T. T. (2010), 'Global fire emissions and the contribution of deforestation, savanna, forest, agricultural, and peat fires (1997-2009)', *Atmospheric Chemistry and Physics* **10**(23), 11707–11735.

van Groenigen, K. J., van Kessel, C. & Hungate, B. A. (2013), 'Increased greenhouse-gas intensity of rice production under future atmospheric conditions', *Nature Climate Change* **3**(3), 288–291.

van Huissteden, J., Berrittella, C., Parmentier, F. J., Mi, Y., Maximov, T. C. & Dolman, A. J. (2011), 'Methane emissions from permafrost thaw lakes limited by lake drainage', *Nature Climate Change* **1**(2), 119–123.

van Vuuren, D. P., Edmonds, J., Kainuma, M., Riahi, K., Thomson, A., Hibbard, K., Hurtt, G. C., Kram, T., Krey, V., Lamarque, J. F., Masui, T., Meinshausen, M., Nakicenovic, N., Smith, S. J. & Rose, S. K. (2011), 'The representative concentration pathways: An overview', *Climatic Change* **109**(1), 5–31.

Velders, G. J. M. (1995), Description of the RIVM 2-dimensional stratosphere model, Technical report, Rijksinstituut voor Volksgezondheid en Milieu (RIVM), Bilthoven, Netherlands.

Vernon, I., Goldstein, M. & Bower, R. G. (2010), 'Galaxy Formation: a Bayesian Uncertainty Analysis', *Bayesian Analysis* **5**(4), 619–669.

Verpoorter, C., Kutser, T., Seekell, D. A. & Tranvik, L. J. (2014), 'A global inventory of lakes based on high-resolution satellite imagery', *Geophysical Research Letters* **41**(18), 6396–6402.

Vogel, B., Vogel, H., Kleffmann, J. & Kurtenbach, R. (2003), 'Measured and simulated vertical profiles of nitrous acid - Part II. Model simulations and indications for a photolytic source', *Atmospheric Environment* **37**(21), 2957–2966.

Voulgarakis, A., Naik, V., Lamarque, J. F., Shindell, D. T., Young, P. J., Prather, M. J., Wild, O., Field, R. D., Bergmann, D., Cameron-Smith, P., Cionni, I., Collins, W. J., Dalsøren, S. B., Doherty, R. M., Eyring, V., Faluvegi, G., Folberth, G. A., Horowitz, L. W., Josse, B., MacKenzie, I. A., Nagashima, T., Plummer,

D. A., Righi, M., Rumbold, S. T., Stevenson, D. S., Strode, S. A., Sudo, K., Szopa, S. & Zeng, G. (2013), 'Analysis of present day and future OH and methane lifetime in the ACCMIP simulations', *Atmospheric Chemistry and Physics* **13**(5), 2563–2587.

Wallace, R. J., Sasson, G., Garnsworthy, P. C., Tapio, I., Gregson, E., Bani, P., Huhtanen, P., Bayat, A. R., Strozzi, F., Biscarini, F., Snelling, T. J., Saunders, N., Potterton, S. L., Craigon, J., Minuti, A., Trevisi, E., Callegari, M. L., Cappelli, F. P., Cabezas-Garcia, E. H., Vilkki, J., Pinares-Patino, C., Fliegerová, K. O., Mrázek, J., Sechovcová, H., Kopečný, J., Bonin, A., Boyer, F., Taberlet, P., Kokou, F., Halperin, E., Williams, J. L., Shingfield, K. J. & Mizrahi, I. (2019), 'A heritable subset of the core rumen microbiome dictates dairy cow productivity and emissions', *Science Advances* **5**(7), eaav8391.

Wania, R., Melton, J. R., Hodson, E. L., Poulter, B., Ringeval, B., Spahni, R., Bohn, T., Avis, C. A., Chen, G., Eliseev, A. V., Hopcroft, P. O., Riley, W. J., Subin, Z. M., Tian, H., Van Bodegom, P. M., Kleinen, T., Yu, Z. C., Singarayer, J. S., Zürcher, S., Lettenmaier, D. P., Beerling, D. J., Denisov, S. N., Prigent, C., Papa, F. & Kaplan, J. O. (2013), 'Present state of global wetland extent and wetland methane modelling: Methodology of a model inter-comparison project (WETCHIMP)', *Geoscientific Model Development* **6**(3), 617–641.

Wania, R., Ross, I. & Prentice, I. C. (2010), 'Implementation and evaluation of a new methane model within a dynamic global vegetation model: LPJ-WHyMe v1.3.1', *Geoscientific Model Development* **3**(2), 565–584.

Watts, J. D., Kimball, J. S., Bartsch, A. & McDonald, K. C. (2014), 'Surface water inundation in the boreal-Arctic: potential impacts on regional methane emissions', *Environmental Research Letters* **9**(7), 075001.

Weinstock, B. (1969), 'Carbon Monoxide: Residence Time in the Atmosphere', *Science* **166**(3902), 224–225.

Wennberg, P. O. (2004), 'Recent changes in the air-sea gas exchange of methyl chloroform', *Geophysical Research Letters* **31**(16), L16112.

Westerling, A. L., Hidalgo, H. G., Cayan, D. R. & Swetnam, T. W. (2006), 'Warming and earlier spring increase Western U.S. forest wildfire activity', *Science* **313**(5789), 940–943.

White, J., Vaughn, B. & Michel, S. (2018), 'Stable Isotopic Composition of Atmospheric Methane (13C) from the NOAA ESRL Carbon Cycle Cooperative Global Air Sampling Network, 1998-2016, Version: 2018-01-31'.
URL: *ftp://aftp.cmdl.noaa.gov/data/trace_gases/ch4c13/flask/*

Whiticar, M. & Schaefer, H. (2007), 'Constraining past global tropospheric methane budgets with carbon and hydrogen isotope ratios in ice', *Philosophical Transactions of the Royal Society A: Mathematical, Physical and Engineering Sciences* **365**(1856), 1793–1828.

Wik, M., Thornton, B. F., Bastviken, D., MacIntyre, S., Varner, R. K. & Crill, P. M. (2014), 'Energy input is primary controller of methane bubbling in subarctic lakes', *Geophysical Research Letters* **41**(2), 555–560.

Wik, M., Thornton, B. F., Bastviken, D., Uhlbäck, J. & Crill, P. M. (2016), 'Biased sampling of methane release from northern lakes: A problem for extrapolation', *Geophysical Research Letters* **43**(3), 1256–1262.

Wik, M., Varner, R. K., Anthony, K. W., MacIntyre, S. & Bastviken, D. (2016), 'Climate-sensitive northern lakes and ponds are critical components of methane release', *Nature Geoscience* **9**(2), 99–105.

Wilkinson, J., Maeck, A., Alshboul, Z. & Lorke, A. (2015), 'Continuous Seasonal River Ebullition Measurements Linked to Sediment Methane Formation', *Environmental Science & Technology* **49**(22), 13121–13129.

Worden, J. R., Bloom, A. A., Pandey, S., Jiang, Z., Worden, H. M., Walker, T. W., Houweling, S. & Röckmann, T. (2017), 'Reduced biomass burning emissions reconcile conflicting estimates of the post-2006 atmospheric methane budget', *Nature Communications* **8**(1), 2227.

Wu, S., Mickley, L. J., Jacob, D. J., Rind, D. & Streets, D. G. (2008), 'Effects of 2000–2050 changes in climate and emissions on global tropospheric ozone and the policy-relevant background surface ozone in the United States', *Journal of Geophysical Research* **113**(D18), D18312.

Xiao, Y., Logan, J. A., Jacob, D. J., Hudman, R. C., Yantosca, R. & Blake, D. R. (2008), 'Global budget of ethane and regional constraints on U.S. sources', *Journal of Geophysical Research: Atmospheres* **113**(21), D21306.

Yacovitch, T. I., Daube, C., Vaughn, T. L., Bell, C. S., Roscioli, J. R., Knighton, W. B., Nelson, D. D., Zimmerle, D., Pétron, G. & Herndon, S. C. (2017), 'Natural gas facility methane emissions: measurements by tracer flux ratio in two US natural gas producing basins', *Elem Sci Anth* **5**(2013), 69.

Yan, X., Akiyama, H., Yagi, K. & Akimoto, H. (2009), 'Global estimations of the inventory and mitigation potential of methane emissions from rice cultivation conducted using the 2006 Intergovernmental Panel on Climate Change Guidelines', *Global Biogeochemical Cycles* **23**(2), GB2002.

Yan, Y., Bender, M. L., Brook, E. J., Clifford, H. M., Kemeny, P. C., Kurbatov, A. V., Mackay, S., Mayewski, P. A., Ng, J., Severinghaus, J. P. & Higgins, J. A. (2019), 'Two-million-year-old snapshots of atmospheric gases from Antarctic ice', *Nature* **574**(7780), 663–666.

Yang, L. (2019), 'Contrasting methane emissions from upstream and downstream rivers and their associated subtropical reservoir in eastern China', *Scientific Reports* **9**(1), 8072.

Yuan, Y., Conrad, R. & Lu, Y. (2011), 'Transcriptional response of methanogen mcrA genes to oxygen exposure of rice field soil', *Environmental Microbiology Reports* **3**(3), 320–328.

Yvon-Durocher, G., Allen, A. P., Bastviken, D., Conrad, R., Gudasz, C., St-Pierre, A., Thanh-Duc, N. & Del Giorgio, P. A. (2014), 'Methane fluxes show consistent temperature dependence across microbial to ecosystem scales', *Nature* **507**(7493), 488–491.

Yvon-Durocher, G., Hulatt, C. J., Woodward, G. & Trimmer, M. (2017), 'Long-term warming amplifies shifts in the carbon cycle of experimental ponds', *Nature Climate Change* **7**(3), 209–213.